UNIVERSITY OF CALIFORNIA SAN DIEGO

Model-enabled Design of Nano-structured Thin Film Sensors

A dissertation submitted in partial satisfaction of the requirements for the degree Doctor of Philosophy

in

Structural Engineering

by

Bo Mi Lee

Committee in charge:

Professor Kenneth J. Loh, Chair
Professor Jiun-Shyan Chen
Professor Francesco Lanza di Scalea
Professor Darren Lipomi
Professor Michael Todd

2019

The Dissertation of Bo Mi Lee is approved, and it is acceptable in quality and form for publication on microfilm and electronically:

_____

_____

_____

_____

_____

Chair

University of California San Diego

2019

DEDICATION

To Mom, Dad, Ki Hyun, and my husband, Minseung

TABLE OF CONTENTS

LIST OF ABBREVIATIONS AND ACRONYMS

1D	One-Dimensional
2D	Two-Dimensional
3D	Three-Dimensional
AJGV	Average Junction Gap Variation
AFM	Atomic Force Microscopy
CFRP	Carbon Fiber-Reinforced Polymer
CN	Carbon Nanofiber
CNT	Carbon Nanotube
DI	Deionized
EIS	Electrical Impedance Spectroscopy
EM	Electromagnetic
EPT	Electrical Percolation Threshold
ETDR	Electrical Time-Domain Reflectometry
FBG	Fiber Bragg grating
GFRP	Glass Fiber-Reinforced Polymer
NP	Nanoparticle
NW	Nanowire
MWCNT	Multi-Walled Carbon Nanotube
OTDR	Optical Time Domain Reflectometry
PBC	Periodic Boundary Condition
p-SWCNT	Purified Single-Walled Carbon Nanotube
RVE	Representative Volume Element

SEM	Scanning Electron Microscopy
S	Strain Sensitivity
SHM	Structural Health Monitoring
STEM	Scanning Transmission Electron Microscopy
SWCNT	Single-Walled Carbon Nanotube
TEM	Tunneling Electron Microscopy
u-SWCNT	Unpurified Single-Walled Carbon Nanotube
QD	Quantum Dot

GLOSSARY

CdSe	Cadmium Selenide
CMC	Carboxymethyl Cellulose
Au	Gold
Ag	Silver
$CaCO_3$	Calcium Carbonate
CdTe	Cadmium Telluride
Cr_2O_3	Chromium Oxides
GaAs	Gallium Arsenide
GO	Graphene Oxide
Hg^{2+}	Mercury Ions
H_2	Hydrogen
NO_2	Nitrogen Dioxide
MoS_2	Molybdenum Disulfide
OTA	Ochratoxin A
PANI	Polyaniline
PBCA	Poly(butyl) Cyanoacrylate
PDMS	Polydimethylsiloxane
PEO	Polyethylene Oxide
PMMA	Poly(methyl methacrylate)
PS	Polystyrene
PSS	Poly(sodium 4-styrenesulfonate)
PU	Polyurethane

PUA	Polyurethane Acrylate
PVA	Polyvinyl Alchol
PVC	Poly(vinyl chloride)
PVDF	Polyvinylidene Fluoride
In_2O_3	Indium Oxide
Si	Silicon
SnO_2	Tin Oxide
TiO_2	Titanium Dioxide
ZnO	Zinc-Oxide
Zr_2O_3	Zirconium Oxide

LIST OF FIGURES

LIST OF TABLES

ACKNOWLEDGMENTS

First, I would like to express my sincere appreciation to my advisor, Professor Kenneth Loh, for his endless support during my PhD study. The successful completion of my thesis was possible only because of his mentoring. His patient guidance, continuous encouragement, and academic inputs have always motivated me and helped me to grow as an independent researcher. In addition, I would like to thank my other dissertation committee members, Professors Francesco Lanza di Scalea, Jiun-Shyan Chen, Michael Todd, and Darren Lipomi, for their insightful and intellectual guidance and encouragement for my dissertation. Their comments helped me to look at my research from diverse perspectives.

My sincere thanks also go to Professor Yuan-Sen Yang at National Taipei University of Technology. His expertise in image analysis helped me to broaden my research using various image processing and analysis techniques.

I would like to thank my colleagues and friends, Sumit Gupta, Han Joo Lee, Morgan Funderburk, Yujin Park, Yening Shu, Tianjiao Zhang, Zachary Huang, Yun-An Lin, Gianmarco Vella, and Tae Hoon Kang in the Active, Responsive, Multifunctional, and Ordered-materials Research (ARMOR) laboratory.

I sincerely appreciate the National Science Foundation (NSF) for supporting my doctoral research (Grant Number: CMMI-1253564). Additional support has been provided by the Jacobs School of Engineering, University of California—San Diego.

Last but not least, I would like to thank my family for their warm love, support, and encouragement. Words cannot describe how thankful I am. I am so grateful for the harmonious and loving family that my parents have given me. My sister's brightness has been my source of energy, and my grandma's love has granted me peace of mind. The last thank that I saved in this

acknowledgment goes to my beloved husband, Minseung Kim. I was able to successfully endure the challenges of completing PhD because of Minseung's love and support

Chapter 1, in part, is a reprint of the material as it appears in Strain Sensing and Structural Health Monitoring using Nanofilm and Nanocomposites, Elsevier, Bo Mi Lee; Sumit Gupta; Kennth J. Loh; Satish Nagarajaiah, 2016. The dissertation author was the primary author of this book chapter.

Chapter 2, in full, is a reprint of the material as it appears in *Journal of Material Science*, Bo Mi Lee; Kenneth J. Loh, 2015. The dissertation author was the primary researcher and author of this paper.

Chapter 3, in full, is a reprint of the material as it appears in Computational Mechanics, Bo Mi Lee; Kenneth J. Loh; Yuan-Sen Yang, 2017. The dissertation author was the primary researcher and author of this paper.

Chapter 4, in full, is a reprint of the material as it appears in Nanotechnology, Bo Mi Lee; Kenneth J. Loh, 2017. The dissertation author was the primary researcher and author of this paper.

Chapter 5, in part, is a reprint of the material as it appears in may appear in IEEE Sensors, Bo Mi Lee; Kenneth J. Loh; Francesco Lanza di Scalea, 2018. The dissertation author was the primary researcher and author of this paper.

Chapter 5, in part, is a currently being prepared for submission for publication of the material. Bo Mi Lee; Zachary Huang; Kenneth J. Loh. The dissertation author was the primary researcher and author of this material.

VITA

2009 Bachelor of Science, Hanyang University, South Korea

2011 Master of Science, Korea Advanced Institute of Science and Technology (KAIST), South Korea

2011-2012 Researcher, Korea Institute of Construction Technology, South Korea

2019 Doctor of Philosophy, University of California San Diego, USA

PUBLICATIONS

1. **B. M. Lee**, K. J. Loh, and F. Lanza di Scalea, "Distributed Strain Sensing Using Electrical Time Domain Reflectometry with Nanocomposites," *IEEE Sensors,* Accepted.
2. **B. M. Lee** and K. J. Loh, 2017, "Carbon Nanotube Thin Film Strain Sensors: Comparison between Experimental Tests and Numerical Simulations," *Nanotechnology*, IOP, 28(15), 1-15, DOI: 10.1088/1361-6528/aa6382 (This work is featured by IOP Publishing: Highlights of 2017).
3. **B. M. Lee**, K. J. Loh, and Y. S. Yang, 2017, "Carbon Nanotube Thin Film Strain Sensor Models Assembled using Nano- and Micro-Scale Imaging," *Computational Mechanics*, Springer, 60(1), 39-49, DOI: 10.1007/s00466-017-1391-6.
4. **B. M. Lee** and K. J. Loh, 2015, "A 2D Percolation-based Model for Characterizing the Piezoresistivity of Carbon Nanotube-based Films," *Journal of Material Science*, Springer, 50(7), 2973-2983, DOI: 10.1007/s10853-015-8862-y.
5. I. H. Kim, H. J. Jung, **B. M. Lee**, and S. J. Jang, 2011, "Broadband Energy-harvesting using A Two Degree-of-freedom Vibration Body," *Applied Physics Letters*, AIP, 98, 214102/1-3, DOI: 10.1063/1.3595278.

ABSTRACT OF THE DISSERTATION

Model-enabled Design of Nano-structured Thin Film Sensors

by

Bo Mi Lee

Doctor of Philosophy in Structural Engineering

University of California San Diego, 2019

Professor Kenneth J. Loh, Chair

Nanomaterials are nanostructured materials in which one of its dimensions is at least smaller than 100 nm. The unique size, shape, structure, and high surface area-to-volume ratio of nanomaterials result in outstanding optical, electrical, mechanical, and magnetic properties versus their bulk counterparts. In particular, carbon nanotubes (CNTs) possess outstanding electrical, mechanical, and electromechanical properties due to their unique structure and carbon-carbon covalent bonds. To take advantage of these properties for use in real-world applications, one approach is to disperse CNTs in a polymer matrix to form nanocomposites. However, the underlying mechanisms of how CNT-based nanocomposites derive their electromechanical properties remains poorly understood, despite the vast amount of experimental and numerical modeling work done in this area.

In this thesis, a CNT-based thin film model was derived based on percolation theory. One dimensional CNT elements were randomly distributed in a predefined two-dimensional area, and their electrical and electromechanical properties were simulated. The objective was to evaluate the main parameters that influence the model's electrical and electromechanical properties. Numerical simulation results showed that the percolation threshold and electrical characteristics of the thin film are affected by CNT lengths, concentrations, and intrinsic piezoresistivity. It was also found that the electromechanical behavior of the model was characterized by linear piezoresistivity. The CNT-based thin film model became less sensitive to applied strains as CNT concentration increased. Furthermore, an important finding was that, near the percolation threshold, inconsistent strain sensing response was observed.

In order to improve the accuracy of predicting the bulk-scale electromechanical behavior of CNT-based thin film, the model was updated with multi-scale experimental measurements. Atomic force microscope images of CNT-based thin films were acquired, and image analysis was conducted to measure the physical characteristics of as-dispersed CNTs, which were then

incorporated in the model. A key finding was that the morphology of the CNT network is an important parameter that governs bulk nanocomposite electrical and electromechanical behavior. The models were validated by conducting electromechanical experiments that characterized thin film behavior fabricated using different parameters and subjected to different loading excitations. The model was able to accurately characterize the electromechanical properties of these films.

This dissertation also explores the use of numerical models to guide the design of electrical time-domain reflectometry (ETDR) sensors that featured CNT-based thin film sensing elements. An advantage offered by the proposed sensor is that, unlike currently available distributed strain sensing systems, implementation of ETDR sensors is easier due to their simple system architecture and low manufacturing and installation costs. The previous simulation results showed that the CNT-based thin film was more sensitive to strains as CNTs were more aligned. Therefore, CNT sensing elements with aligned CNTs were integrated in the ETDR setup, and the sensor showed better strain sensing performance. The two most important research contributions of this dissertation were: (1) the systematic investigation conducted to uncover the fundamental material mechanisms that governed CNT-based thin film electromechanical behavior; and (2) the development of a numerical model for sensor design and optimization.

Chapter 1.

Introduction

1.1 Promise of Nanotechnology

Nanotechnology and nanomaterials have brought forth technological breakthroughs in both science and engineering since the invention of the scanning tunneling microscope in 1981 and the discovery of the fullerene in 1985 [1]. Nanotechnology is defined as a technology of engineering and utilizing materials with at least one inner or outer dimension is in the nanometer range. Nanomaterials can be categorized as zero-dimensional (*e.g.*, nanoparticles (NPs)), one-dimensional (1D) (*e.g.*, nanotube, nanowires, and nanorods), two-dimensional (2D) (*e.g.*, graphene), and three-dimensional (3D) (*e.g.*, box-shaped graphene) depending on the number of dimensions that are less than 100 nm [2]. They can also be categorized into carbon-based nanomaterials (*i.e.*, carbon nanotubes (CNTs), carbon nanofibers, and graphene), inorganic nanomaterials (*i.e.*, metal oxide and zinc-oxide (ZnO) NPs), organic nanomaterials (*i.e.*, silk fibroin, poly(lactic-co-glycolic) acid, and chitosan NPs), and composite nanomaterials depending on their compositions [3].

Due to their unique structures, nanomaterials have unusual electrical, mechanical, optical, and magnetic properties drastically different than their corresponding bulk form [4]. For example, graphene is a one-atom-thick 2D carbon-based nanomaterial in which carbon atoms are densely packed into a 2D honeycomb crystal lattice. It is a basic structural element of carbon-based materials of carbon nanotubes, fullerenes, and graphite. Graphene is a zero-bandgap semiconductor and possesses a *sp2* bond structure in which each carbon atom has σ-bond with three neighboring atoms and one out-of-plane π-bond. Due to the graphene's electronic structure, it has extremely high electron and hole mobility (>10^5 $cm^2/V{\cdot}s$) [5] and high thermal conductivity (3×10^3–5×10^3 $W/m\cdot k$) at room temperature [6]. The carbon-carbon covalent bond enables graphene to be 300 times stronger than steel. The optical transmittance of graphene over the visible spectrum was shown to be ~98%, meaning that graphene can be used to assemble transparent conductors [7].

CNTs physically represent a layer of graphene rolled into a cylindrical shape. Similar to graphene, CNTs possess extraordinary mechanical properties due to the covalent bond between carbon atoms. The specific strength of CNTs was found to be 48×10^3 $kN{\cdot}m/kg$ and is significantly higher than that of steel (154 $kN\cdot m/kg$) [8]. CNTs can be either electrically metallic or semiconducting depending on their chirality. Due to the 1D structure, metallic single-walled carbon nanotubes (SWCNTs) and multi-walled carbon nanotubes (MWCNTs) show ballistic electronic transport with negligible scattering, which contributes to their high electrical conductivity [4]. In addition, the theoretical electrical current density of metallic SWCNTs is 4×10^9 A/cm^2, which is three orders of magnitude higher than that of copper [9]. Electron and hole mobility of a semiconducting SWCNT can be up to 1×10^5 $cm^2/V\cdot s$, which is better than conventional silicon transistors (1×10^4 $cm^2/V\cdot s$), thereby suggesting that semiconducting

SWCNTs can be beneficial for future transistors [10]. An individual MWCNT showed better thermal conductivity (> 3 kW/m·K) than diamond (2 kW/m·K).

In addition, due to their nanoscale dimensions, nanomaterials show size-dependent properties. Quantum dots (QDs) of nanocrystals emit different colors of light according to their size. For example, the optical emission of cadmium selenide (CdSe) QDs shifted from blue ($\lambda = 500$ nm) to red ($\lambda = 610$ nm) as their size increased from 2 to 10 nm [11]. This occurred because the band gap became bigger as the size of QDs got smaller, resulting in a shift in the optical emission. In addition, the optical properties of metallic NPs (*e.g.*, gold (Au) and silver (Ag) NPs) are dominated by surface-plasmon resonance of the collective oscillation of surface electrons. Specifically, Au nanospheres with the size of 2-50 nm showed a peak absorption at ~520 nm, while larger Au nanospheres had broader peaks at longer wavelengths (where 100 nm Au nanospheres displayed a peak absorption at 572 nm) [12]. Zhang *et al.* [13] studied the size-dependent *in vivo* toxicity of polyethylene glycol-coated Au NPs in mice. It was shown that 5 and 10 nm Au NPs dominantly accumulated in the liver, 30 nm Au NPs accumulated in the spleen, and 60 nm particles accumulated minimally in organs. In addition, mice treated with 10 and 60 nm Au NPs had increased alanine transaminase and aspartate transaminase, indicating that these Au NPs adversely affected the liver and kidney [13].

Advances in microscopy technologies, such as scanning electron microscopy (SEM), atomic force microscopy (AFM), tunneling electron microscopy (TEM), and scanning transmission electron microscopy (STEM), have enabled visualization of atomic structures, nanomaterial characterization, and *in-situ* nanomaterial manipulation [14, 15]. For example, Junno *et al.* [14] used AFM to displace gallium arsenide (GaAs) NPs by first imaging GaAs NPs to identify their locations and then physically pushing the particles with an AFM cantilever to their desired positions. To realize real-time manipulation of nanomaterials, Polyakov *et al.* [15] placed

an AFM cantilever inside an SEM to displace Au and Ag NPs on an oxidized Si substrate while visualizing them through SEM.

Various nanofabrication techniques, which are used to synthesize nanomaterials and to fabricate nanostructured materials and nanodevices, have enabled the creation of diverse nanosystems. In particular, the capability of nanofabrication to control the size, structure, and shape of nanomaterials has opened opportunities to tailor their properties [16]. Nanofabrication techniques can be categorized according to their assembly, following a bottom-up or top-down approach. First, bottom-up fabrication, including dip-pen nanolithography, electrodeposition, and molecular self-assembly, is an additive approach that combines atoms and molecules to form nanomaterials. For example, dip-pen nanolithography fabricates or patterns nanostructures on a surface by directly writing on the surface using an ink-coated AFM tip. Piner *et al.* [17] used dip-pen nanolithography to write alkanethiols on a thin Au film with 30 nm resolution. Second, top-down fabrication, including photolithography, laser ablation, and nano-imprint lithography, is a subtractive approach that starts with a large-scale object and gradually removes and subdivides a bulk material to form nanomaterials. For example, nanoimprint lithography is a low-cost and high-throughput lithographic method involving two steps: i) imprinting using a mold with nanostructures pressed into a resist; and ii) removal of the mold by etching [18]. Chou *et al.* [18] employed nano-imprint lithography to fabricate a photodetector with 25 nm feature size.

Advances in nanomaterials and nanotechnology and various nanofabrication tools have offered considerable promise to resolve problems in a wide range of fields including energy, engineering, healthcare, biology, and environment, among others. First, since the size of NPs is generally comparable with biomolecules (*i.e.*, DNA, protein, and cell membrane), they can offer unprecedented solutions in biology and medicine [19]. Their high surface area has provided new possibilities in catalysis with improved reactivity [20]. Moreover, size-dependent optical

properties of nanomaterials can be applied to biology and energy. For example, the optical properties of QDs can be tuned for multiplexed optical sensing applications [21]. The efficiency of solar cells can be improved by combining NPs of different sizes to absorb the entire solar spectrum [22]. In addition, multifunctionality can be encoded in a nanoscale device [23, 24]. An example is a multifunctional mesoporous silica NP (100–200 nm) for drug delivery, magnetic resonance and manipulation, fluorescence imaging, and cell targeting [24]. Application examples of nanomaterial and nanotechnology with more details will be reviewed in Section 1.2.

1.2 Applications of Nanotechnology

Through the National Nanotechnology Initiative, the United States has invested $1.2 billion in 2018 and over $25 billion since its inception in 2001 to explore the unlimited applications of nanotechnology [25]. The focus of nanotechnology research and development has evolved from fundamental scientific discoveries in 2000–2010 to nanosystem research for applications in 2010–2020 [26]. Nanotechnologies can be applied in fields as diverse as medicine [27, 28], food science [29, 30], textiles [31, 32], energies [33, 34], and various engineering areas including electrical [35-37], computer [38, 39], and structural engineering [40, 41].

Nanotechnology has been employed to solve open problems in electrical and computer engineering. For example, nanomaterials such as CNTs [42, 43], graphene [44, 45], and QDs [46] have been emphasized as crucial materials which can realize flexible and stretchable electronics due to their high intrinsic electron mobility, conductivity, mechanical strength, and flexibility. Eda *et al.* [45] produced a transparent and flexible graphene-based transistor with the thickness of one to five layers of graphene (1–2 nm). Sun *et al.* [43] assembled transparent thin film transistors by dispersing low concentrations of SWCNTs, which showed high electrical performance with a field-effect mobility of 35 cm^2/V and on/off ratio (I_{on}/I_{off}) of 6×10^6. Such high performance was

attained as a result of CNT's long lengths (~10 μm) and Y-type junctions, which lowered contact resistance. Similarly, Choi *et al.* [46] demonstrated that CdSe QD-based thin film transistors achieved a field-effect mobility of 27 cm^2/V and I_{on}/I_{off} ratio of 10^6. Radisavljevic *et al.* [47] assembled a field-effect transistor using a single layer of Molybdenum disulfide (MoS_2), which showed a mobility of 217 $cm^2/V{\cdot}s$ and I_{on}/I_{off} ratio of 10^8. Besides the intrinsic properties of nanomaterials, their small, nanoscale dimensions can reduce the size of electrical or optical components (*i.e.*, transistors, switches, and supercapacitors), thus supporting the production of extremely small devices [36, 37, 48]. In 2017, Intel released a 10-nm transistor in which 100 million transistors could fit in 1 mm^2; in contrast, the diameter of the first point contact transistor in 1947 was 1 cm. 1D structures of nanowires and CNTs can be used as both a device and electric wire, functioning as building blocks for nanoscale electronics [37]. Geiselmann *et al.* [48] engineered a nanodiamond-based optical transistor that served as a photonic counterpart of an electronic transistor for optical signal processing.

Nanoengineered textiles offer multiple functionalities of sensing [49], energy harvesting [31], resisting wrinkles [50], antibacterial control [51], and enhancing strength [31, 52]. Incorporating clay NPs in textile can endow it with electrical, heat, and chemical resistance, as well as ultraviolet (UV) light-blocking and flame-retardant properties [53]. Seung *et al.* [31] demonstrated a mechanically robust electric-power-generating textile using ZnO nanorods, nanopatterned polydimethylsiloxane (PDMS), and silver-coated textile, which generated a maximum power of 1.1 mW using the triboelectric effect. Lee *et al.* [49] fabricated conductive textiles by integrating Ag NPs in poly(styrene-block-butadiene-styrene) polymer, which covered poly(p-phenylene terephthalamide) fibers, and used them to assemble a capacitive textile-based pressure sensor. The electrical resistance of the conductive textile was 0.15 Ω/cm. Pressure sensing results showed two different pressure sensitivity regions of higher sensitivity (0.24 kPa^{-1}) at lower

pressure (P < 2 kPa) and lower sensitivity (0.062 kPa^{-1}) at high pressure (2 kPa < P < 10 kPa). Zhao *et al.* [51] attached single-layer graphene oxide (GO) to cotton fabrics for antibacterial control purposes and demonstrated the capability of the GO-modified cotton fabric to inactivate most of the bacteria (> 98%) in 4 hours.

Nanotechnology has influenced the medical field including biological devices [54], biosensors [55], and biomedicine [27, 56, 57]. As mentioned in Section 1.1, nanomaterials' nanoscale sizes enable them to access cells, tissues, and organs that other particles cannot reach. In addition, limitations of current chemotherapy treatment, such as nontarget tissue toxicity and drug resistance, have been addressed by nanomaterial-based drug-delivery systems by offering site-specific drug release [58]. Various nanomaterials including dendrimers [59], chitosan NPs [60], liposomes [61], nanospheres [62], and Au NPs [56] have been used for drug delivery [58]. For example, CytImmune Sciences Inc. used Au NPs attached to a tumor-eliminating agent to deliver chemotherapy drugs directly to cancer cells [56]. Recently, Wang *et al.* [57] developed a vaccine using protein NPs to combat influenza A viruses. Duan *et al.* [60] coated curcumin-loaded chitosan on cationic poly(butyl) cyanoacrylate (PBCAs) NPs to take advantage of the antitumor activity of curcumin-PBCA NPs against hepatocellular carcinoma cells. They treated two groups of mice with curcumin-loaded and empty PBCA NPs for four weeks. The mice treated with curcumin-PBCA NPs showed decreased tumor volume compared with those treated with empty PBCA NPs.

On the other hand, sustainable energy systems have been significantly improved by nanotechnology [33, 63, 64]. The efficiency of photovoltaic cells can be enhanced with the incorporation of nanoscale components (*i.e.*, electrodes), which enhances the optical path and decreases charge recombination [33]. For example, Tang *et al.* [63] assembled a photovoltaic device using CdS-Cu_2S core-shell nanowires. The device's open circuit voltage (V_{oc} = 0.61 V) and

fill factors (FF = 80%), which determine the overall behavior of a solar cell, were higher compared to CdS-Cu_2S thin film solar cells with $V_{oc} \cong 540$ mV and FF = 71%. Zhang *et al.* [64] assembled rechargeable batteries using cathodes of self-assembled 3D nanostructured NiOOH-nickel composites. The battery showed extremely fast battery charge and discharge rates (90% charging in 2 min) without sacrificing energy storage capacity.

Researchers in structural engineering have employed nanomaterials to enhance the mechanical strength of concrete and cement by adding NPs such as zirconium oxide (Zr_2O_3) [65], calcium carbonate ($CaCO_3$) [66], chromium oxides (Cr_2O_3) [67], and Ag NPs [68]. Nazari *et al.* [67] dispersed Cr_2O_3 NPs in a cementitious composite and studied their effects on the composite's compressive and flexural strength. The study demonstrated enhanced compressive and flexural strengths of Cr_2O_3-based cementitious composite (47.7 and 4.9 MPa, respectively) compared to those of a control case without Cr_2O_3 NPs inclusion (39.8 and 4.2 MPa, respectively). Besides, nanomaterials and nanotechnology have been used to functionalize structural materials with self-healing properties [41, 69]. Bang *et al.* [41] included microbial calcite (bio-based nanomaterials) in concrete and showed that microbial calcite increased the concrete's compressive strength and stiffness through crack remediation. Specifically, the microbial calcite-based concrete beam's stiffness and compressive strength were 550 kN/m and 36 MPa, while those of the untreated concrete beam were 500 kN/m and 29 MPa, respectively.

1.3 Nanomaterial-Based Sensors

Among various applications of nanotechnology and nanomaterials, many researchers have sought to develop new chemical (*i.e.*, gas and corrosion), physical (*i.e.*, strain, temperature, and pressure), and biological (*i.e.*, DNA, proteins, and pathogen) sensors. Nanomaterials' high surface area, high surface-to-volume ratio, and electrical, electromechanical, and optical properties can be

used to develop sensors with improved sensitivity [70], specificity [71], multiplexing capability [72], and reduced detection times [55]. For example, due to their high surface-to-volume ratios, nanomaterials' electrical properties can be sensitive to surface molecules, thereby enabling single-molecule detection [70]. Zhang *et al.* [73] fabricated an indium oxide (In_2O_3) nanowire-based chemical sensor that could detect nitrogen dioxide (NO_2) as low as 0.5 ppm. Besides, Li *et al.* [70] functionalized silicon nanowires (SiNWs) with single-stranded probe DNA molecules so that only the complementary DNA target can be detected by DNA hybridization. Because the material itself is sensitive to external stimuli, the sensing properties can be possibly controlled by different designs and various nanotechnologies. For instance, Lyson-Sypien *et al.* [74] studied titanium dioxide (TiO_2)-tin oxide (SnO_2) nanocomposites for hydrogen (H_2) detection with various TiO_2 concentrations from 2 to 80 mol% and found that 50 mol% TiO_2-SnO2 nanocomposite showed the best H_2-sensing response.

In particular, nanomaterial-based sensors have been widely exploited for chemical sensing [75-77]. The nanomaterials' electrical properties (*i.e.*, electrical conductance or capacitance) or optical properties (*i.e.*, fluorescent intensity) change when they are exposed to gas (*i.e.*, ammonia and nitrogen dioxide), such that the existence and concentration of gas can be estimated by measuring these electrical or optical parameters. Early research conducted by Lonergan *et al.* [76] utilized carbon black-based vapor sensors to detect benzene and methanol by measuring their electrical resistance signals. Zhang *et al.* [77] fabricated a conductive carbon nanofiber (CN)-polystyrene (PS) composite for tetrahydrofuran vapor sensing. The results showed that the electrical resistance of the CN-PS composites increased 10^4 to 10^5 times when they were exposed to saturated tetrahydrofuran vapor. Xie *et al.* [72] used SiNW-based fluorescent sensors to detect mercury ions (Hg^{2+}). The surface of SiNWs was functionalized by glutaraldehyde, and then SiNWs were assembled with thymine-rich DNA stands. With the existence of Hg^{2+} ions, the distance

between DNAs decreased due to thymine-Hg-thymine pair formation, lowering fluorescence intensity. The sensors were able to detect Hg^{2+} as low as 5 pM, and their high sensitivity was due to the high surface area and surface-to-volume ratio of SiNWs.

Nanomaterials' similar size to biomolecules and cells and their unique properties, such as fast electron transport [4], quantum mechanical properties [78], and signal amplification [79], have inspired many researchers in biology to employ them to develop novel miniaturized biosensors [80] that are biocompatible [81], highly accurate [82], and high sensitivity [71]. Lu *et al.* [83] developed a fluorescence sensor based on molybdenum disulfide (MoS_2) nanosheets and cadmium telluride (CdTe) QDs to detect toxic Ochratoxin A (OTA), which exists in plant-origin foods such as fruits, corn, coffee, and cereals. As the concentration of OTA increased from 1 to 1,000 ng/mL, the fluorescence intensity increased from 160 to 200 a.u. In addition, biomolecules functionalized by nanomaterials have brought significant advances in nanomedicine through target binding, imaging, and drug delivery. For example, the intrinsic optical properties of Au NPs are widely used to detect protein-protein interaction [81]. Homogeneous suspensions of AuNPs between 10 and 50 nm showed a pink color, while a blue-gray color was displayed when AuNPs became closer together resulting from binding events between two protein partners immobilized in different AuNPs [81]. Xie *et al.* [72] functionalized SiNWs with DNA strands that could detect low concentration of DNA targets (1 pM).

Besides chemical and biological sensing, researchers have assembled nanomaterial-based nanocomposites to measure physical properties such as strain [84], pressure [85], and temperature [86]. For example, Gullapalli *et al.* [84] embedded ZnO nanostructures in a cellulose matrix to form a piezoelectric strain sensor. Two ends of a 2×0.5 cm^2 ZnO-based nanocomposite were coated with gold electrodes, and the nanocomposite was attached to a brass beam using an insulating epoxy. The output current of the ZnO-based nanocomposite was increased when

subjected to uniaxial tensile loading up to 1,600 με. Gong *et al.* [85] fabricated a flexible pressure sensor using a sandwiched structure of Au NW-impregnated tissue paper between PDMS sheets. This sensor, used to monitor the blood pressure of a human radial artery, was able to measure pressure force as low as 13 Pa with high sensitivity (1.14 kPa^{-1}), low energy consumption (30 μW), and fast response time (< 17 ms). In addition, Lin *et al.* [87] developed a self-powered triboelectric pressure sensor composed of a nanopatterned PDMS on Au electrode and Ag nanowires deposited on the aluminum film. The pressure sensor showed high sensitivity (0.31 kPa^{-1}), fast response time (< 5ms), and long-term stability (30,000 cycles). By incorporating the nanopatterned PDMS film and Ag nanowires, pressure-sensing response was improved due to the large effective contact area between the PDMS film and Ag nanowires. Vetrone *et al.* [86] devised a thermal nanoprobe based on temperature-sensitive fluorescent NPs (*i.e.*, $NaYF_4:ER^{3+},Yb^{3+}$) to measure the internal temperature of the living cells (*i.e.*, HeLa cervical cancer cells). The NPs were capable of converting long-wavelength, near-infrared light to green and red light of shorter wavelengths so that inexpensive near-infrared lasers could be used to excite the NPs. The emission intensities of the green fluorescence bands of ER^{3+} changed with temperature, thus enabling temperature measurement using the fluorescent intensities.

1.4 CNT-Based Strain Sensors

In particular, CNT-based nanocomposites or nanofilms have been recognized as next-generation strain sensing materials due to their electromechanical [88, 89] and Raman active behavior [90]. Stampfer *et al.* [88] suspended a 600 nm-long SWCNT on an Au cantilever support to investigate its potential for electromechanical displacement sensing. AFM in contact mode was used to induce strain in an SWCNT, and the results showed that the maximum strain sensitivity of the SWCNT was 2,900, which was attributed to its band-gap and structural changes. On the other

hand, spectral methods (*i.e.*, Raman spectroscopy) were used to characterize strain-sensitive behavior of individual CNTs [90]. For example, Cronin *et al.* [90] demonstrated that the *G* and *G'* bands in Raman mode of individual SWCNTs shifted linearly when they are subjected to three-point bending. These experimental results confirmed the advantages of CNTs for developing high-performance strain sensing devices.

1.4.1 Experimental Investigations

To translate their outstanding nano-scale strain sensing properties to the macroscale, various scalable fabrication techniques, such as vacuum filtration [91], layer-by-layer [92], spray coating [93], in-situ polymerization [94], among others, have been employed. Extensive experimental studies have used different types of CNTs (*i.e.*, SWCNT [91, 95], double-walled CNT [96], and MWCNT [97-100]), various polymers (*e.g.*, epoxy [101], polyvinyl alcohol (PVA) [96, 102], and polyethylene oxide (PEO) [97]), dispersing methods (*e.g.*, tip sonication [92], magnetic stirring [103], and mechanical mixing [98]), and curing temperatures [104]. The general procedure is that, first, CNTs are uniformly dispersed in a polymer matrix without agglomeration; second, CNT-based nanocomposites are constructed through one of the bottom-up fabrication techniques mentioned previously.

The Raman shift behavior of CNTs was employed to realize bulk CNT-based strain sensors. Frogley *et al.* [95] dispersed SWCNTs in polyurethane acrylate (PUA) and showed a linear shift in the Raman band of the SWCNT-PUA nanocomposite under uniaxial tensile strains. Qui *et al.* [105] randomly dispersed 0.5 wt% SWCNTs in an epoxy matrix to assemble an SWCNT-based Raman strain rosette. In-plane strain measurements were achieved by an analytical model of the SWCNT Raman strain rosette based on the polarized Raman properties of SWCNTs. Although the results obtained helped explain that individual CNTs were being stretched when

tension was applied to the nanocomposites, Raman spectroscopy is not a practical tool for real-world strain sensing applications because it requires a bulky and elaborate setup.

As an alternative, the electrical characteristics (*i.e.*, resistance [91], capacitance [106], and impedance [92]) of CNT-based nanocomposites have been widely explored for strain sensing. For example, Lipomi *et al.* [106] assembled transparent and stretchable capacitive sensors composed of SWCNT-PDMS films to detect pressure and tensile strains. The sensor had a sandwiched structure of Ecoflex silicone elastomer between PDMS films with SWCNT films attached to them. When pressure or tensile strains were applied to the sensor, the distance between electrodes decreased, resulting in capacitance increase with a pressure sensitivity of 0.23 MPa^{-1} and a capacitive strain sensitivity of 0.004. Loyola *et al.* [92] used frequency-domain electrical impedance spectroscopy (EIS) to characterize the strain sensing performance of MWCNT-polyelectrolyte thin films deposited on glass fiber-reinforced polymer composites. The measured EIS data were fit to the parallel resistor-capacitor circuit model, and the results demonstrated that the resistance of resistive parameters (*i.e.*, series resistor and parallel resistor) increased while the capacitance of a capacitive parameter (*i.e.*, parallel capacitor) decreased.

Among the electrical components, many studies have investigated resistance-type CNT-based strain sensors. For example, Dharap *et al.* [91] produced SWCNT-based buckypaper strain sensors using a vacuum filtration method. The thin film was affixed to a brass specimen with a poly(vinyl chloride) (PVC) film in-between the two, and uniaxial tensile and compressive strains to $\pm$ 400 $\mu\varepsilon$ were applied to the specimen. Voltage was measured using a four-point probe method (*i.e.*, by interrogating the film using a constant amplitude direct current input), and linear changes in voltage was detected. Continued work [107] evaluated the flexural strain-sensing properties of these buckypapers by applying four-point bending (*i.e.*, pure bending). Similar to the previous tests, it was found that the voltage increased linearly from 0 to 200 mV when flexural strain

increased from 0% to 0.06%. Loh *et al.* [96] assembled mechanically strong SWCNT-PE thin films by the layer-by-layer method. The procedure entailed sequentially dipping a charged glass substrate in positively charged polycationic PE solution (*i.e.*, PVA or polyaniline (PANI)), followed by the negatively charged polyanionic solution with CNTs dispersed in poly(sodium 4-styrenesulfonate) (PSS) solution. The 20×10 mm^2 SWCNT-PSS/PVA thin films were affixed onto PVC coupons, and the film and PVC coupon specimens were subjected to tensile-compressive cyclic tests applied using an MTS-810 load frame. In this study, unpurified SWCNTs (u-SWCNTs) and purified SWCNTs (p-SWCNTs) were used to fabricate two different SWCNT thin films. The p-SWCNT-PSS/PVA thin films showed clear piezoresistive response, whereas u-SWCNT thin films showed poor response due to impurities inherent to u-SWCNT and their poor dispersion. In addition, their strain sensitivity was also sensitive to initial fabrication parameters, where higher CNT concentrations and better dispersion (enabled by higher concentrations of PSS) improved bulk film strain sensitivity.

Besides SWCNT-based nanofilms, MWCNTs have also been employed for their metallic electrical properties and lower costs [97-100]. Park *et al.* [97] assembled two concentrations (*i.e.*, 0.56 vol% and 1.44 vol%) of MWCNT-PEO thin films and measured their electrical resistance. The unstrained resistances of 0.56 vol% (*i.e.*, near the percolation threshold) and 1.44 vol% MWCNT-PEO thin films were 598 and 6.89 kΩ, respectively. When they were subjected to uniaxial tensile strains up to 1%, the electrical resistance increased linearly up to 0.8% strain for the 0.56 vol% MWCNT-PEO thin film and up to 1% strain for the 1.44 vol% MWCNT-PEO thin film before showing nonlinear response. Pham *et al.* [98] used a solution casting method and a dry blended method for embedding MWCNTs in a poly(methyl methacrylate) (PMMA) matrix. Uniaxial tensile strain tests (ε < 10,000 με) revealed that MWCNT-PMMA films became less sensitive to strain as the concentration of MWCNTs increased. MWCNT-PMMA films prepared

using different fabrication techniques had different electrical and electromechanical properties, such that MWCNT-PMMA nanofilms assembled by dry blending were more sensitive to applied strains than those made with solution casting. More recently, versatile additive manufacturing has been used to assemble MWCNT-based strain sensors [99, 100]. Christ *et al.* [99] assembled MWCNT-polyurethane (PU) composites using fused deposition modeling and showed their strain sensing responses while varying the MWCNT concentrations from 2 to 5 wt%. The 2 wt% MWCNT-PU nanocomposite showed the highest strain sensitivity of ~176, while the 5 wt% MWCNT-PU nanocomposite had ~8.6.

CNT-based nanocomposites have been applied to functionalize structural composites (*i.e.*, cementitious composites and fiber reinforced polymer composites) with self-sensing characteristics [108-110]. Thostenson *et al.* [108] dispersed MWCNTs in epoxy and infiltrated MWCNT-epoxy through a glass fiber preform. Cyclic loading-unloading with increasing maximum strains up to failure was applied to the MWCNT-based fiber composites. The results showed a linear piezoresistive response until microcracking caused deviations in their resistance response. Loh *et al.* [109] coated MWCNT-latex thin films onto sand particles and used them to cast mortar specimens. Two copper mesh electrodes were embedded in two ends of the 5×5×5 cm^3 specimen for electrical resistance measurement. The specimen was conductive with an unstrained electrical resistance of ~20 kΩ, since the MWCNT-latex coating offered conductive MWCNT networks in the specimen. The specimen was subjected to a 0.1 Hz cyclic-compressive load pattern up to 0.45 % peak strain, and the electrical resistance followed the pattern of compressive strains.

1.4.2 Numerical Simulations

Although a numerous experimental studies have been conducted to achieve high-performance CNT-based strain sensors, it has been reported that the electromechanical behavior

of CNT-based strain sensors is affected by various parameters (*i.e.*, CNT's intrinsic characteristics [111], polymer matrix [112], fabrication methods [113], curing temperature [93], and dispersion method [114]). Therefore, analytical investigations or numerical simulations were explored to advance the understanding of CNT-based nanocomposites and the relationship between parameters and their bulk electrical and electromechanical properties.

As a first step to explain the underlying mechanisms of the electromechanical properties of CNT-based strain sensors, there have been efforts to understand the electrical properties of CNT-based nanocomposites [115-120]. Zheng *et al.* [115] described an insulator-to-conductor phase transition (*i.e.*, percolation behavior) of CNT-polymer nanocomposites using the electrical percolation threshold (EPT), which was defined as a ratio of the number of percolation cases to the total number of simulations conducted. When an aspect ratio of CNT element was 300, the percolation threshold was calculated as ~4.5 wt%. Kumar *et al.* [116] derived a computational diffusive-transport model of a CNT-based thin film to simulate the dependence of conductance on the length of the CNT-based thin film model and showed a nonlinear dependence of conductance on the model length. Behnam *et al.* [117] used Monte Carlo simulations to study the relationship between different parameters (*e.g.*, CNT length, density, and resistance ratio) and the resistivity of a CNT-based thin film model. The simulation results demonstrated that the model resistivity decreased as CNT density and length increased. Other studies [118-120] have investigated how the morphology of dispersed CNTs (*i.e.*, alignment and dispersed shapes of CNTs) affect a bulk film's electrical properties. For example, Bao *et al.* [118] and Du *et al.* [120] demonstrated the effect of the alignment of CNTs on the bulk electrical conductivity. Bao *et al.* [118] dispersed 1D CNT elements in a representative cuboid (5.5 μm^3) and simulated electrical conductivity by considering the intrinsic resistance of CNTs and the contact resistance created by the electron ballistic tunneling approximated by the Landauer-Büttiker formula. As CNTs were more aligned

to the direction of the electrodes, the conductivity of the model decreased, as a result of the CNTs' inability to form a conductive path. Li *et al.* [119] used a 2D computational model to simulate the electrical conductivity according to the dispersed shapes of CNTs. Two different CNT geometries (*i.e.*, straight and curved) were considered, and lower conductivity of the 2D model was observed with curved CNTs.

Besides the electrical properties of CNT-based nanocomposites, there have been efforts to simulate their electromechanical or strain sensing performance. For example, Hu *et al.* [121] modeled a CNT as a soft-core element and randomly dispersed CNT elements in 3D space. Tunneling effect was considered as the critical parameter that determined electromechanical behavior while excluding the change in resistance of individual CNTs when strained. The numerical simulation results demonstrated higher strain sensitivity near the percolation threshold. A continued research study then applied tensile and compressive loading to the CNT-based nanocomposite model, and the model had better strain sensing performance in tension than in compression [114]. Similarly, Rahman *et al.* [122] incorporated an approximate tunneling resistance between neighboring CNTs in the model and demonstrated that numerical models with lower CNT concentration and CNT aspect ratios (*i.e.*, length-to-diameter ratio) exhibited higher strain sensitivity. Wang *et al.* [123] introduced average junction gap variation (AJGV), which is a function of Poisson's ratio of polymer and density, diameter, and orientation of CNTs, and showed that the piezoresistivity of the CNT-polymer composite can be improved by increasing the value of AJGV. Amini *et al.* [124] applied an approximate method of graph conductance theory to simulate the electromechanical behavior of a 3D mathematical model. Similar to Hu *et al.* [121], the numerical simulation results showed that a CNT film near its percolation threshold (*i.e.*, 2–3 wt%) had a higher strain sensitivity. In addition, the electrical properties deviated more at lower CNT concentrations as compared to that of high CNT concentrations.

1.4.3 Limitations of Current CNT-Based Strain Sensors

Despite the extensive research on CNT-based strain sensors, the underlying mechanisms of electromechanical response to applied strains are still poorly understood. First, parameters that affect their bulk strain sensing properties remain unclear. As mentioned before, experimental studies have shown that the electrical and electromechanical performance of CNT nanocomposites varied depending on the types of polymers and CNTs, fabrication and dispersion methods, and curing temperatures. For example, Loh *et al.* [96] found that unpurified CNT-based thin films performed poorly, whereas purified CNT-based thin films had much better strain sensing behavior. Mortensen *et al.* [93] studied how high-temperature treatment affected the electrical resistivity of spray fabricated MWCNT-PSS/polyvinylidene fluoride (PVDF) thin films. It was demonstrated that the thin films' resistivity decreased as the thermal annealing temperature increased from 100 to 250 ºC. Hu *et al.* [114] studied the effects of curing temperature and stirring rates of a planetary mixer on the piezoresistivity of MWCNT-epoxy nanocomposites. The curing temperature was varied from 80 to 120 ºC, and stirring rate was varied from 800 to 2,000 rpm. It was shown that the nanocomposite was more sensitive to strains with a lower curing temperature (80 Cº) and a higher stirring rate (2,000 rpm).

Except for a very few studies [114, 124], most studies focused exclusively on experiments or numerical simulations, and thus the linkage between experimental investigations and numerical simulations is missing. In addition, although numerical investigations were able to explain the general electromechanical or strain sensing behavior of CNT-based nanocomposites, they were limited in their explanation and representation of the various electromechanical behavior observed in experimental studies of CNT-based nanocomposites. Therefore, the accuracy of predicting the bulk-scale electromechanical behavior needs to be improved. For example, many numerical studies [114, 117, 118, 121, 122, 124] simplified the morphological features of CNT-based

nanocomposites such that CNTs were assumed to be straight with uniform length. However, experimental studies have found that CNT-based nanocomposites fabricated using different types of CNTs exhibited different electromechanical characteristics. Yin *et al.* [125] assembled MWCNT-epoxy nanocomposites using two different MWCNTs: MWCNT1 with a diameter of 10 nm, an aspect ratio of 500-1500, and purity of 95–98%; and MWCNT2 with a diameter of 40–90 nm, an aspect ratio of 100, and purity of > 99.5%. The electrical and electromechanical characteristics of the two types of MWCNT-epoxy nanocomposites were different. First, 10% MWCNT2-epoxy nanocomposites were much more conductive (95.2 S/m) as compared to 10% MWCNT1-epoxy nanocomposites (0.00533 S/m). In addition, the average strain sensitivity of 10% MWCNT1-epoxy nanocomposites was 4.3 while that of 10% MWCNT-epoxy nanocomposite was 3.2.

1.5 Dissertation Objectives and Outline

As previously discussed in Section 1.4, there is a dire need for an experimentally validated numerical model of CNT-based thin films that can help advance the understanding of the underlying mechanisms that affect their bulk electrical and electromechanical properties. Thus, the primary objective of this dissertation is to derive an experimentally validated numerical model of CNT-based thin film strain sensors. Advanced microscopy techniques (*i.e.*, STEM, SEM, AFM, and TEM) have allowed researchers to precisely observe the geometry of nanostructured material. AFM and SEM will be employed to measure the physical characteristics of as-dispersed CNTs in a polymer matrix. With advanced nanotechnology and various fabrication techniques, CNT-based strain sensors possess great potential to obtain tailorable strain sensing properties. However, the lack of optimization or a design tool prevents such innovation. Therefore, this thesis also explores

numerical models to guide the design of CNT-based distributed strain sensors, which will be achieved by leveraging the principles of electrical time-domain reflectometry (ETDR).

In Chapter 2, a 2D numerical simulation model of a CNT-based thin film will be derived based on percolation theory. Straight 1D CNT elements with a predefined length will be located by positioning CNTs at random locations, which describes the random dispersion of CNT networks. This chapter will evaluate the effects of different parameters (*i.e.*, lengths and density of CNTs and intrinsic piezoresistivity of CNTs) on the electrical and electromechanical properties of CNT-based thin film models. The electrical properties of the thin film model will be evaluated by calculating percolation probability and nominal electrical resistance. To assess the electromechanical performance of the CNT-based thin film model, it will be subjected to different loading conditions. The chapter will especially focus on investigating the piezoresistive behavior near the percolation threshold where the percolation probability is ~50%.

Chapter 3 seeks to enhance the accuracy of the CNT-based thin film models. In fact, the majority of numerical simulation research assumed the geometry of CNTs is straight with a certain length. However, experimental studies have reported different strain sensing behaviors depending on the type of CNTs. This chapter will address this knowledge gap by looking at ultra-low concentration MWCNT-PSS thin films to assess the morphology and physical characteristics of as-deposited MWCNTs. AFM images of the MWCNT-PSS thin films will be obtained, followed by image analysis to measure the physical characteristics of MWCNTs (*i.e.*, dispersed MWCNT shape and length distribution). The measurement results will be integrated in the model, and models with different morphologies of CNT networks will be simulated.

In Chapter 4, experimental validation of the CNT-based thin films will be conducted. Seven different concentrations of MWCNT-pluronic thin films are assembled through vacuum filtration. SEM images will be obtained to characterize the dispersed shape of MWCNTs, which will be then

integrated into the model. The electrical properties of the model and the MWCNT-pluronic thin films will be compared by measuring their electrical resistance. Next, different strain patterns will be applied to the model and the MWCNT-pluronic thin films to compare their electromechanical responses. Besides investigating similarities between simulations and experiments, further validation of the numerical model will be achieved by comparing the area ratio of the numerical models and SEM images of the MWCNT-pluronic thin films.

Chapter 5 explores the use of numerical simulation models to guide the design of an MWCNT-based distributed strain sensor. A new approach to achieve distributed sensing will be achieved by integrating the principle of ETDR and MWCNT-based sensing elements. ETDR involves transmitting an electromagnetic wave from one end of a transmission line and then observing characteristics of the reflected signals. The proposed ETDR sensor will be constructed by replacing portions of a transmission line with sensing elements that is composed of MWCNT-based dielectric and conducting parts. Different CNT thin film models characterized by different nanostructures will be numerically simulated and compared. Based on numerical simulation results, ETDR-based distributed strain sensors will be assembled by incorporating different MWCNT-based thin films. Then, their distributed strain sensing performance will be evaluated by applying strain patterns to each sensing element and measuring the corresponding reflected waveform response. In addition, the strain sensing behavior of different designs of ETDR sensors will be compared.

Chapter 1, in part, is a reprint of the material as it appears in Strain Sensing and Structural Health Monitoring using Nanofilm and Nanocomposites, Elsevier, Bo Mi Lee; Sumit Gupta; Kennth J. Loh; Satish Nagarajaiah, 2016. The dissertation author was the primary author of this book chapter.

Chapter 2.

A 2D CNT Thin Film Model Based on Percolation Theory

2.1 Introduction

The primary objective of this chapter was to derive a 2D CNT-based thin film model based on percolation theory to understand the electrical and coupled electromechanical behavior of CNT-based thin films. A major focus of this chapter was to investigate, through numerical simulations, how changes in the intrinsic piezoresistivity of individual nanotubes would affect the electromechanical behavior of the nanocomposite. Early experimental investigation by Tombler *et al.* [89] demonstrated that the conductance of a metallic SWCNT decreased by more than two orders of magnitude when the tube was strained via three-point bending applied by an AFM tip. Likewise, Jang *et al.* [126] detected linear changes in resistance when both sides of an MWCNT were stretched by tungsten tips. However, it remains unclear how the piezoresistivity of individual tubes affect and propagate to large-scale systems such as percolated nanotube networks.

In this chapter, the model was derived by positioning 1D CNT elements at random locations to generate a CNT network. The electrical properties of the thin film model were evaluated by calculating percolation probability and nominal electrical resistance. To assess the electromechanical performance of the CNT-based thin film model, it was subjected to loading conditions. In particular, special attention was paid to assess the models' piezoresistive properties when the simulated film was near its percolation threshold (as defined by the percolation probability being ~50%). Three different CNT gage factors were considered, which were based on results reported in the literature. Uniaxial tensile-compressive cyclic loads were applied to the nanocomposite model, and its electromechanical properties (such as bulk film strain sensitivity) were calculated and compared. This chapter begins with a discussion of the percolation-based model, assumptions, and boundary conditions. Second, the method used for calculating thin film resistance was presented. Then, the results of the electrical and electromechanical performance simulations were discussed, followed by a brief summary.

2.2 Percolation-based Model and Simulation Procedures

2.2.1 Percolation Theory

Percolation theory was introduced by Broadbent and Hammersley [127, 128] in 1957 to explain phase transition of a permeable 3D box. They demonstrated that low concentrations of fluid could not flow through the permeable box until the fluid concentration reached a certain percolation threshold. Later in 1973, Kirkpatrick [129] applied percolation theory to describe, through numerical modeling, phase transition (*i.e.*, insulator-to-conductor) of conductive particle-based composites.

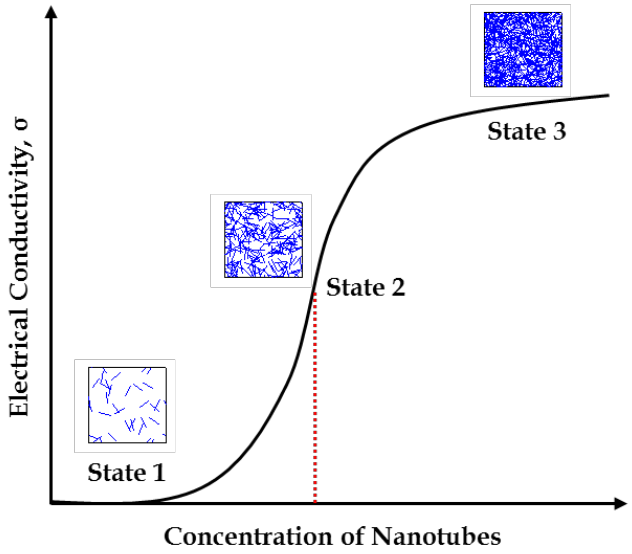

Figure 2.1. The electrical conductivity of CNT-based nanocomposites follows percolation theory and can be classified by three different states. State 1 is an electrically insulating state where very few nanotubes are distributed nor connected to one another. State 2 experiences dramatic increases in conductivity as a result of the creation of at least one or a few electrically conductive pathways between opposite electrodes. State 3 consists of a dense network of electrically conductive paths.

Similar to these early investigations, one can also expect the same insulator-to-conductor phase transition with the incorporation of electrically conductive nanotubes embedded in an insulating polymer matrix. In particular, three different states can be investigated depending on the concentration of nanotubes. The first state corresponds to when that of the insulating polymer matrix is dominating the electrical properties of the nanocomposite (Figure 2.1). Since very few conductive nanotubes are embedded in the polymer matrix, a continuous conductive pathway for electrical current to flow from one end of the nanocomposite to the other does not exist. As the concentration of nanotubes increases, they start to create electrically conductive clusters, which are formed by direct nanotube-to-nanotube junctions or other electron transport mechanisms between neighboring CNTs (*e.g.*, tunneling). At the second state, with the addition of more nanotubes, the clusters are finally able to connect and form an electrically conductive path between the two opposite electrodes (Figure 2.1). After the formation of one conductive pathway, any

additional nanotubes will induce dramatic increases in conductivity of the nanocomposite (*i.e.*, due to more routes for current flow). The minimum concentration of nanotubes that causes a remarkable increase in bulk film electrical conductivity (*i.e.*, the transition from an insulator to conductor) is defined as the percolation threshold. The final state corresponds to the case with high CNT concentrations (Figure 2.1). Here, a dense network of electrical conductive paths exists, and electrical conductivity increases gradually and finally saturates.

2.2.2 Model Generation

To investigate the electrical and electromechanical properties of CNT-based nanocomposites, a 2D percolation-based model was derived by randomly distributing straight 1D nanotubes of a predefined length (L_{CNT}). The concentration of nanotubes (N) and the dimensions of the 2D thin film model (*i.e.*, length, L and width, W) were specified. The location of each nanotube was identified by two end-points, namely (x_1, y_1) and (x_2, y_2), as represented in a Cartesian coordinate system. The first end-point, (x_1, y_1), was determined using a random number generator (*e.g.*, "rand" in *MATLAB*). The other end point, (x_2, y_2), was then calculated using the prescribed nanotube length and a randomly generated CNT orientation (θ):

$$x_2 = x_1 + L_{CNT}\cos\theta \tag{2.1}$$

$$y_2 = y_1 + L_{CNT}\sin\theta \tag{2.2}$$

This procedure was reiterated until the exact number of nanotubes desired (N) was included in the model. A representative numerical model with 400 CNTs in a 1×1 μm^2 area is shown in Figure 2.2.

In a previous study, if a portion of the nanotube exceeded the boundary of the thin film model, that portion of the CNT was eliminated so that all the nanotubes fit inside the modeling domain [130]. In contrast, this study employed periodic boundary conditions (PBC) commonly

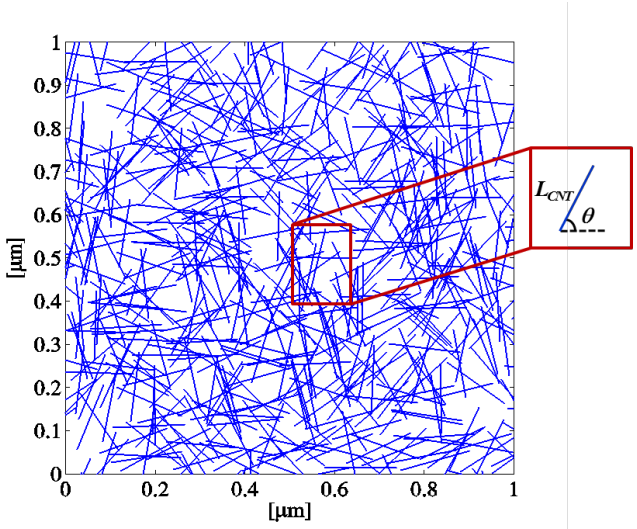

Figure 2.2. CNTs were randomly distributed in the representative 2D unit area model (1×1 µm^2) with a prescribed nanotube length (L_{CNT} = 0.16 µm), nanotube concentration (N = 600), and the use of PBCs.

used in creating representative volume elements (RVE) [131-133]. In short, PBCs ensured the portion of randomly placed CNTs that exceeded the thin film boundary would appear on the opposite edge of the film, as shown in Figure 2.3. The implementation of PBCs also ensured that the predetermined density or number of nanotubes was maintained. Hill *et al.* [134] explained that the characteristics of materials can be represented by an RVE, including sufficient amounts of inclusions. Odegard [131] mentioned that an RVE could represent the entire structure of the material in a statistical sense. In fact, RVE was widely employed for simulating the mechanical properties of composite materials [131-134]. The generated model shown in Figure 2.2 utilized PBCs. It should be mentioned that the models employed in this study were assumed to be representative of a randomly selected location of a bulk film. Therefore, its electrical and electromechanical properties would also be statistically representative of the entire system [113].

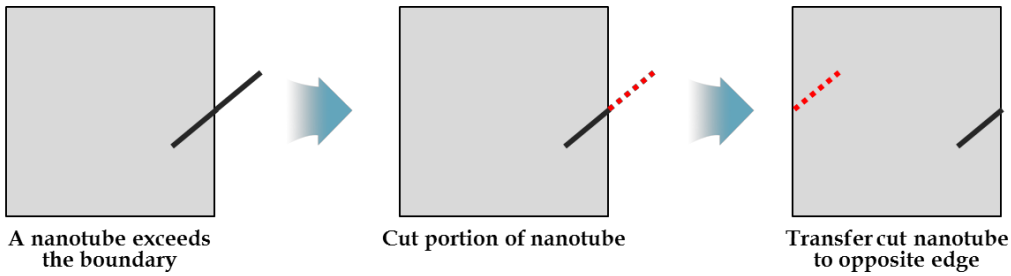

Figure 2.3. PBCs were implemented in this study by cutting the nanotubes that exceeded the model boundary and then transferring them to the opposite edge.

2.2.3 Electrical Property Simulations

Upon generating the nanotubes in the model, junction locations were identified. A junction was defined as the location where nanotubes intersected one another. A soft-core model was considered such that CNT elements could penetrate one another [121, 135]. In doing so, intersecting nanotubes that formed junctions remained within the same 2D plane. On the other hand, since the nanotubes employed in this work were straight, they could also be expressed as linear equations. Therefore, the locations of junctions were located by simply solving sets of linear equations, and the results were stored in a junction matrix. Junction locations and corresponding segment numbers were stored in a matrix.

In addition to being linear elements, each CNT was considered as a resistive element. Therefore, after the junction locations were identified, the equation used for calculating a nanotube's resistance (R) between junctions was defined as shown in Equation 2.3 [117, 136]:

$$R = R_i + R_{jct} + R_{Ohmic} \tag{2.3}$$

where R_i is the theoretical intrinsic resistance of a ballistic SWCNT with an approximate value of 6.5 kΩ, R_{Ohmic} is Ohmic resistance, and R_{jct} is junction resistance. Ohmic resistance (R_{Ohmic}) is caused by carrier scattering due to defects, impurities, and phonons and is defined in Equation 2.4 [137]:

$$R_{Ohmic} = \left(\frac{h}{4e^2} \right) \frac{L_n}{l} \tag{2.4}$$

where h is Plank's constant, e is the electron charge, l is an electron's mean free path length (which is assumed to be 1 μm), and L_n is the conductor length (which is the length of the CNT between two junctions). Junction resistance (R_{jct}) depends on the electrical properties of SWCNTs (*i.e.*, metallic or semiconducting depending on its chirality [4]) that comprise the junction [138]. Despite these complexities, this study assumed that all CNTs were metallic to be consistent with the use of MWCNTs in the aforementioned experiments, and only metallic-metallic junctions (R_{jct} = 98 kΩ) existed [116, 117, 139].

Then, each nanotube's resistance was incorporated to determine the resistance of the entire CNT-network by formulating a conductance matrix for analyzing the thin film's electrical properties. The reciprocal of CNT resistance, which is conductance, was used to construct the conductance matrix, [G]:

$$\left[G\right] = \begin{bmatrix} g_{11} & \cdots & g_{1i} & \cdots & g_{1n} \\ \vdots & \ddots & & & \vdots \\ g_{i1} & & g_{ii} & & g_{in} \\ \vdots & & & \ddots & \vdots \\ g_{n1} & \cdots & g_{ni} & \cdots & g_{nn} \end{bmatrix} \tag{2.5}$$

where the diagonals (g_{ii}) are the summation of the conductance values connected to junction i, and the non-diagonal terms (g_{ij}) are the negative of the summation of the conductance values between junctions i and j. [G] is a square matrix of order n, which is equal to the total number of junctions. Then, for the models investigated in this study, it was assumed that the electrodes were located on the top and bottom edges of the thin film model shown in Figure 2.2. A potential difference of 10 V was applied across the electrodes to excite the system.

Using [G] and the applied voltage, Kirchhoff's current law and the conductance version of Ohm's law were then used to determine the resistance of the entire CNT-network. Kirchhoff's current law states that the summation of electrical current, both input and output, at each node (or at any point) is equal to zero. The conductance version of Ohm's law expresses the conventional Ohm's law using conductance in lieu of its reciprocal or resistance. Thus, the entire resistance network can be expressed using Kirchhoff's current law in terms of conductance (Equation 2.6) [117, 137].

$$[G]\{v\} = \{c\} \tag{2.6}$$

where $\{c\}$ is the equivalent current vector and $\{v\}$ is the nodal voltage vector. The nodal voltage vector was then solved with $[G]$ and $\{c\}$. With these results, the total current was calculated using nodal voltage and the resistive nanotube elements connected to the drain (0 V). Finally, the resistance of the entire nanotube network was evaluated using the total current and the applied voltage.

2.2.4 Electromechanical Response Simulation

In addition, deformations were also applied to the thin film model for evaluating its electromechanical or strain sensing properties. To be specific, uniaxial tensile and compressive strains to ±0.01 (in 0.0025 increments) were applied in the direction of the *y*-axis (Figure 2.2), and the electrical properties at each strain state were calculated. The model was assumed to be homogeneous and isotropic, and the strain was applied uniformly to the entire film. This assumption greatly simplified computations by neglecting the CNT-matrix interfaces, especially since it has been shown from finite element models that stress concentrations would exist at the terminating ends of each tube [140]. Regardless, the coordinates of each strained CNT were then updated. The electrical resistance of the strained CNT-network was subsequently calculated

following the aforementioned procedure. In essence, the application of strain deformed each nanotube and altered its orientation. The coordinate of each deformed nanotube was then updated accordingly using Equations 2.7 and 2.8:

$$x' = x - \nu\varepsilon(x - \frac{W}{2}) \tag{2.7}$$

$$y' = y(1 + \varepsilon) \tag{2.8}$$

where x and y are the initial coordinates, x' and y' are the updated coordinates, and ν is Poisson's ratio. The coordinate (0.5W, 0) was fixed, and the remainder of the film deformed accordingly and relative to this point. The Poisson's ratio of the nanocomposite was assumed to be that of typical polymers (*i.e.*, 0.34), even though an exact type of polymer matrix was neither specified nor modeled. Upon doing so, the resistance of the entire CNT network was calculated following the same procedure outlined in the previous section and before the model was subjected to a different magnitude of applied strain. It should be mentioned that only models whose CNT concentrations or densities that exceeded the percolation threshold were considered. The model's resistance was then correlated to different magnitudes of applied tensile and compressive strains for studying its electromechanical properties.

As mentioned before, an objective of this chapter was to quantify the effects of different CNT gage factors or strain sensitivities (S_{CNT}). In general, the definition of strain sensitivity (S) or gage factor is as follows:

$$S = \frac{\Delta R / R_0}{\Delta\varepsilon} \tag{2.9}$$

where R_0 is the initial unstrained resistance, ΔR is the change in resistance between the strained and unstrained states, and $\Delta\varepsilon$ is the change in applied strain. It is known that materials such as copper and aluminum are characterized by S = 2.2 and 2.5, respectively [88]. In contrast, CNTs

exhibit significantly higher gage factors as compared to conventional materials. Cao *et al.* [141] experimentally measured the intrinsic strain sensitivities of nanotubes and showed three different strain sensitivities of nanotubes (*i.e.*, S_{CNT} = 60, 150, and 1,000). In this work, the numerical model assumed three different nanotube strain sensitivities (*i.e.,* S_{CNT} = 1, 60, and 150). These strain sensitivity assumptions affected the Ohmic resistance of each CNT, as was described in Equation 2.4. When S_{CNT} = 1 which was the control case, the nanotube's Ohmic resistance would only depend on its length, which is directly related to the level of applied strain.

2.3 Results and Discussions

2.3.1 Nominal Electrical Properties

The percolation behavior of the proposed CNT-based model was evaluated using percolation probabilities. Percolation probability is defined as the probability that the CNT-based nanocomposite would possess at least one conductive path between the source and drain electrodes, thereby enabling it to conduct electrical current from one end of the film to the other. Percolation probability (P) can be calculated using Equation 2.10 [115]:

$$P = \frac{n_p}{n_t} \tag{2.10}$$

where n_t is the total number of simulations, and n_p is the number of cases in which the model is electrically conductive. In this study, three different CNT lengths were considered (L_{CNT} = 0.14, 0.16, and 0.18 μm); it should be clarified that each simulation only considered one specific length. In addition, for each prescribed nanotube density case (*i.e.*, N nanotubes defined in the given model

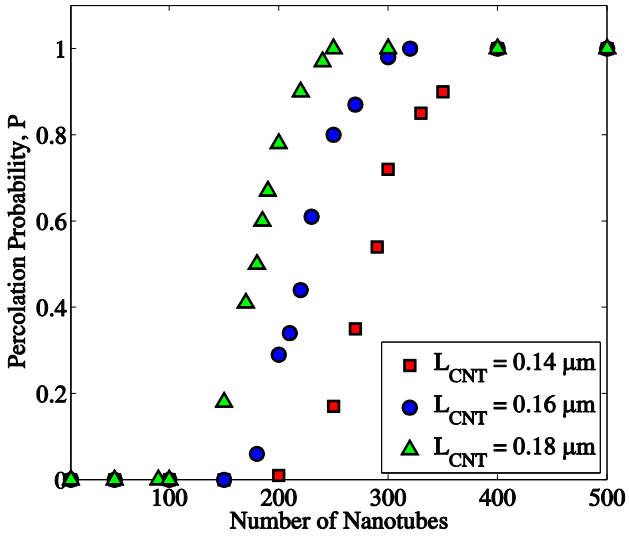

Figure 2.4. The percolation characteristics of 1×1 μm^2 CNT-based nanocomposite models were evaluated as a function of nanotube concentration. Three different nanotube lengths (L_{CNT} = 0.14, 0.16, and 0.18 μm) were considered.

space), 100 simulations were conducted (n_t = 100). Nanotubes were randomly deposited in a 1×1 μm^2 area. The EPT was then defined as the density of nanotubes when the CNT-based nanocomposite experienced dramatic increases in conductance and corresponded to 50% percolation probability [115].

The percolation simulation results are shown in Figure 2.4. It can be observed that, as L_{CNT} increased, the number of nanotubes (or N) required for creating an electrically conductive model decreased; fewer number of CNTs were also needed to attain EPT. Specifically, when the length of nanotubes increased from 0.14 to 0.18 μm, the number of nanotubes corresponding to EPT decreased from 290 to 180, respectively. Similarly, to reach a percolation probability of 100%, N decreased from 400 to 250. This result was expected, since the length of CNTs was equivalent to the length of the electrical conductor, and longer nanotubes had greater probabilities of intersecting another nanotube to create at least one conductive pathway that spanned from the source to the drain. These results were also consistent with other experimental and numerical investigations

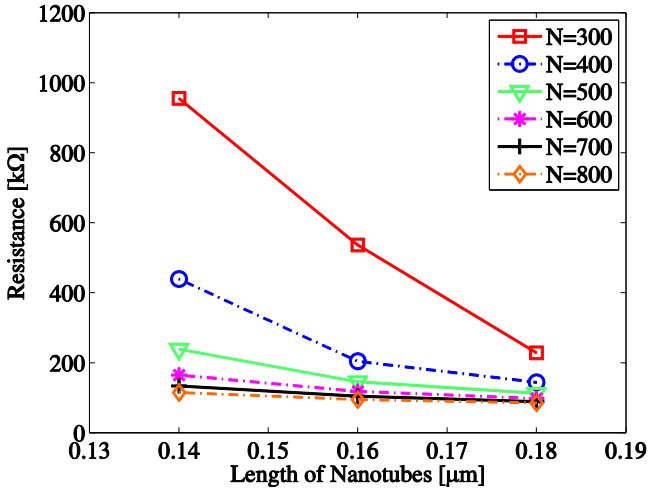

Figure 2.5. The nominal unstrained resistances of 1×1 μm^2 CNT-based nanocomposite models were evaluated with different nanotube lengths (L_{CNT} = 0.14, 0.16, and 0.18 μm) and concentrations (N).

reported [115, 124]. In addition, the percolation probability results shown in Figure 2.4 were used for guiding the electrical and electromechanical simulations, as will be presented next; in these cases, only percolated thin film models that were electrically conductive were of interest.

A percolated CNT-based thin film model would be characterized by certain electrical properties, namely resistivity and conductivity. Various parameters such as nanotube length, density, aspect ratio, fabrication method, and the polymer matrix could influence the electrical properties of nanocomposites [117, 142]. Despite the plethora of different parameters, this study considered two, specifically CNT length (where L_{CNT} = 0.14, 0.16, and 0.18 μm as mentioned earlier) and nanotube density (where N = 300 to 800, in 100 increments). Figure 2.5 summarizes the results after running numerous simulations (*i.e.*, 20 for each unique case) corresponding to different CNT lengths and densities. It can be seen from Figure 2.5 that the resistance of the model decreased with the incorporation of longer nanotubes and with a denser nanotube network. These results were expected, because first, longer nanotubes had greater likelihood of intersecting with other nanotubes to create larger numbers of conductive pathways for a given CNT density.

Similarly, by increasing the number of nanotubes within the same 2D area, more conductive pathways could also be formed, thereby increasing electrical conductivity (or decreasing resistivity). It should be noted that, as L_{CNT} and N continued to increase, the bulk film resistance began to plateau due to saturation of the number of electrical conductive pathways (Figure 2.5).

2.3.2 Electromechanical Response

As mentioned earlier, the electromechanical properties of the thin film model were also investigated by calculating how the models' electrical properties varied with different magnitudes of applied strains. To investigate more realistic thin film models that were comparable to ones used for strain sensing applications, CNTs were deposited within a 0.5×5 μm^2 space, and PBCs were employed again. In addition, CNTs were assigned with three different intrinsic nanotube strain sensitivities, namely S_{CNT} = 1, 60, and 150. Finally, the thin film model was subjected to uniaxial tensile-compressive cyclic strains to ±1% (in 0.025% increments), and its electrical resistance was calculated at every strain step. It should be noted that the model aimed to simulate a representative element of an actual thin film rather than the entire film subjected to electromechanical testing.

Figure 2.6a shows a representative set of results corresponding to the case of a thin film model (with S_{CNT} = 150, L_{CNT} = 0.28 μm, and N = 700) subjected to cyclic loading. Figure 2.6a shows the applied one-cycle load pattern to ±1%. Furthermore, the normalized change in resistance of the film (R_{norm}) was overlaid in Figure 2.6a, and R_{norm} was calculated by:

$$R_{norm} = \frac{\Delta R}{R_0} \tag{2.11}$$

where R_0 is the initial unstrained or nominal resistance, and ΔR is the change in resistance between the strained and unstrained states. The fact that the model's electrical resistance changed in response to strain confirmed the electromechanical properties observed by many other research

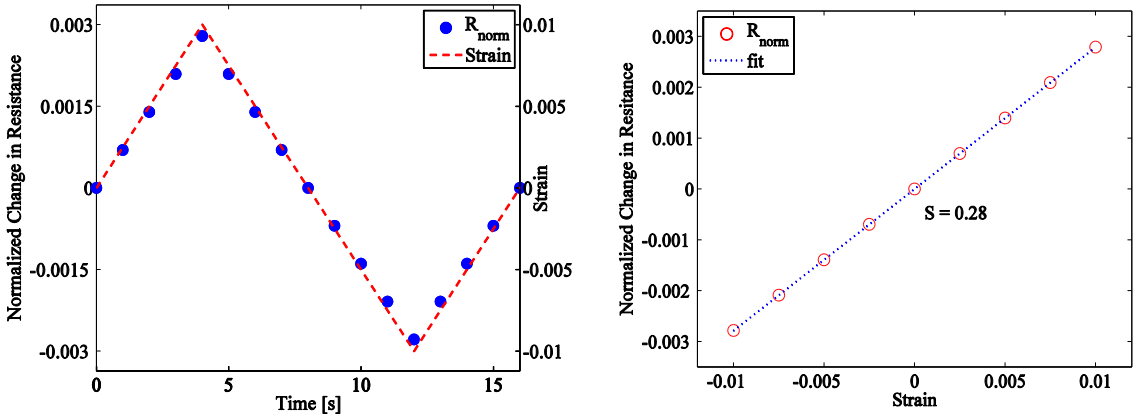

Figure 2.6. (a) The CNT-based nanocomposite model (0.5×5 μm^2) exhibited linear piezoresistivity when subjected to a one-cycle tensile-compressive strain pattern to ±1%. The model assumed that S_{CNT} =150, L_{CNT} = 0.28 μm, and N = 700. (b) The corresponding film's normalized change in resistance was plotted as a function of strain, and the strain sensitivity of this model was 0.28.

groups. Figure 2.6b plots the normalized change in resistance as a function of applied strains. From Figure 2.6b, one could conclude that the normalized change in resistance varied linearly when the film was strained in both tension and compression. A linear least-squares regression line was also fit to the normalized change in resistance data shown in Figure 2.6b to demonstrate the model's strong linearity. The strain sensitivity of each thin film specimen can then be estimated from the slope of the linear least-squares regression line. It should be noted that many other CNT-based thin film models also exhibited such linearity. Similar electromechanical properties were also observed in numerous other experimental studies [91, 96, 143, 144].

Despite the similarities, the model employed in this study only investigated a small representative element of what was typically tested in the aforementioned experimental studies and not the entire film. In addition, the conditions of the model were specific to films under perfectly uniform, uniaxial, tensile-compressive cyclic loading. In experiments, such ideal conditions may not exist, so comparison of numerical and experimental results needs to be

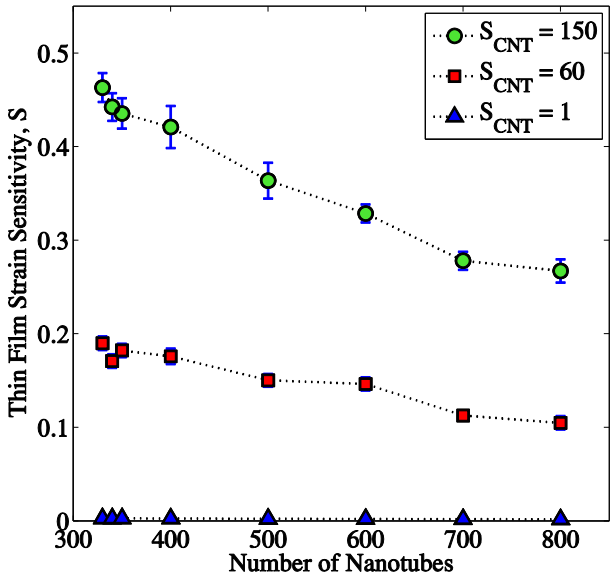

Figure 2.7. The strain sensitivities of 0.5×5 μm^2 CNT-based thin film models with three different intrinsic CNT gage factors (S_{CNT} = 1, 60, and 150) and different nanotube concentrations were determined. The average strain sensitivities and corresponding error bars (*i.e.,* standard error of the mean) are shown.

performed with caution. This is particularly true for freestanding films subjected to tensile tests where non-uniform stress distributions could occur near its boundaries. However, such effects can be negligible if the specimen tested is large enough such that the majority of the film is subjected to uniaxial loading. In this case, the model results can serve as a good comparison.

Upon executing all the different numerical simulations that employed different numbers of nanotubes, lengths, and intrinsic strain sensitivities, the results are summarized in Figure 2.7. The lowest nanotube concentration (*i.e.*, N = 330) for the thin film strain sensitivity simulation was chosen based on percolation probability results in which percolation probability was ~50%. Here, each data point corresponds to the average strain sensitivity determined from 20 simulations; the only exception was those cases in which the films were near the percolation threshold, and 40 simulations were conducted. From Figure 2.7, it can be observed that, when S_{CNT} = 1, the strain sensitivity of the bulk film was very low and decreased marginally as CNT density or N was

increased. On the other hand, clear trends could be identified for the other two cases when S_{CNT} = 60 or 150. As N was increased from 330 to 800, bulk film strain sensitivity decreased. It should be noted that with higher CNT gage factors (*i.e.*, S_{CNT} = 150), bulk film strain sensitivity was also higher as compared to films with the same CNT concentration but with a lower intrinsic CNT gage factor. When CNT strain sensitivity was 1, the film's resistance response only depended on changes in nanotube lengths. On the other hand, with larger S_{CNT}, resistance changes were amplified to result in high bulk film strain sensitivities, which were consistent with other experimental and numerical studies [98, 124, 145]. However, regardless of S_{CNT}, the same trends existed in which strain sensitivity decreased with increasing CNT density.

This study also investigated how bulk film strain sensitivities varied near percolation and when even longer nanotubes were incorporated. Similar to previous cases, CNTs were deposited within a 0.5×5 μm^2 space. On the other hand, the length of nanotubes was varied as follows, where L_{CNT} = 0.213 to 0.53 μm for N = 500, and L_{CNT} = 0.195 to 0.4 μm for N = 600. Numerical simulations of films subjected to tensile-compressive loading were conducted, and the strain sensitivities corresponding to the different cases were calculated as before. It should be noted that the shortest CNT length was also decided based on percolation probability results; specifically, the shortest nanotube length corresponded to the case that yielded only 50% percolation probability. Here, a total of 20 simulations were performed for each CNT density case, except 30 simulations were conducted near the percolation threshold.

The strain sensitivity results are shown in Figure 2.8. Similar to the results shown in Figure 2.7, strain sensitivity decreased as nanotube length increased. The major difference observed in this case, however, was strain sensitivity near percolation. Here, the trend near percolation was inconsistent, where it appeared that strain sensitivity peaked not when percolation probability was 50% but at higher values (*i.e.*, still close to percolation). It should be noted that inconsistent strain

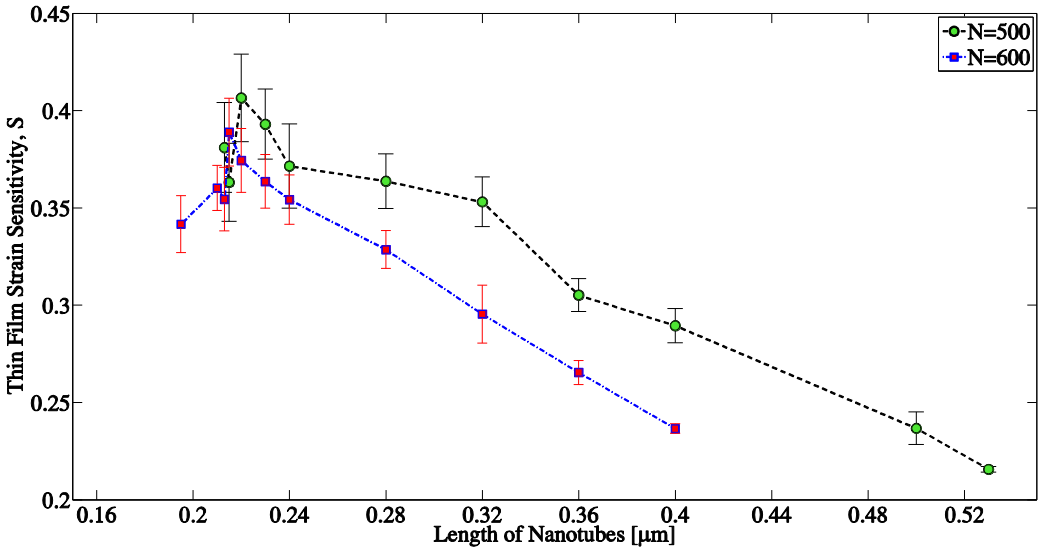

Figure 2.8. The average bulk film strain sensitivities were estimated as a function of nanotube length. Two different nanotube concentration cases (*i.e.*, $N = 500$ and 600) were considered, and their corresponding error bars (*i.e.*, standard error of the mean) are also plotted.

sensitivity near the percolation threshold was clearer for strain sensitivity results as a function of nanotube lengths (Figure 2.8) than that of nanotube concentration (Figure 2.7). A possible explanation could be due to the inherent randomness of the model, where the electrical and electromechanical properties were affected by how CNTs were distributed in the film. As a result, models close to percolation (*i.e.*, with low CNT densities) would be sensitive to special cases that could occur. Amini *et al.* [124] demonstrated through numerical modeling that, when the concentration of MWCNTs was near the percolation threshold, the electrical properties deviated more than that of higher MWCNTs concentrations. One could infer that higher strain sensitivities could be acquired near the percolation threshold, but the repeatability would be lower as compared to relatively higher nanotube concentrations [124].

2.4 Summary

In this study, 2D percolation-based computational models were developed to investigate the electrical and electromechanical properties of CNT-based nanocomposites. First, straight nanotubes were randomly distributed in a 2D representative area of a thin film. Then, CNT junction locations were found by solving sets of linear equations that defined the position and orientation of each nanotube. With the nanotube resistor network defined and the location of junctions known, the electrical resistance of the entire model was then calculated using Kirchhoff's current law and the conductance version of Ohm's law. The numerical model was then subjected to uniaxial tensile-compressive cyclic strains in an effort to study the electromechanical responses of the nanocomposite system. In particular, the objective was to characterize how the electrical properties of the thin film model would vary depending on different CNT lengths, densities, and intrinsic CNT piezoresistivity considered.

First, the numerical model was used for investigating percolation properties. It was found that the electrical percolation threshold decreased with the incorporation of longer nanotubes, since longer CNTs possessed a greater probability of intersecting with another longer tube in its vicinity. Second, the unstrained or nominal electrical resistance of nanocomposites with different CNT lengths and densities were determined. The results showed that electrical resistance decreased with the incorporation of longer nanotubes and at higher nanotube concentrations, both of which were expected. Finally, the thin film's electromechanical or strain-sensitive properties were also studied. It was found that the bulk film's resistance increased with increasingly applied tensile strains, and the opposite was also true (*i.e.*, the resistance decreased with greater compression). The results also showed that strain sensitivity decreased with increasing CNT lengths, regardless of their intrinsic gage factor used. However, this trend was not true when the film was close to the percolation threshold.

Chapter 2, in full, is a reprint of the material as it appears in *Journal of Material Science*, Bo Mi Lee; Kenneth J. Loh, 2015. The dissertation author was the primary researcher and author of this paper.

Chapter 3.

Thin Film Strain Sensor Models Assembled using Experimentally Extracted Features

3.1 Introduction

To date, many researchers have sought to take advantage of micro- or nano-scale images obtained by SEM, TEM, and AFM to characterize CNT-based thin films. For example, Dharap *et al.* [91] and Loh *et al.* [96] employed SEM for investigating the quality of nanotube dispersion in thin films. The CNTs' physical properties (*i.e.*, nanotube length and diameter) can then be estimated from these SEM images, but the challenge is that they form complex 3D networks, and it is often difficult to identify the start- and end-points of individual nanotubes.

Gommes *et al.* [146] used TEM images of MWCNTs to measure their inner and outer radii. It was shown that annealing at 2,500 °C decreased MWCNT lengths. Tenent *et al.* [147] dispersed SWCNTs in a sodium carboxymethyl cellulose (CMC) aqueous solution and varied sonication times (*i.e.*, 10 and 60 min). Diluted SWCNT-CMC solution was spin-coated to form SWCNT-

CMC thin films on silicon. Then, the lengths of 300 SWCNTs in the thin films were measured using AFM and Gwyddion software. The results showed that SWCNTs subjected to 60 min of sonication (which yielded a mean length of 0.55 μm) were significantly shorter than those treated with 10 min of sonication (where mean SWCNT length was 1.32 μm). Instead of focusing on individual CNTs, Timmermans *et al.* [148] characterized the morphology of SWCNT-networks fabricated using four different techniques, namely electrostatic precipitation, thermal precipitation, press transfer from a filter, and dissolving the filter. The SEM images clearly showed different morphological features of SWCNT-networks depending on the particular fabrication method employed. These experimental studies revealed that the physical features of CNTs (*i.e.*, CNT length, diameter, and dispersed geometry of CNT network) were varied depending on the types of CNTs, sonication times, fabrication methods, annealing temperature, and so on.

In the previous Chapter, the morphological features of CNT-based nanocomposites were somewhat simplified, where CNTs were assumed to be straight and of uniform length. Therefore, the objective of this Chapter was to derive a 2D CNT-based thin film model that could adequately describe the electrical and electromechanical properties of a specific type of CNT-based nanocomposite thin film. Instead of making arbitrary assumptions, CNTs' physical properties, as-dispersed and deposited shapes, and statistical distributions of CNT lengths, were obtained from direct experimental measurements and then incorporated in the percolation-based model. This Chapter starts with a discussion about the fabrication of ultra-low-concentration MWCNT-PSS thin films. Then, AFM images of MWCNT-PSS thin films were obtained to resolve the individual nanotubes deposited. Image analysis and processing were employed to characterize CNT length distributions and their preferential deposited geometric shapes. These results were incorporated in the 2D numerical model, and their electrical and strain sensing properties were subsequently computed and evaluated.

3.2 Carbon Nanotube Characterization

3.2.1 Materials

MWCNTs were purchased from SouthWest NanoTechnologies with a reported median outer diameter of 10 nm, median length of 3.0 μm, and purity >99%. PSS ($M_W \approx$ 1,000,000) was acquired from Sigma-Aldrich.

3.2.2 AFM Sample Preparation

MWCNT-PSS thin films were prepared for AFM characterization so as to investigate the morphology and physical characteristics of dispersed and as-deposited MWCNTs. MWCNT-PSS thin film assembly started with the preparation of 1 *wt.*% PSS aqueous solution. PSS powder was dissolved in deionized (DI) water by 60 min of bath ultrasonication (135 W, 42 kHz). Then, 1 mg/mL of MWCNTs was dispersed in 1 *wt.*% PSS solution. Uniform dispersion was achieved by subjecting the MWCNT-PSS mixture to 180 min of bath ultrasonication and 60 min of high-energy probe sonication (3 mm tip, 150 W, 22 kHz) [96]. The 1 mg/mL MWCNT-PSS solution was diluted with DI water to create ultra-low-concentration MWCNT-PSS solutions (*i.e.*, 1 μg/mL). The rationale for preparing 1 μg/mL MWCNT-PSS solutions was so that AFM imaging could resolve the physical properties of individual nanotubes as opposed to imaging a percolated network (which would then be difficult to characterize the properties of individual nanotubes).

The 1 μg/mL MWCNT-PSS dispersion was then used as is for preparing thin film samples for AFM imaging. Here, a silicon substrate was used. Prior to film deposition, silicon wafers were treated with piranha solution (H_2SO_4:H_2O_2 = 17:9) for 30 min to remove organic residues on the wafer surface and to enhance hydrophilicity. The cleaned silicon wafer was cleaved to obtain smaller chips (~7×7 mm^2) using a diamond scribe. A small drop of diluted MWCNT-PSS solution

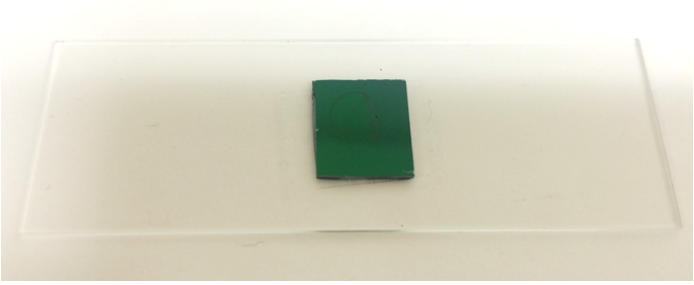

Figure 3.1. A small drop of 1 μg/ml MWCNT-PSS solution was pipetted onto a silicon substrate (~7×7 mm^2) and air-dried for AFM imaging.

was pipetted onto the substrate and left to air-dry in a fume hood for 12 h to form the final ultra-low-concentration thin film (Figure 3.1).

3.2.3 Image Analysis Procedure

As mentioned before, a primary focus of this work was not just to assume the physical parameters and dispersed shapes of CNTs when generating the numerical model but, instead, to integrate actual experimental measurements of nanotube properties (*i.e.*, dispersed shapes of CNTs and their lengths) with appropriate uncertainty quantification (*i.e.*, CNT length distribution). In this study, an Asylum MFP-3D AFM was employed to analyze the surface topography of MWCNT-PSS thin films deposited on silicon substrates. AFM was performed in tapping mode using a silicon cantilever (FMV-A, Bruker) with aluminum coating on the back and a spring constant of ~1.80 N/m. AFM imaging was initially conducted using a coarse scan size of 20 μm, and then the location of the target MWCNT was set as the next scan position to capture 5×5 μm^2 images.

Some representative AFM images are shown in Figure 3.2. Both amplitude (Figure 3.2a) and height images (Figures 3.2b–e) clearly showed that MWCNTs were embedded in the PSS matrix. As mentioned earlier, the specimen was assembled in a manner to deposit individual MWCNTs (*i.e.*, non-percolated) with very low concentrations of PSS. The drying process does not

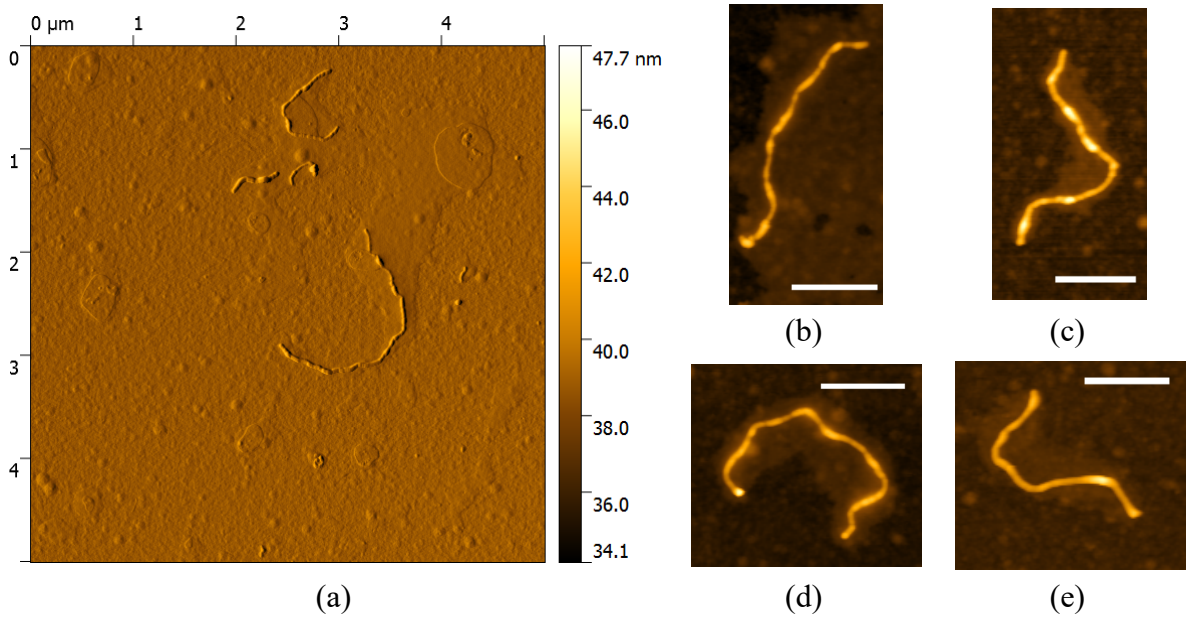

Figure 3.2. (a) The AFM amplitude image describes the surface topography of the MWCNT-PSS thin film. (b)-(e) AFM height images show various geometrical shapes of as-deposited MWCNTs. All scale bars represent 500 nm.

form a continuous thin film but rather localized regions with individual MWCNTs deposited on the silicon wafer. Since AFM imaging was performed on individual MWCNTs, the heights reported Figures 3.2b–e sufficiently characterized the physical properties of MWCNTs, as opposed to the PSS matrix. In addition, AFM imaging revealed the presence of ultra-short MWCNTs (*i.e.*, of a few nanometers). These MWCNTs were thought to be cut during high-energy tip sonication [147]; these were ignored during the characterization process, since they were unlikely to help form a percolated network even when high concentrations of nanotubes are used for thin film fabrication. One particular important finding here is that, unlike many CNT-based numerical models that assumed CNTs to be straight [121, 122, 149], the AFM images revealed a variety of shapes when they are deposited experimentally.

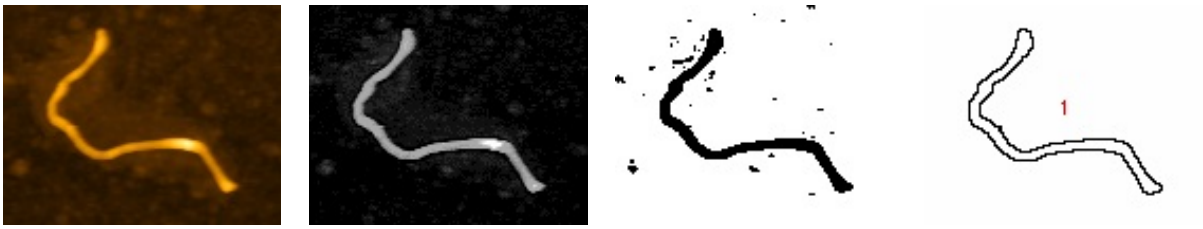

(a) (b) (c) (d)

Figure 3.3. The length of an MWCNT was estimated following four steps: (a) select the region of interest in the AFM image (RGB image); (b) convert the RGB image into a gray-scale image; (c) convert gray-scale image into a binary image; and (d) measure the perimeter or length of the MWCNT.

3.2.4 Image Analysis Results

MWCNT length measurements were obtained from AFM height images. The images were processed and analyzed using *ImageJ,* an image processing software. The image analysis procedure and intermediate steps are illustrated in Figure 3.3. First, an AFM image (RGB image) was imported to *ImageJ*. The correct scale of the image was defined using the scale bar in the AFM image. Then, a region of interest in which an MWCNT was located was selected (Figure 3.3a). Second, the RGB image was converted into a gray-scale image (8-bit). Then, the resulting gray-scale image shown in Figure 3.3b was enhanced by applying built-in commands (*i.e.*, sharpening, smoothing, median filter, and fast Fourier transform filter, among others) and converted into a binary black and white image (Figure 3.3c). Finally, the edges that sum to obtain each MWCNT's perimeter were identified and measured. Since the aspect ratio of each MWCNT is high, its length was estimated as half of the total perimeter (*i.e.*, the diameter of the MWCNT was assumed to be negligible).

To verify *ImageJ* length estimation, an MWCNT length was measured using a customized *MATLAB* program and then compared as follows. Similar to *ImageJ* analysis, an AFM image (RGB) was imported into *MATLAB* and converted into gray-scale. A target MWCNT was

Table 3.1. An MWCNT's length was measured using two methods and compared.

	Linear segment method (*MATLAB*)		Perimeter method (I*mageJ*)
	Number of segments	Estimated length (μm)	Estimated length (μm)
MWCNT 1	7	1.488	1.623
	14	1.590	
MWCNT 2	15	2.557	2.734
	20	2.581	

identified and divided into linear segments. The "measure distance" tool was used to measure the pixel distance of each linear segment in the image. Using the tool, the distance of the scale bar was measured for calibration. The measured segments were then added and converted to its physical length (in μm) using the ratio of the real distance of scale bar to pixel distance. The results are summarized in Table 3.1. It can be seen that the measured length using this linear segment method was comparable to that obtained from *ImageJ* (*i.e.*, herein referred to as the perimeter method). However, the length measured by the linear segment method was smaller than the perimeter method. One possible reason can be the fact that the perimeter method did not exclude the diameter of MWCNTs. In addition, results from linear segment estimation depend on the number of segments used for characterizing each MWCNT, where estimated length would increase with more linear segments used (*i.e.*, due to the fact that the MWCNT is curved). Overall, the perimeter method with *ImageJ* was successfully validated and was used for the remainder of this study.

In total, the lengths of 20 MWCNTs were measured, which yielded an average length of 1.904 μm and a standard deviation of 0.506 μm. Figure 3.4 shows the distribution of MWCNT lengths. In addition, a Gaussian distribution was fitted to the raw data, and one can find that fitting was adequate. It should be noted that the mean MWCNT length measured by image analysis was shorter than that reported by the manufacturer, which is 3 μm. A possible reason for this

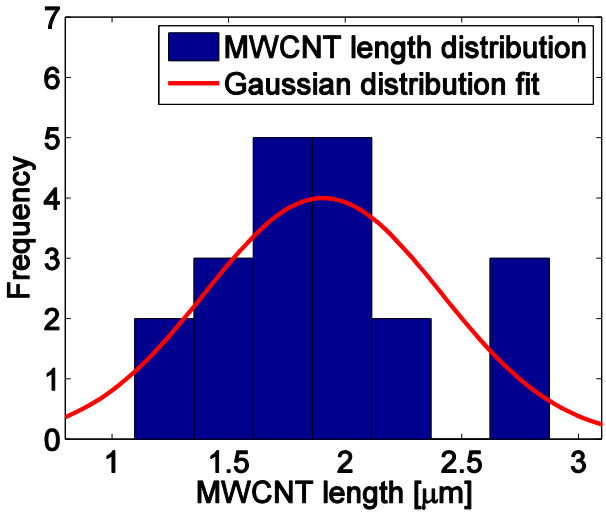

Figure 3.4. The histogram plots the distribution of different CNT lengths measured, and a Gaussian distribution was fitted to the raw data to obtain its average length of 1.904 μm and standard deviation of 0.506 μm.

discrepancy is that MWCNTs were cut and shortened during sonication, as was reported in other studies [147].

3.3 Numerical Modeling

3.3.1 CNT Thin Film Model

This work builds on the foundation established in a previous chapter, in which 2D percolation-based models were derived assuming that straight CNTs with a uniform length. Here, the uncertainties of as-deposited MWCNT lengths (*i.e.*, mean and standard deviation of MWCNT lengths) were incorporated when defining the numerical model. In addition, the model proposed herein also accounts for the different shapes of dispersed MWCNTs.

First, nanotube density (the number of CNTs or N) and the dimensions of the film (*i.e.*, length, L, and width, W) were defined. This work defined film size as 60×10 μm^2, and this geometry or aspect ratio was selected so as to be consistent with actual specimen aspect ratios that

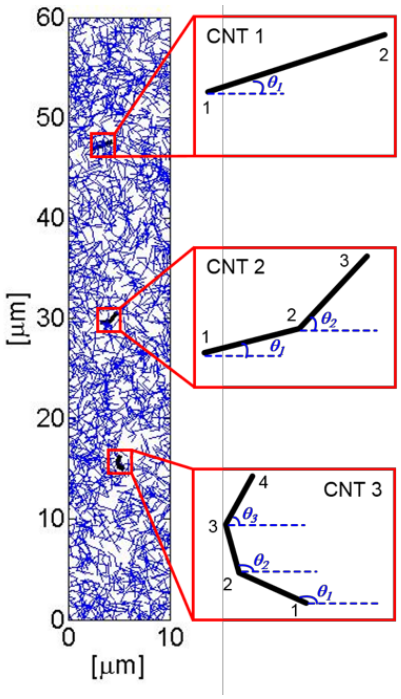

Figure 3.5. A representative 2D CNT-based thin film model (N = 1,400) was generated by randomly dispersing three types of CNTs (CNT 1, 2, and 3) within a 10×60 μm^2 area.

were experimentally tested [149]. Second, using the results from Section 3.2.4, the model assumed that CNT lengths (L_{CNT}) followed a Gaussian distribution identical to that obtained from image analysis, where the lengths of N CNTs were then generated using the "normrnd" function in *MATLAB*. Third, with each CNT length generated, CNTs of various shapes were randomly dispersed and deposited in the model space. Since AFM imaging of MWCNT-PSS thin films revealed that nanotubes can possess a wide variety of shapes, such as being nearly straight (Figure 3.2b), kinked (Figure 3.2c), and rounded (Figure 3.2d), this work assumed three predominant shapes during modeling, as is shown in Figure 3.5. The three different CNT shapes are: straight (CNT 1); two linear segments to form a kink with three nodes (CNT 2); and three linear segments with four nodes to form a rounded or a sinusoidal geometry (CNT 3). For simplicity, each linear segment was assumed to possess the same length. For example, CNT 2 and CNT 3 each had a segment length of $L_{CNT}/2$ and $L_{CNT}/3$, respectively. In addition, the angle at each node and between

adjacent segments were randomly generated to be between 0° and 179°; here, 179° was used as the upper-limit to prevent overlap of segments in the same CNT, and this was consistent with observations from AFM imaging.

To randomly locate CNTs in the 2D model space, the first end-point of a CNT, (x_1, y_1), was generated using *MATLAB*'s random number generator and positioned to be within the film dimensions. The positions of other nodes (i) were determined using the segment length and angles (θ_{i-1}):

$$x_i = x_{i-1} + \frac{L_{CNT}}{i-1}\cos(\theta_{i-1}) \tag{3.1}$$

$$y_i = y_{i-1} + \frac{L_{CNT}}{i-1}\sin(\theta_{i-1}) \tag{3.2}$$

where i is the nodal number (ranges from 1 to 4 depending on the type of CNT defined). Similar to the previous chapter, PBCs were implemented.

In total, five different models were generated to investigate how the morphology of the dispersed CNT-network affected bulk film electrical and strain sensing properties. The first model (Model #1), which was the control case, included only 1D straight CNTs (CNT 1). The second, or Model #2, consisted of only CNTs with two segments (CNT 2). Model #3 included only CNTs with three segments (CNT 3). Then, Model #4 and Model #5 were composed of different types of CNTs; Model #4 was composed of CNT 1 and CNT 2, while Model #5 consisted of all three different CNTs (CNT 1, 2, and 3). A representative Model #5 with N = 1,400 is shown in Figure 3.5.

3.3.2 Electrical and Electromechanical Properties

Upon generating the five different thin film models, their electrical and electromechanical properties were simulated and characterized. The electrical and electromechanical simulation

procedures followed the similar steps mentioned in Chapter 2. However, the difference between straight CNT-networks in Chapter 2 and Model #2 to #5 in this chapter was that the straight CNT-network had only one conducting component between two junctions (*i* and *j*) while other CNT-networks had more than one conducting component between two junctions. The intrinsic strain sensitivity for metallic nanotubes ($S_{CNT} = 60$) was incorporated in the model [141].

3.4 Results and Discussion

3.4.1 Nominal Electrical Properties

CNT thin film percolation-based models were formulated according to the steps discussed in Section 3.3, and the nominal or unstrained electrical resistance of five different models were calculated. However, before characterizing the nominal electrical properties of the CNT-network model, each model's percolation threshold was evaluated. The percolation thresholds for Models #1, #2, #3, #4, and #5 were identified as $N = 1{,}140$, 1,325, 1,440, 1,230, and 1,322, respectively.

The percolation threshold was used as the minimum number of nanotubes needed to obtain a percolated system so that electrical current could propagate through the film, so that the model's electrical resistance could be computed. Therefore, for this study, the mininum CNT density used was $N = 1{,}400$, and density was varied for $N = 1{,}400$, 1,800, and 2,400. CNT density was altered so as to model the incorporation of different carbon nanotube weight fractions or concentrations in the films. The results are summarized in Figure 3.6. Here, 20 simulations were conducted for each CNT concentration. Similar to Chapter 2, it can be observed that all five models showed a decrease in electrical resistance with higher CNT densities, which is consistent with percolation theory.

Although all models possessed identical CNT length distributions (*i.e.*, same average CNT length and standard deviation of CNT lengths), the different sets of models were constructed using

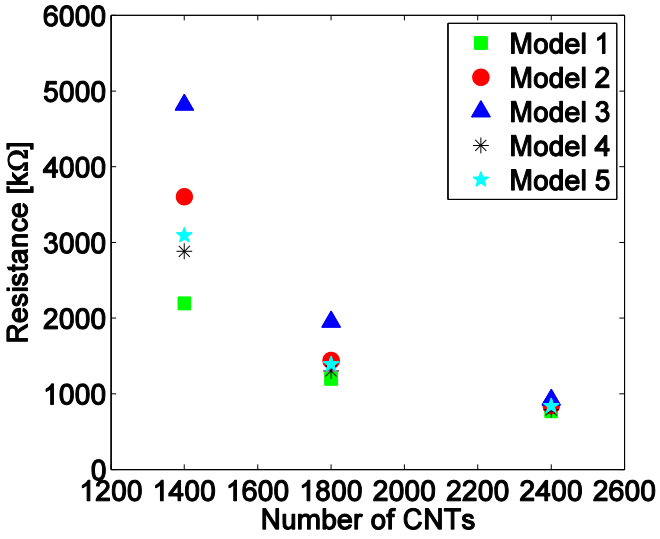

Figure 3.6. The average nominal (or unstrained) electrical resistances of five different CNT-based thin film models were simulated along with different CNT densities (N = 1,400, 1,800, and 2,400).

different CNT shapes, which caused the models to exhibit different nominal electrical resistances. In particular, the model that used CNTs represented by three linear segments (Model #3) exhibited the highest electrical resistance (lowest conductance), whereas the model with only straight CNTs (Model #1) had the lowest electrical resistance. This result directly supports the hypothesis that CNT geometry affects bulk film electrical properties. These results were consistent with other experimental and numerical investigations [119, 125, 150]. For example, as mentioned in Chapter 1, Yin *et al.* [125] utilized two different types of MWCNTs to fabricate two different epoxy-based nanocomposites. SEM images revealed that one type of MWCNTs dispersed in the epoxy matrix were significantly curved as compared to the other sample set. The result was that films consisting of 7 *wt.*% curved nanotubes yielded a bulk film conductivity of 0.00192 S/m, which is significantly lower than the other case (65.8 S/m) with mostly straight nanotubes (*i.e.*, the system with straight nanotubes yielded higher electrical conductivity or lower resistance, which is consistent with the findings presented in this work). Yi *et al.* [151] compared the percolation threshold of 2D fibrous networks with different geometries of conductive fibers (*i.e.*, rectangle, sinusoidal, and kinked

fibers). The author concluded that the curl ratio significantly affected percolation threshold (*i.e.*, percolation threshold increased with higher curl ratio), whereas percolation threshold was not affected by fiber geometries (*i.e.*, sinusoid, triangle, and rectangle) of identical curl ratio. Dalmas *et al.* [152] numerically showed that increasing the tortuosity of CNTs in a 3D fibrous network increased percolation threshold. Similarly, Berhan *et al.* [153] demonstrated that the effect of the shape of CNTs on percolation threshold increased when its aspect ratio was less than 1,000. Li *et al.* [119] generated 2D CNT-based nanocomposite models that considered two different CNT shapes (*i.e.*, straight and curved). It was shown that the model with curved CNTs exhibited lower conductivity versus the other with only straight CNTs. A curl ratio was defined as the ratio between the CNT length to effective CNT length (*i.e.*, maximum distance between two arbitrary points of a CNT). The results showed the model's electrical conductivity would decrease with higher CNT curl ratios, which is also consistent with the findings presented here.

In this study, a similar effective CNT length was defined [119]. In each thin film model, effective lengths of N CNTs were calculated and averaged. Then, the model's electrical resistance was plotted with respect to effective CNT length, as shown in Figure 3.7. For all N cases, Model #3 had a shorter effective length than the other four models, while Model #1 yielded the longest effective length. In addition, the results showed that effective length was not affected by CNT density. For example, the effective length of Model #3 was 1.484, 1.488, and 1.486 μm for N = 1,400, 1,800, and 2,400, respectively. On the other hand, when the number of CNTs was kept the same, the model with shorter effective lengths showed higher resistances. These results confirmed that bulk film electrical properties were sensitive to effective CNT lengths.

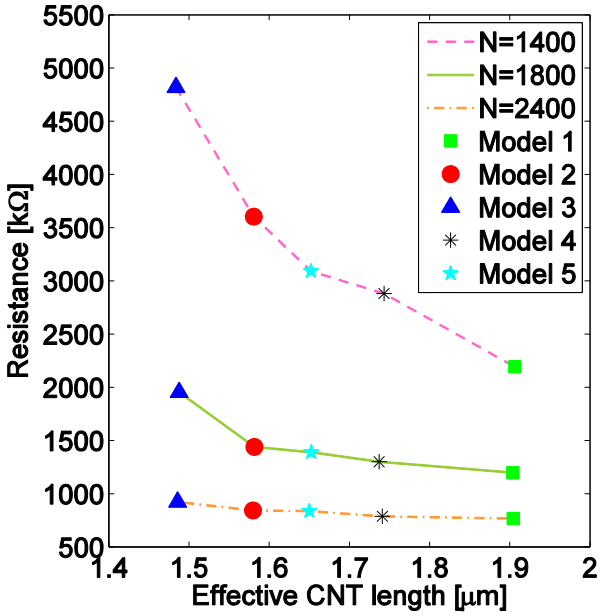

Figure 3.7. The unstrained resistances of different thin film models were plotted as a function of effective CNT lengths. Three different CNT densities (N = 1,400, 1,800, and 2,400) were considered.

3.4.2 Strain Sensing Properties

The electromechanical or strain sensing properties of the CNT-based thin film models were also investigated. Figure 3.8 plots the normalized change in resistance (R_{norm}) of five representative thin film models as a function of applied strains, when N = 1,400. First, all five models exhibited an increase in film resistance in tandem with increasingly applied strains. Second, it can be observed that R_{norm} of all five models exhibited a linear relationship with respect to applied strain. On the other hand, the values of R_{norm} at the same strain state varied depending on different thin film models. For instance, when applied strain was 0.01, the model based on only straight CNTs (Model #1) had a larger R_{norm} value (1.145×10^{-2}) than the other four cases (1.051×10^{-2}, 0.970×10^{-2}, 1.076×10^{-2}, and 1.048×10^{-2} for Models #2, #3, #4, and #5, respectively).

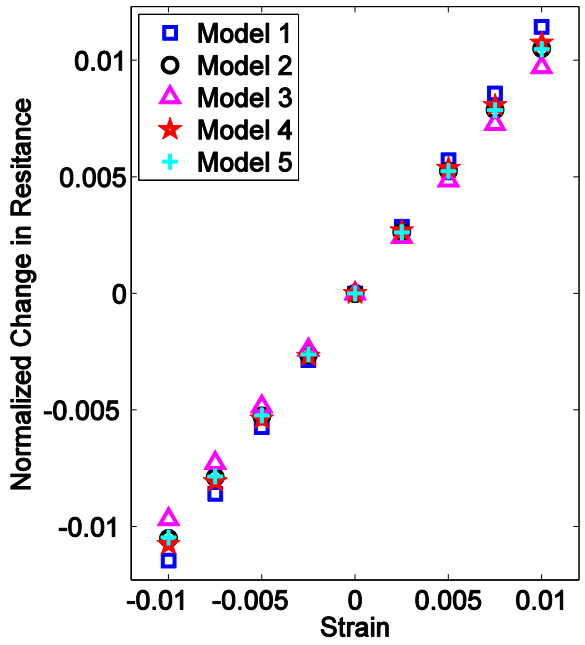

Figure 3.8. The normalized change in resistance was plotted as a function of applied strain. All five different types of CNT-based thin film models exhibited linear piezoresistivity.

Strain sensitivity or gage factor of the bulk film was obtained from the slope of the linear least-squares regression line fitted to each dataset shown in Figure 3.8. Similar to Section 3.4.1, CNT density was also varied (N = 1,400, 1,800, and 2,400), and the strain sensitivity results are summarized in Figure 3.9. Each data point corresponds to the average of 20 strain sensitivity simulations. A general trend was that, as the number of CNTs increased, strain sensitivity decreased, which was consistent with previous works and other experimental and numerical studies [98, 121]. In particular, it can be seen in Figure 3.9 that Model #1 with straight CNTs exhibited the highest strain sensitivities among the cases investigated. Model #2 and Model #5 showed similar strain sensitivities. For example, when N = 2,400, the average strain sensitivities of Model #2 and Model #5 were 0.923 and 0.925, respectively. On the other hand, strain sensitivities of Model #3 were the smallest of the five. These results suggest that a highly simplified CNT-based thin film model assuming that all CNTs are straight would tend to

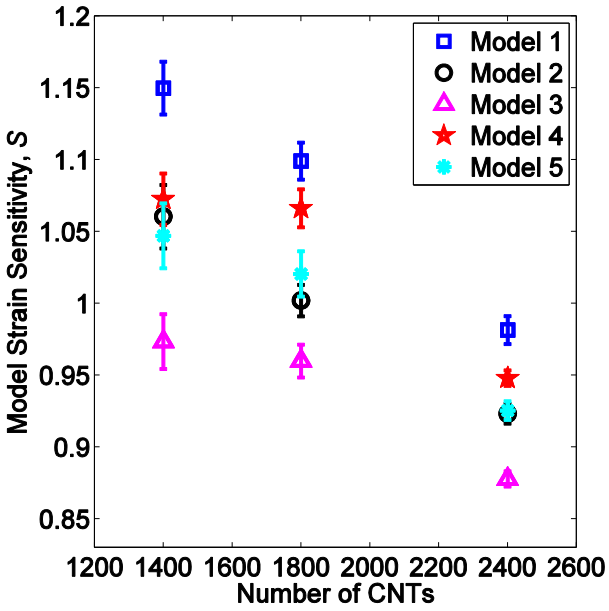

Figure 3.9. Strain sensitivities of 10×60 μm^2 CNT-based thin film models (with standard error of the mean plotted as error bars) were evaluated as a function of CNT density or *N*.

overestimate strain sensitivity (*i.e.*, within the framework of the assumptions presented in this numerical simulations study). Nevertheless, a more general conclusion is that the geometric shapes of CNTs is an important parameter that governs bulk film electrical and electromechanical properties and should be considered.

3.4.3 Experimental Validation

To validate the 2D CNT-based thin film model, MWCNT-PSS thin films were fabricated using a vacuum filtration method [91]. First, 0.75 mg/mL MWCNT-PSS solution was prepared following the procedures mentioned in section 3.2.2. The solution was then vacuum-filtered using a polytetrafluoroethylene (PTFE) membrane filter. Upon filtration and air-drying, the thin film was cut to form smaller (~4×33 mm^2) specimens. Then, two single-strand wires were affixed at opposite ends of the film, using silver paste, to form the electrodes. After drying the silver paste

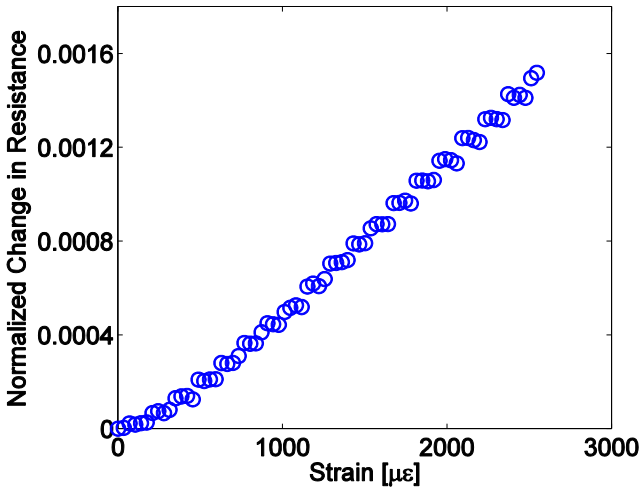

Figure 3.10. A 0.75 mg/mL MWCNT-PSS thin film was subjected to uniaxial tensile strains to 2,500 με.

for ~4 h in air, the nominal electrical resistance of the specimen was measured using a Keysight 34461A digital multimeter.

It should be mentioned that the films tested in these experiments were different than those used for AFM characterization. In these experiments, MWCNT-PSS thin films were electrically percolated (*i.e.*, conductive) and were characterized by an average nominal (unstrained) resistance of 42.98 Ω. The objective here was to study their bulk film electrical properties, as opposed to trying to identify individual nanotube physical properties. Then, the films were mounted in a Test Resources 150R load frame and subjected to monotonic uniaxial tensile tests. Tensile strains up to 2,500 με were applied at a load rate of 5,000 με/min. Figure 3.10 shows a representative result in which the normalized change in resistance of the thin film is plotted as a function of applied strains. It can be observed that, similar to the 2D numerical modeling results (Figure 3.8), the experiments revealed that MWCNT-PSS thin films also exhibited linear strain sensing properties.

3.5 Summary

In this chapter, 2D CNT-based thin film models were derived using AFM measurements of the physical properties of as-deposited MWCNTs. First, ultra-low-concentration MWCNT-PSS thin films were assembled by drying dispersed solutions on silicon substrates. Second, AFM images of these MWCNT-PSS thin films were obtained. The AFM images were processed to estimate the lengths of individual MWCNTs. It was found that the average length of 20 MWCNTs was 1.904 μm, which was shorter than their initial state (3 μm), suggesting that nanotubes were cut during dispersion. Moreover, the image analysis results demonstrated that dispersed MWCNTs, when deposited, could be characterized by complex geometric shapes, and three dominant shapes were identified for numerical modeling purposes.

The image analysis results were incorporated in 2D CNT-based nanocomposite models. First, all of the models were generated considering that CNTs could possess different lengths, and its statistical distribution followed those found in experiments (*i.e.*, from image analysis). To incorporate the three different CNT shapes in the model, these shapes were assumed to be composed of equidistant linear segments connected at the nodes, and the angle at each node was randomly generated. The model also randomly deposited CNTs in a 10×60 μm^2 representative area. Then, the simulations considered applying uniaxial tensile-compressive strains to the model so as to investigate how the bulk film properties would change in response to applied strains.

This work considered five different models to explore the effects of CNT morphology on bulk film electrical and electromechanical properties. It was found that the unstrained electrical resistance of models that incorporated more complex geometric shapes of CNTs were higher than a simplified case with only straight CNTs. In particular, given the same CNT density, electrical resistance was sensitive to effective CNT length. In addition, the morphology of the CNT network also affected the film's electromechanical behavior. The results showed that the CNT network with

straight CNTs was more sensitive to mechanical strains as compared to other thin film models. The thin film model that included CNTs with three linear segments exhibited the lowest strain sensitivity among the five different thin film models. Overall, these results suggest that the geometric shapes of CNTs can contribute significantly to affect bulk film electrical and electromechanical properties.

Chapter 3, in full, is a reprint of the material as it appears in Computational Mechanics, Bo Mi Lee; Kenneth J. Loh; Yuan-Sen Yang, 2017. The dissertation author was the primary researcher and author of this paper.

Chapter 4.

Experimental Validation of Carbon Nanotube Thin Film Sensor Model

4.1 Introduction

As mentioned in Chapter 1, the integration of experimental and numerical research on CNT-based thin film is limited despite the extensive experimental and numerical studies. The objective of this chapter was to derive an experimentally validated model of CNT-based thin film strain sensors. This study first began with the fabrication of MWCNT-Pluronic nanocomposites using a vacuum filtration method. Second, the films were subjected to uniaxial tensile strains while their electrical properties were measured, so as to characterize their strain sensing properties. Third, an experimentally validated, 2D, percolation-based, numerical model of the film was built with inputs obtained from SEM images of the fabricated films (*i.e.*, physical properties of CNTs as-deposited in the film). Then, the numerical models were subjected to the same tensile strain patterns, and the electromechanical properties of the model were compared with the experimental results. For further validation of the 2D CNT thin film model, a new concept of area ratio (*AR*)

was introduced, and *AR* of 2D CNT thin film models and that of MWCNT-Pluronic thin films using SEM images were computed and compared.

4.2 Experimental Methods

4.2.1 Materials

MWCNT (outer diameter: 10 nm, median length: 3 μm, and purity > 98%) and Pluronic® F-127 (Pluronic) ($M_W \approx 12{,}600$) were acquired from Sigma-Aldrich. Hydrophilic PTFE membrane filters (diameter: 47 mm and pore size: 0.45 μm) were purchased from EMD Millipore.

4.2.2 Nanocomposite Fabrication

MWCNT-Pluronic buckypaper specimens were fabricated using vacuum filtration (Figure 4.1) [91, 154]. An advantage of using vacuum filtration is that the density of film constituents (*i.e.*, nanotubes and polymers) can be precisely controlled. First, 1 *wt.*% Pluronic solution was prepared by dissolving Pluronic powder in DI water. Pluronic is a triblock copolymer with a central propylene oxide block and ethylene oxide chains, both of which are water soluble. Because of its amphiphilic characteristic, Pluronic can disperse nanotubes in aqueous solutions and achieving steric stabilization, which prevents agglomeration of nanotubes [155]. Shvartzman-Cohen *et al.* [156] demonstrated that SWCNTs can be dispersed in Pluronic solution well below the critical micellar concentration and critical micellar temperature. Zhao *et al.* [157] found that MWCNT-Pluronic dispersions remained stable for weeks. Thus, to attain homogeneous dissolution, the mixture was constantly stirred using a magnetic stirrer (Corning) at 55 °C for ~90 min. Second, upon stirring and when the Pluronic solution cooled to room temperature, dispersion of MWCNTs was achieved by subjecting MWCNT-Pluronic mixtures to 60 min of high-energy tip sonication (3 mm tip, 150 W, 22 kHz) [157]. In this study, seven different concentrations of MWCNT-

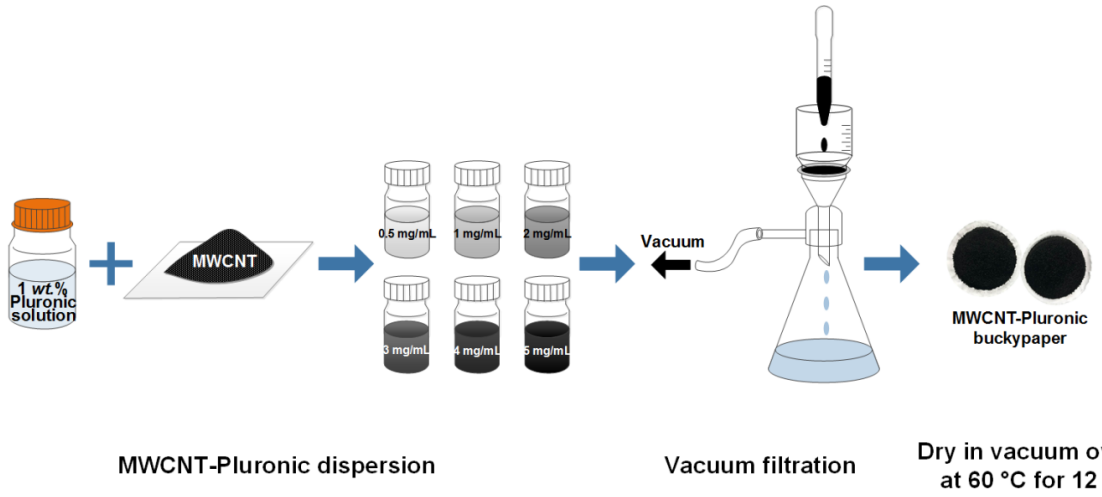

Figure 4.1. An MWCNT-Pluronic buckypaper was fabricated, first, by dispersing MWCNTs in 1 *wt.*% Pluronic solution. Then, the solution was vacuum filtered using PTFE membrane filter (pore size: 0.45 μm) and dried in a vacuum oven at 60 °C for 12 h.

Pluronic solution were prepared, namely 0.25, 0.5, 1, 2, 3, 4, and 5 mg/mL, to quantify the effects of MWCNT concentration on the strain sensing behavior of MWCNT-Pluronic nanocomposites. Next, the stable suspension was vacuum-filtered using a PTFE membrane. Finally, the film, together with the membrane filter, was dried for 12 h at 60 °C in a StableTemp vacuum oven. Figure 4.1 shows a picture of an MWCNT-Pluronic buckypaper specimen still attached to its PTFE filtration membrane.

4.2.3 Strain Sensing Characterization

The strain sensing properties of MWCNT-Pluronic buckypaper were characterized by applying uniaxial tensile cyclic strains to the films while simultaneously measuring their change in electrical properties. First, MWCNT-Pluronic buckypaper that was still attached to its PTFE membrane was cut to form smaller specimens of 4×30 mm^2. Second, two electrodes were established at opposite ends of the specimen using 1.5 mm-wide copper tape strips for two-point probe electrical measurements during load testing. Silver paste (Ted Pella) was applied over the

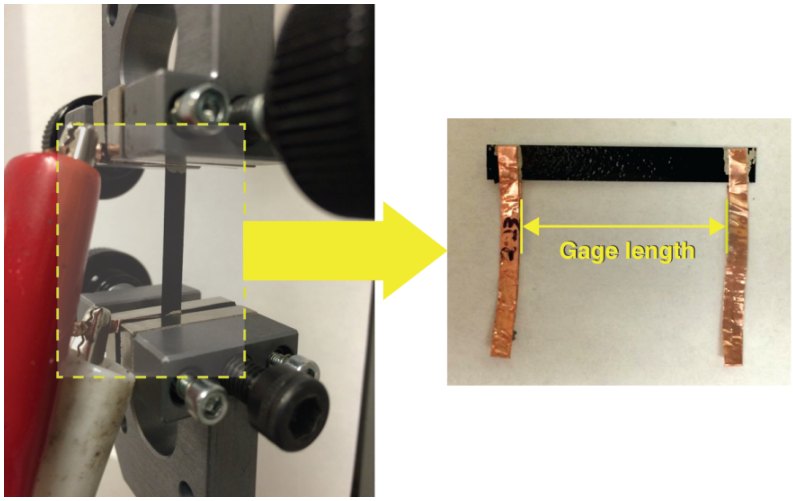

Figure 4.2. An MWCNT-Pluronic strain sensor was mounted in a Test Resources 150R load frame for strain sensing characterization.

copper tape electrodes and film for minimizing contact impedance and then dried in air for ~3 h. The distance between two electrodes (*i.e.*, gage length) was ~24 mm.

MWCNT-Pluronic buckypaper specimens were then subjected to electromechanical testing using a Test Resources 150R load frame with a 4.89 N (1.1. lbf) load cell installed (Figure 4.2). To ensure that the specimen is flat and taut, the load frame applied a preload to 0.2 N. Then, the load frame executed a five-cycle uniaxial tensile load pattern to strain the film to a maximum strain of 2,500 με (load rate: 5,000 με/min). Throughout the entire test, an Agilent 34401A digital multimeter recorded the electrical resistance of the film. The load frame's cross-head displacement, applied load, and the multimeter's electrical resistance measurements were simultaneously collected using a customized LabVIEW program. It should be mentioned that, since nanotubes are sensitive to environmental stimuli (*e.g.*, temperature [158], light [159], and humidity [160]), these tests were performed by shielding the entire test setup with a blackout curtain.

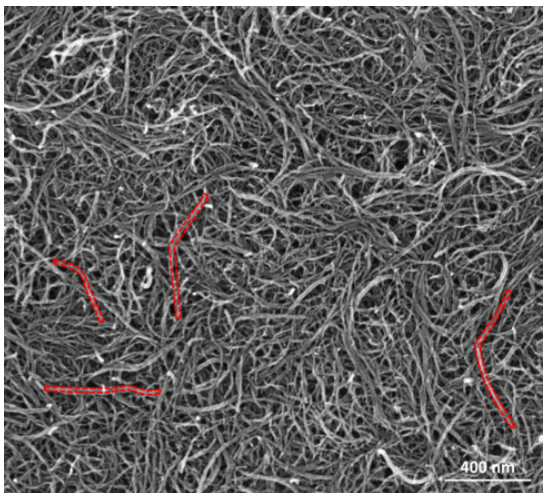

Figure 4.3. An SEM image of a 2 mg/mL MWCNT-Pluronic buckypaper shows the random, percolated morphology of MWCNTs.

4.3 Numerical Simulation Methods

4.3.1 Morphology Characterization and Model Generation

As an effort to understand and explain the experimental results of MWCNT-Pluronic strain sensor, a 2D CNT-based nanocomposite model was developed. In order to develop models that more accurately represented the actual shapes of CNTs in the thin film, SEM imaging was used to characterize the morphology of nanotubes in MWCNT-Pluronic buckypapers. Using an FEI 230 NanoSEM, one can obtain SEM images of the thin film, such as that shown in Figure 4.3, which clearly shows that MWCNTs were randomly oriented to form a densely percolated network. Although it is hard to locate the end-points of each nanotube, Figure 4.3 shows that MWCNTs were curved or slightly kinked. For instance, most nanotubes physically represent a half-cycle sinusoidal shape. Therefore, based on this observation, a 2D nanocomposite model can be generated. Here, the dimensions of the model were set as 4×24 μm^2 to have the same aspect ratio (*i.e.*, 1:6) as the MWCNT-Pluronic thin films in Section 4.2. It should be noted that the numerical model was developed specific to the type of film fabricated in this study, and changes to fabrication

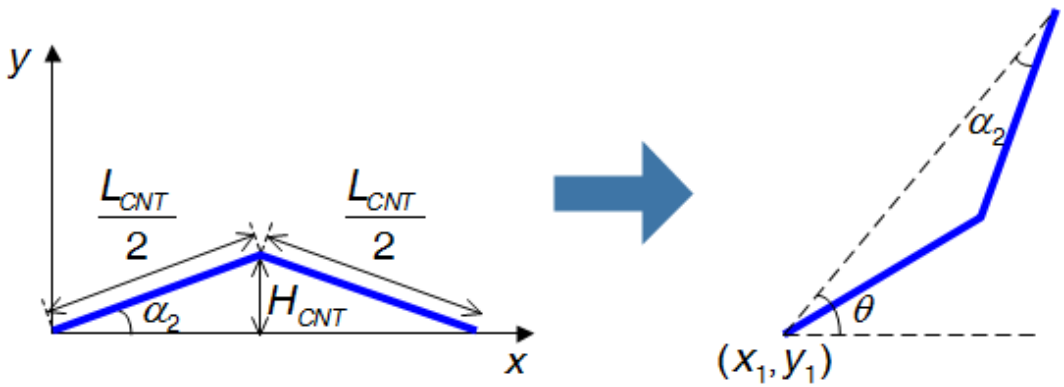

Figure 4.4. A kinked CNT can be described by the ratio of height-to-length of CNT (*i.e.*, height ratio (*HR*)).

procedure and the type of nanotubes used, among others, could change the results; nevertheless, the procedure for model generation employed in this study would still apply.

Before generating the CNTs in the model space, the physical properties of the as-deposited MWCNTs were needed. Similar to Chapter 3, a Gaussian distribution of CNT lengths with a mean and standard deviation of 1.904 μm and 0.506 μm was applied to the model. *N* number of MWCNTs (or equivalently related to density) were populated in the model space. The shape of MWCNTs were assumed to be kinked as a simplified representation of the half-cycle sinusoidal shapes observed in Figure 4.3. To decrease computational demand, the kinked shape comprised of two equidistant linear segments ($L_{CNT}/2$), where L_{CNT} is the total nanotube length. The position of the MWCNTs within the model space was also randomly determined, and one end of the MWCNT (at x_1, y_1) was defined by a distance (l_i) and orientation angle (α_i) with respect to the origin (0, 0) in a Cartesian coordinate system (Figure 4.4). To describe the degree of nanotube kink, a height ratio can also be defined as follows:

$$HR = \frac{H_{CNT}}{L_{CNT}} \tag{4.1}$$

where H_{CNT} is the distance from the vertex of the MWCNT relative to its local *x*-axis that intersects its two end-points (Figure 4.4). In this study, four different height ratios (*i.e.*, 0, 10, 20, and 30%)

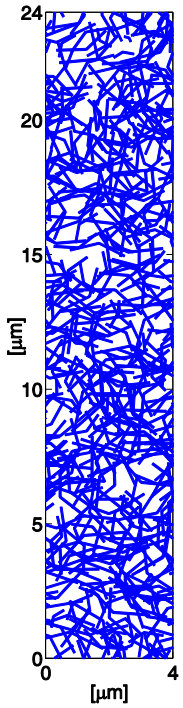

Figure 4.5. A representative nanocomposite model shows that kinked CNTs are randomly distributed in a 4×24 μm^2 area (N = 400 and HR = 20%).

were considered. Once each MWCNT was generated and its first end-point positioned at (x_1, y_1), the other two points (*i.e.*, vertex and end-point) were determined using α_i and a random rotation angle (θ):

$$\begin{aligned} x_i &= x_1 + l_i \cos(\theta - \alpha_i) \\ y_i &= y_1 + l_i \sin(\theta - \alpha_i) \end{aligned} \tag{4.2}$$

A representative numerical model with N = 400 and HR = 20% is shown in Figure 4.5 as an example.

4.3.2 Strain Sensing Simulation

The strain sensing behavior of the CNT-based nanocomposite model was simulated by calculating the electrical resistance of the model at different strain states. R_{jct} was assumed to be 240 kΩ specific to metal-metal junction resistance [161]. It should be mentioned that, in this work,

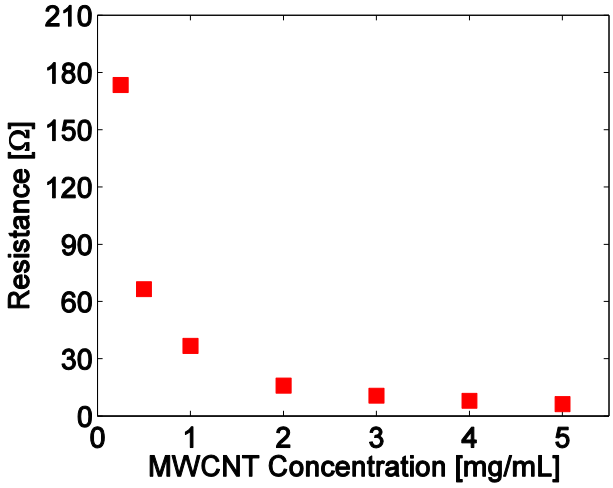

Figure 4.6. The unstrained electrical resistances of MWCNT-Pluronic strain sensors were plotted as a function of MWCNT concentration.

intrinsic strain sensitivity (S_{CNT}) of CNTs was also incorporated to the model and assumed to be 150 [162]. Finally, after calculating the models' electrical resistances corresponding to different strain states, their strain sensing properties were evaluated.

4.4 Experimental Results

4.4.1 Electrical and Strain Sensing Properties

The electrical properties and strain sensing behavior of MWCNT-Pluronic nanocomposites were characterized by following the procedures described in Section 4.2.3. The unstrained electrical resistance measurements are plotted in Figure 4.6. For each MWCNT concentration, 10 resistance measurements were obtained and then averaged. It can be seen from Figure 4.6 that the electrical resistance of the buckypaper decreased with increasing MWCNT concentrations. This result is expected, since higher densities of MWCNTs create denser networks of electrical conducting pathways, which result in higher bulk electrical conductance and lower electrical resistance. However, the rate of decrease in resistance with increasing MWCNT concentrations

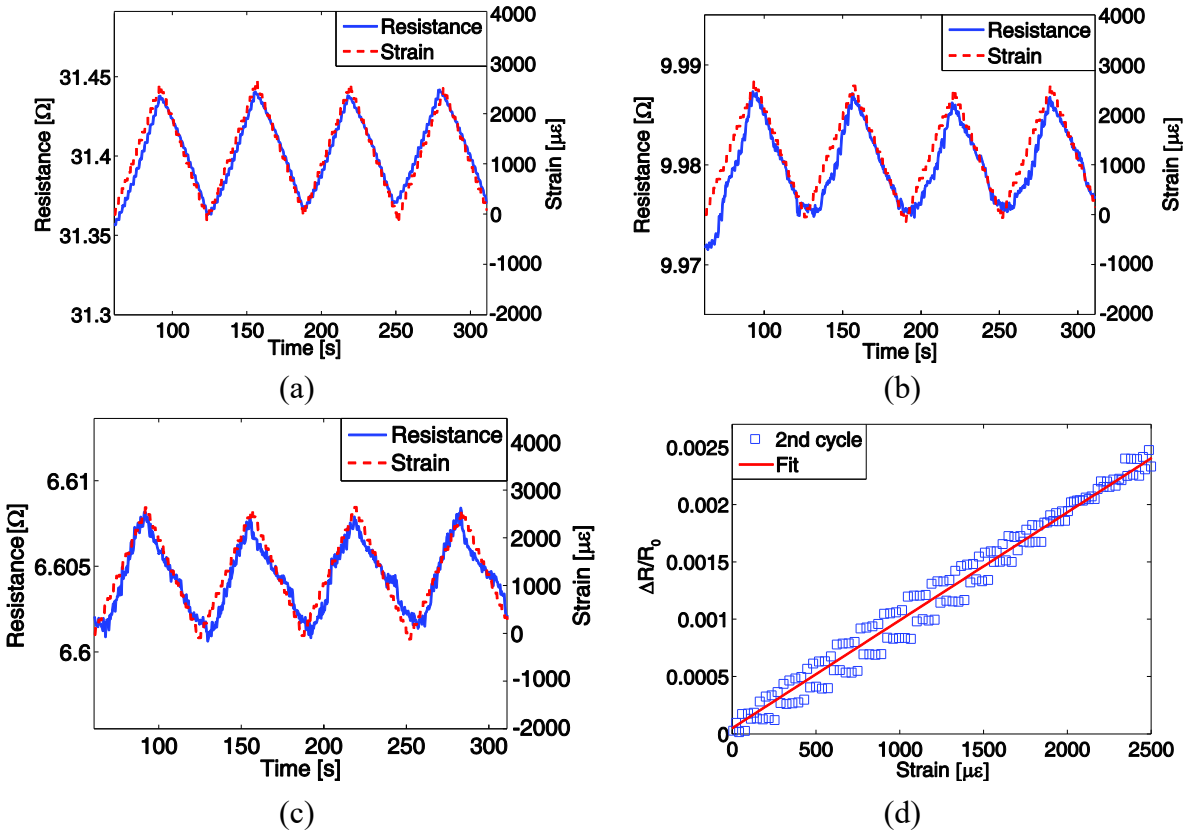

Figure 4.7. The electrical resistance responses of (a) 1 mg/mL, (b) 3 mg/mL, and (c) 5 mg/mL MWCNT-Pluronic strain sensors are overlaid with the corresponding applied strain time history. (d) The normalized change in resistance of a 1 mg/mL MWCNT-Pluronic strain sensor is plotted as a function of applied strains.

was nonlinear and slowed down. To be specific, when MWCNT concentration increased from 1 to 2 mg/mL, resistance decreased from 36.82 to 15.94 kΩ (*i.e.*, 56.7% decrease); from 4 to 5 mg/mL, resistance decreased from 8.03 to 6.28 kΩ (*i.e.*, 21.8% decrease).

In addition, the strain sensing properties of MWCNT-Pluronic nanocomposite were characterized. In a previous experimental study, the electrical resistance of MWCNT-latex thin films deposited on polyethylene terephthalate substrates exhibited linear piezoresistivity in response to applied tensile cyclic loading [149]. Similarly, when MWCNT-Pluronic strain sensors were subjected to five-cycle, uniaxial, tensile strains, their electrical resistance varied in tandem with applied strains. The results are summarized in Figure 4.7. In Figure 4.7a–c, the electrical

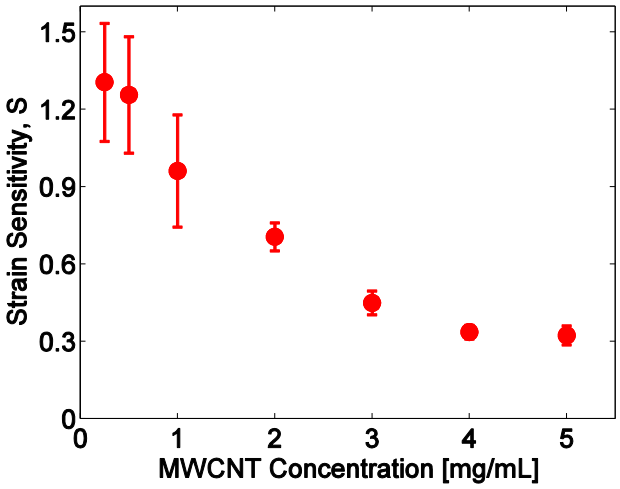

Figure 4.8. Strain sensitivities of MWCNT-Pluronic strain sensors and their error bars were obtained for buckypaper specimens fabricated using different MWCNT concentrations.

resistance time histories of three films with different MWCNT concentrations were overlaid with their corresponding applied cyclic load pattern. Here, only the responses from the second to fifth cycles are shown, and the first-cycle data was omitted; most specimens showed relatively higher increases in resistance during initial loading, which could be due to permanent deformation in the PTFE membrane. Regardless, the electrical properties of the films stabilized after the first cycle of applied loading.

Similar to numerical studies in Chapter 2 and 3, the strain sensing properties of MWCNT-Pluronic thin films was quantitatively studied using strain sensitivity estimated by fitting a linear least-squares regression line to the plot of R_{norm} versus $\Delta\varepsilon$, such as Figure 4.7d. In this study, S for each load cycle (*i.e.*, second to fifth cycles) was computed separately, and S for each film is reported as the average of the four cycles. For each MWCNT concentration, 10 different specimens were tested. Figure 4.8 summarize these results, and it can be seen that S decreased in an exponentially decaying fashion as the concentration of MWCNTs was increased from 0.25 to 5 mg/mL. This trend was consistent with other experimental and numerical studies [114, 124].

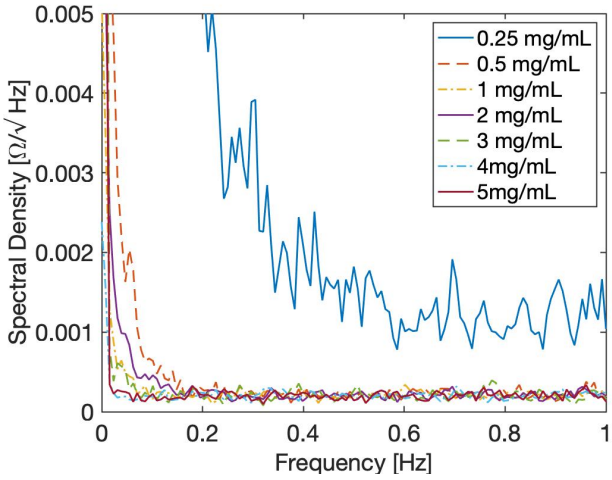

Figure 4.9. The amplitude spectral density was plotted as a function of frequency for seven difference concentrations of MWCNT-Pluronic thin films.

4.4.2 Strain Sensing Resolution

To further investigate strain sensing properties of MWCNT-Pluronic thin films, strain sensing resolution of MWCNT-Pluronic thin films was evaluated. Strain sensing resolution is defined as the smallest change of a strain sensor can reliably indicate. First, unstrained resistance of MWCNT-Pluronic thin films was measured for ~1,000 s with sampling rate of 2 Hz to obtain the noise floor of the sensor. A resistance change was then calculated by subtracting the mean of the unstrained resistance data from the unstrained resistance data:

$$\Delta R_i = R_i - R_{i,mean} \tag{4.3}$$

where ΔR_i is the change in unstrained resistance, R_i is the unstrained resistance, and $R_{i,mean}$ is the average of the unstrained resistance. An amplitude spectral density of the resistance change (ΔR_i) was then calculated and plotted as a function of frequency. Strain sensing resolution in resistance was estimated by averaging the amplitude values of spectral density after noise stabilization at f_s. Finally, the resolution in resistance was converted into strain to estimate the strain sensing resolution in strain using Equation 2.9.

Table 4.1. The strain sensing resolutions of MWCNT-Pluronic thin films were estimated and compared.

MWCNT concentration (mg/mL)	**0.25**	**0.5**	**1**	**2**	**3**	**4**	**5**
Resolution (μΩ)	1,183	221	212	205	206	204	202
Resolution (με)	4.30	3.04	7.40	17.61	44.84	73.79	88.91

In this chapter, seven samples of MWCNT-Pluronic thin films from each concentration were used. Figure 4.9 shows the results of the amplitude spectral density versus frequency. One can find that for higher MWCNT concentrations (1–5 mg/mL), the noise level stabilized at $f_s \sim 0.2$ Hz, while lower MWCNT concentrations (0.25 mg/mL and 0.5 mg/mL) plateaued at higher frequencies ($f_s > 0.4$). In particular, 0.25 mg/mL MWCNT-Pluronic thin films showed the higher noise level compared to other concentrations, which stabilized at $f_s \sim 0.6$ Hz. The strain sensing resolution results were summarized in Table 4.1. Except for 0.25 mg/mL, the resolution in resistance was similar regardless of MWCNT concentrations. However, due to the high strain sensitivity and unstrained resistance of the 0.25 mg/mL MWCNT-Pluronic thin film, the strain sensing resolution in strain was improved (4.30 με). The smallest strain sensing resolution that the MWCNT-Pluronic thin film achieved was 3.04 με at 0.5 mg/mL. The strain sensing resolution results indicated that although the 0.25 mg/mL MWCNT-Pluronic thin film was the most sensitive to applied strains among seven MWCNT concentrations, the highest resolution was achieved by the 0.5 mg/mL MWCNT-Pluronic thin film. Therefore, depending on the purpose of CNT-based strain sensors, the CNT concentration should be judiciously determined.

In general, the best sensor configuration requires a higher sensitivity with lower resolution. It was shown that the MWCNT concentration of the highest strain sensitivity (*i.e.*, 0.25 mg/mL)

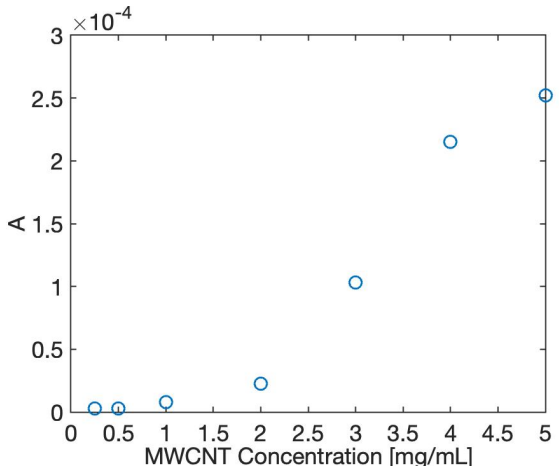

Figure 4.10. The strain sensing resolution in strain was divided by the strain sensitivity and plotted as a function of MWCNT concentrations.

and that of the lowest strain sensing resolution (*i.e.*, 0.5 mg/mL) were different. Therefore, to find the best solution (*i.e.*, MWCNT concentration), A was defined as below:

$$A = \frac{\gamma_\varepsilon}{S} \tag{4.4}$$

where γ_ε is the strain sensing resolution in strain, and S is the strain sensitivity of an MWCNT-Pluronic thin film. The MWCNT concentration with a minimum A is the concentration in which the strain sensing performance is optimized. The results are summarized in Figure 4.10. The 0.5 mg/mL MWCNT-Pluronic thin film showed the lowest A (2.72×10^{-6}). A value of the 0.25 mg/mL MWCNT-Pluronic thin film was comparable to that of 0.5 mg/mL (2.77×10^{-6}), and A increased at higher MWCNT concentrations (*i.e.*, 1–5 mg/mL). The results suggest that 0.5 mg/mL is the optimum MWCNT concentration with the best strain sensing configurations of the strain sensitivity and the strain sensing resolution among seven different concentrations.

4.5 Numerical Simulation Results

By following the procedures outlined in Section 4.3, nanocomposite strain sensing properties of different models were simulated. Before conducting strain sensing simulations, the

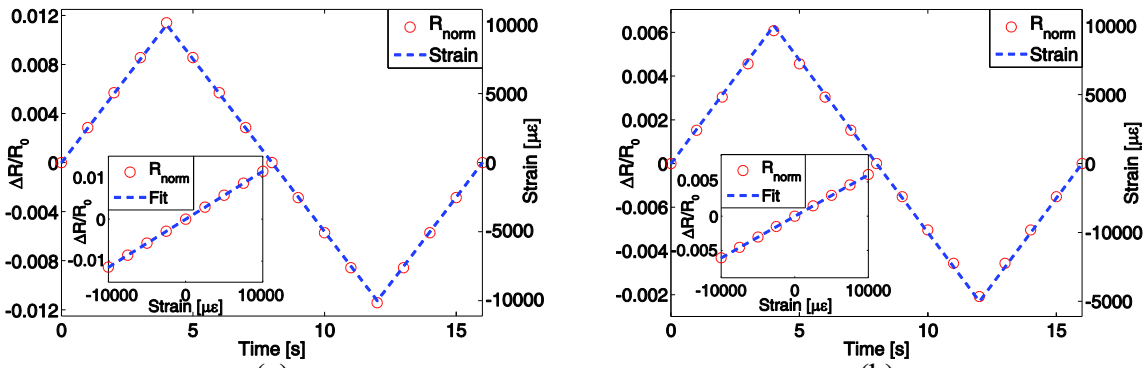

Figure 4.11. CNT-based nanocomposite models with (a) N = 300 and (b) N = 800 (HR = 20%) were subjected to a one-cycle tensile-compressive strain pattern to ±10,000 με, and their respective strain sensitivities were S = 1.14 and 0.61.

percolation probability [115] of each model was calculated for N = 250. The percolation probability for HR = 0, 10, 20, and 30% were 60.4, 55.4, 51.4, and 29.4%, respectively. Figure 4.11 shows the representative set of results corresponding to models of N = 300 and 800 (HR = 20%). The normalized change in resistance varied linearly in response to applied strains. The strain sensitivities of N = 300 and 800 were 1.14 and 0.61, respectively. Strain sensitivities were evaluated for models of different CNT densities (N).

In addition, this study investigated the effects of variations in HR and CNT statistical length distributions on bulk film strain sensing properties. The results are summarized in Figures 4.12 and 4.13. Each data point corresponds to the average strain sensitivity calculated from 20 simulations (for each case). Both sets of results showed that strain sensitivity decreased as N increased. In particular, it can be seen from Figure 4.12 that models with higher height ratios exhibited lower strain sensitivities as compared to those with lower HR. To be specific, when N = 250, the strain sensitivity for the HR = 30% case was 1.03, while that of HR = 0% (*i.e.*, CNTs were assumed to be straight elements) was 1.29. Figure 4.13 demonstrated that models that considered a Gaussian distribution of CNT lengths showed similar strain sensitivities than cases considering a fixed CNT length (*i.e.*, L_{CNT} = 1.904 μm), except at lower CNT densities and when the models

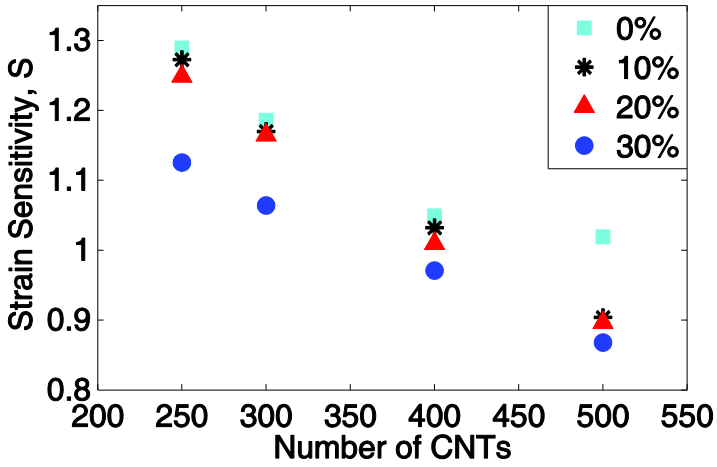

Figure 4.12. Strain sensitivities of nanocomposite models with different CNT densities (*N*) and shapes (*HR* = 0, 10, 20, and 30%) were computed.

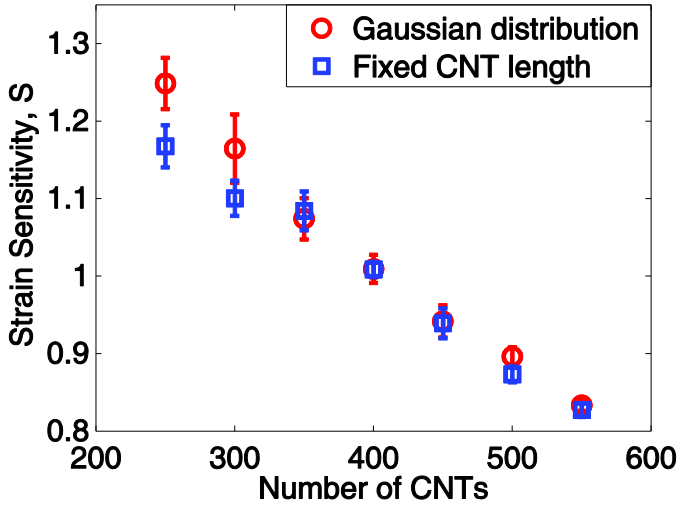

Figure 4.13. The strain sensitivities of nanocomposite models assembled using CNTs assumed to be of a fixed and a distribution of lengths were computed and compared.

were close to their percolation threshold (*i.e.*, *N* = 250 and 300). These numerical simulation results suggested that the geometrical features of dispersed CNTs and length distributions need to be considered for modeling nanocomposites, especially at lower CNT densities, since these effects influence the bulk film electromechanical properties.

4.6 Comparison of Experimental and Numerical Results

4.6.1 Strain Sensing Properties

From the results presented in Sections 4.4 and 4.5, both the MWCNT-Pluronic strain sensor test results and numerical models confirmed their linear piezoresistivity. Moreover, the model with *HR* = 20% showed similar strain sensing characteristics with the MWCNT-Pluronic test results. The normalized change in resistance of experimental tests results and numerical models with *HR* = 20% are plotted together with respect to applied tensile strains as shown in Figure 4.14. Only the tensile test results are compared in Figure 4.14, since it was not possible to apply compressive strains to the actual films as it would buckle the specimens. In Figure 4.14, the numerical simulation results are presented as linear lines, whereas the experimental data points are plotted individually. Overall, Figure 4.14 shows good matching between experimental and numerical results. It can also be observed that, as the density of MWCNTs increased, the slope of the lines and strain sensitivity decreased.

In Figure 4.15, strain sensitivities of the models and MWCNT-Pluronic strain sensors are overlaid according to CNT density and MWCNT concentration in the film, respectively. Most of the strain sensitivity data from the models were generated from averages of 20 simulations, but due to computational demand and time, only 10 simulations were conducted for the N = 800 and 900 cases and five simulations for the 1,000 to 1,500 models. In addition to the average strain sensitivity, the error bars show the standard deviations for each CNT density case. In general, one can clearly see that the simulation results agreed with those obtained from strain sensing characterization tests conducted on actual MWCNT-Pluronic buckypaper specimens. For example, the strain sensitivity of 0.5 mg/mL MWCNT-Pluronic films (*i.e.*, S = 1.26) was approximately equal to the nanocomposite model with N = 250 (S = 1.25). These results suggest

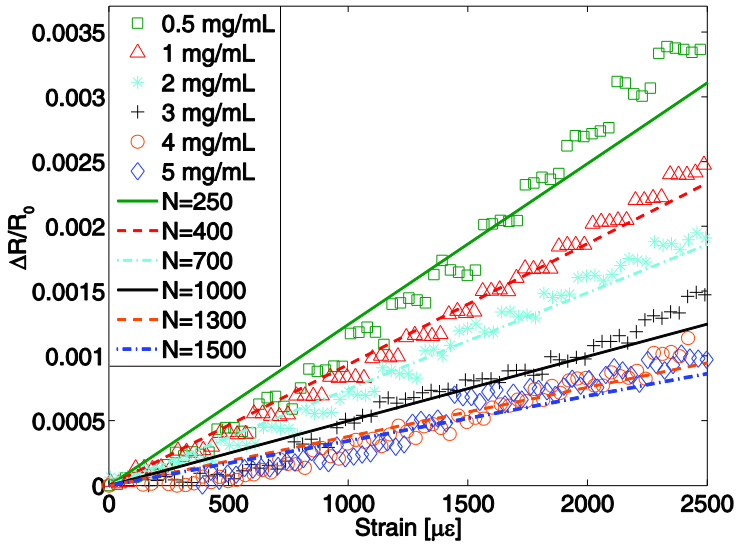

Figure 4.14. The experimental and numerical model strain sensing responses are compared by plotting the normalized change in resistance as a function of applied strains.

that the model proposed can be used to describe the strain sensing properties of MWCNT-Pluronic thin films.

4.6.2 Area Ratio (AR)

Besides observing similarities between experiments and simulations, further validation of the 2D nanocomposite model can be performed by computing the *AR* of MWCNT-Pluronic buckypapers using SEM images. *AR* is defined as the ratio of MWCNT network area to the total area of the image and can be calculated using equation:

$$AR = \frac{A_{CNTs}}{A_{total}} = \frac{N_1}{N_{pixel}} \tag{4.4}$$

where A_{CNTs} is the area occupied by MWCNTs, A_{total} is the total area of the image, N_1 is the number of pixels occupied by 1, and N_{pixel} is the number of pixels of the entire image. Essentially, AR computes the effective percentage of the 2D space that is occupied by the conductive MWCNTs. The area ratio is a simple and effective means for validation, because, ideally, *AR* for the numerical

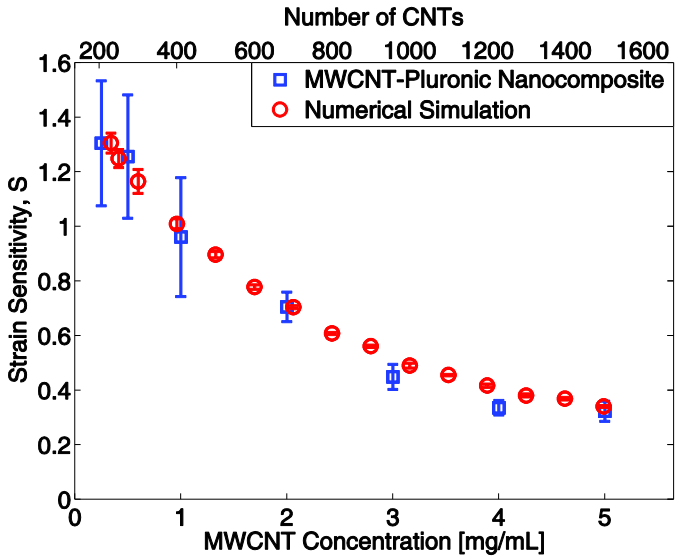

Figure 4.15. The strain sensitivities obtained from experimental tests and numerical simulations are compared for films with different CNT concentrations/densities.

models should be comparable to those observed in experiments and in the actual films. However, it should be mentioned that there are limitations to this method. MWCNTs form a dense 3D percolated network in the films, and nanotubes do not only lie in a single plane. By virtue of using SEM images for computing *AR*, one is only considering a planar view of the complex network. However, the model presented in this study is an effective simplified numerical model that was derived from 2D AFM and SEM images of individual nanotubes. In that regard, the initial inputs to the numerical model (*e.g.*, statistical length distributions of nanotubes) already considers the non-planar orientation of MWCNTs.

The first step is to compute *AR* of actual MWCNT-Pluronic thin films. First, SEM images of MWCNT-Pluronic buckypapers were obtained (Figure 4.16a) using a Zeiss SIGMA 500 with an accelerating voltage of 3 kV. Since the interest of this study was the surface topography of MWCNT-Pluronic buckypapers, a secondary electron detector was used. Second, the SEM image in RGB format was imported to *MATLAB* and converted to gray-scale, using built-in functions available from *MATLAB*'s image processing toolbox. A histogram of the image was used to

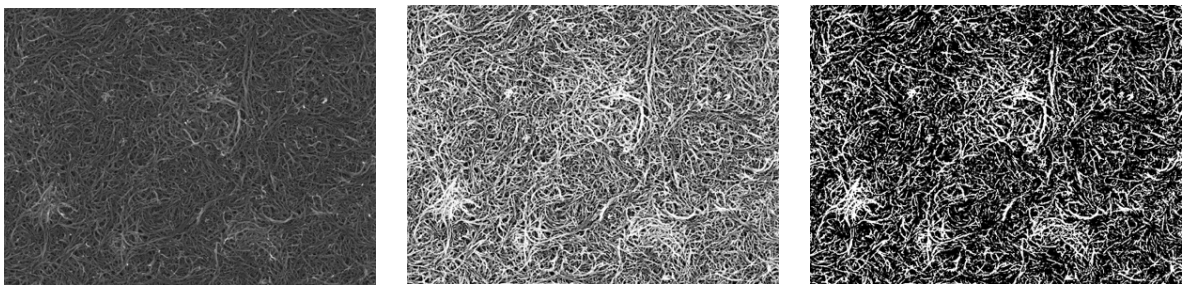

(a) (b) (c)

Figure 4.16. The area ratio of MWCNT-Pluronic nanocomposites was determined by following three steps: (a) acquire SEM image; (b) enhance image; and (c) convert enhanced image into a binary image.

observe the image pixel intensity distribution. Since the histogram of gray-scale SEM images tended to show that intensity of the image was biased toward the dark end, image contrast was enhanced using the histogram equalization method (Figure 4.16b). Third, to define the edge of MWCNTs, the enhanced images in gray-scale were converted into binary black-and-white images (Figure 4.16c) by determining pixel intensity ranges (*i.e.*, region of interest). It should be noted that, in the gray-scale image, a translucent interface was observed near the edges of MWCNTs, which was considered as polymer (*i.e.*, Pluronic) covering the MWCNTs [163]. In the binary image such as Figure 4.16c, the white area (*i.e.*, 1 in binary representation) was considered as MWCNTs, whereas black was regarded as the polymer matrix or vacant region.

SEM images of four different MWCNT concentrations (2, 3, 4, and 5 mg/mL) are shown in Figure 4.17. SEM images of lower MWCNT concentrations (0.25 to 1 mg/mL) were excluded, since MWCNT boundaries were less clear, and the images were also affected by charging effect. In this work, a conductive coating was not used to preserve the pristine nanocomposite surface. It can be seen in Figure 4.17 that, as MWCNT concentration increased, more MWCNTs were distributed and less voids are present. Furthermore, the film's surface topography became more nonuniform. For example, by comparing 2 and 3 mg/mL SEM images (Figure 4.17a–b) to 4 and 5

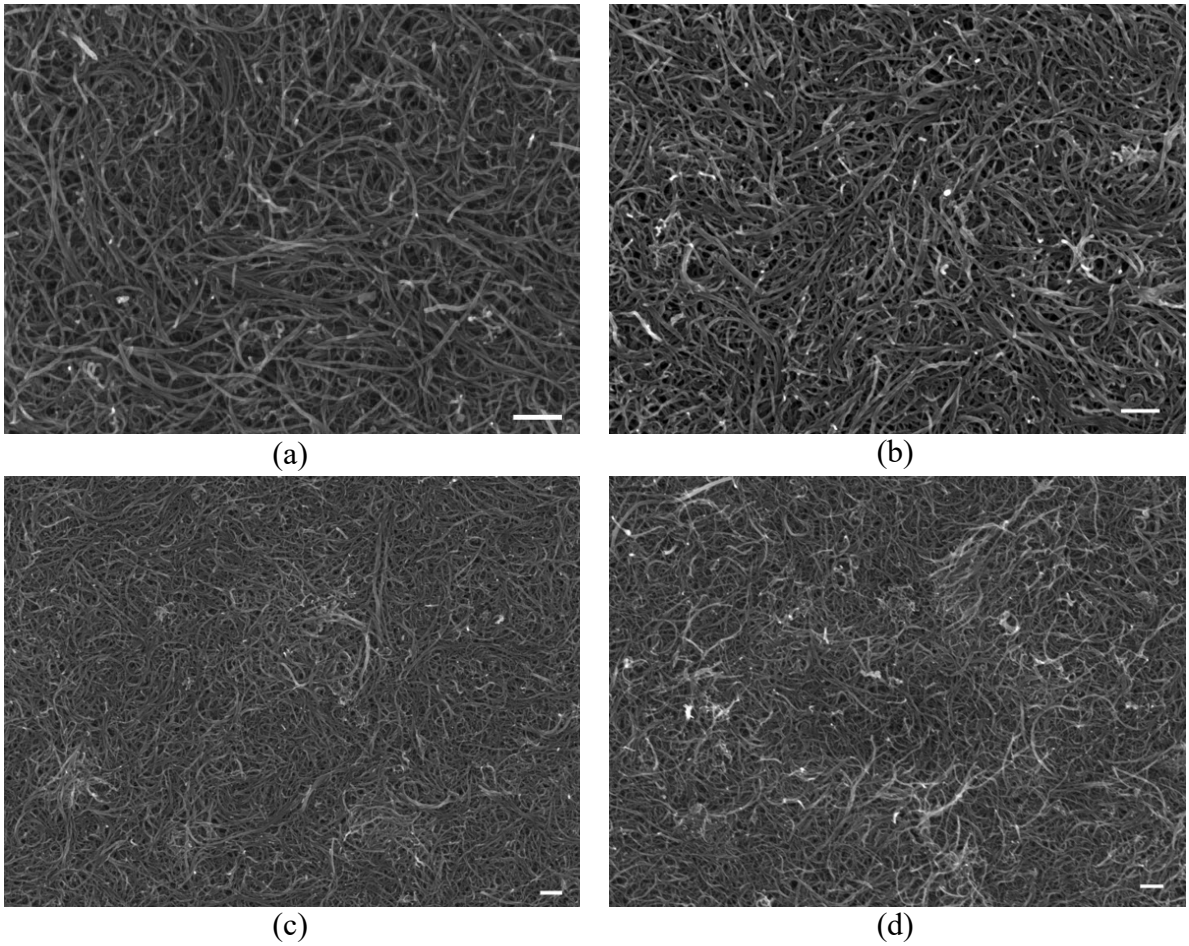

Figure 4.17. SEM images of MWCNT-Pluronic thin films with (a) 2, (b) 3, (c) 4, and (d) 5 mg/mL concentrations are shown. The white scale bar represents 200 nm.

mg/mL ones (Figure 4.17c–d), it can be seen that there are regions with clusters of dispersed MWCNTs situated higher than other regions of the film. This, however, was not an issue and was considered during image analysis by adjusting pixel intensity ranges when the grayscale images were converted to binary images.

Similarly, the *AR* of the nanocomposite numerical model was also evaluated. Although the diameter of CNTs was not specified in the model during simulations, one can still consider CNT diameter during image analysis. An SEM image of MWCNT-Pluronic nanocomposite was used to define the average diameter for as-deposited MWCNTs. Diameter was determined by measuring the two edge boundaries of an MWCNT in the SEM image. Most diameter measurements ranged

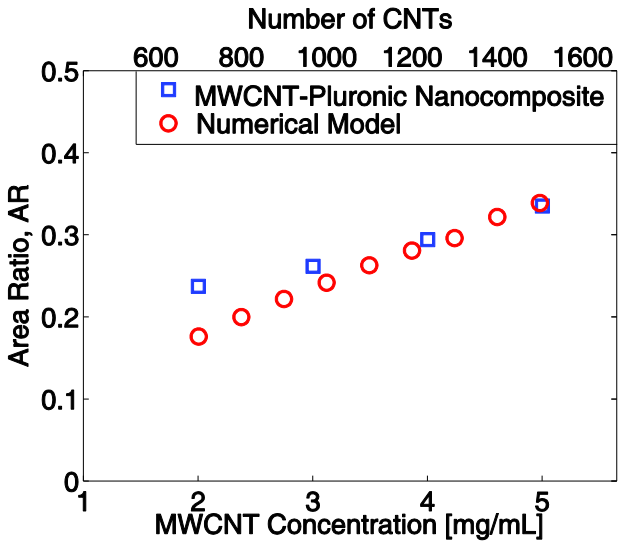

Figure 4.18. The area ratios of MWCNT-Pluronic nanocomposites and numerical models were evaluated and compared.

from 15 to 25 nm, so an average diameter of 20 nm was assumed and applied to the model. Then, the RGB image of the numerical model was saved (after model generation) and processed in the same manner as the aforementioned experimental case; the only difference was that image enhancement was not required.

Since it was demonstrated in Figure 4.15 that the strain sensitivity of 2 mg/mL MWCNT-Pluronic strain sensor ($S = 0.71$) was similar to that of the $N = 700$ model ($S = 0.70$), area ratios of numerical models with $N \geq 700$ were calculated and compared, following the aforementioned procedures. In Figure 4.18, area ratio results of MWCNT-Pluronic strain sensor experimental tests and numerical models were summarized. Similar to the strain sensitivity results, area ratios of MWCNT-Pluronic buckypapers were comparable to those computed for the numerical models. For example, AR for 3 mg/mL buckypaper was 0.262 and was similar to that of the corresponding $N = 1{,}000$ model ($AR = 0.242$). It should be noted that the size of the model space is irrelevant, since AR is always normalized with respect to the dimensions. Despite the favorable area ratio results, AR for the model was slightly lower than those computed from experimental SEM images.

A possible reason could be due to the inherent nature of imaging, where the SEM image attempts to capture everything in its 3D view but flattened to form a 2D image. Therefore, nanotubes near the surface appeared to be brighter and larger compared to nanotubes located subsurface. During image analysis, the brighter area with high intensity was regarded as MWCNTs, the polymer close to the surface could appear with the same shade of gray as compared to nanotubes in a lower plane [164]. In addition, another source of error could be the assumption of a constant CNT diameter for the numerical models.

4.7 Summary

In summary, this chapter characterized the strain sensing properties of MWCNT-Pluronic thin films and compared experimental and numerical modeling results. First, MWCNT-Pluronic buckypaper specimens were fabricated by vacuum filtration, and seven different MWCNT concentration sample sets were prepared. The films' unstrained electrical properties were measured, and they were also subjected to electromechanical tests. Second, a 2D CNT thin film model was derived, taking into account the kinked shape CNTs and statistical length distributions observed from SEM images of MWCNT-Pluronic buckypapers. The model's nominal electrical properties, as well as at different applied strain states, were computed by constructing a conductance matrix of the CNT network. Lastly, the experimental and numerical simulation results were compared. Both the model and the experimental results revealed the linear piezoresistive properties of the nanocomposites. Furthermore, both results showed that strain sensitivity decreased as CNT density was increased. Not only were these trends the same, the values for strain sensitivities were also similar, thereby suggesting that the models accurately described the electromechanical properties of the films. To further validate the nanocomposite model, an area ratio calculation was defined. Image processing was employed to compute the area ratio of

MWCNT-Pluronic buckypapers (using SEM images), as well as for the numerical models. The area ratios between experiments and the models were comparable, thereby successfully validating that the models' physical and electromechanical properties represented that of the actual buckypapers fabricated.

Chapter 4, in full, is a reprint of the material as it appears in Nanotechnology, Bo Mi Lee; Kenneth J. Loh, 2017. The dissertation author was the primary researcher and author of this paper.

Chapter 5.

Model-enabled Design of Distributed Strain Sensor using Carbon Nanotube Nanocomposites

5.1 Introduction

The main objective of this chapter was to leverage the experimentally validated CNT-based thin film model to design and implement CNT-based thin film sensors for structural health monitoring (SHM). A distributed strain sensing system using CNT-based thin films and the principles of ETDR was developed and validated. Strain sensing was enabled by replacing portions of the transmission line with piezoresistive CNT-based sensing elements. In particular, MWCNTs were used to modify the conductor and dielectric portions of the sensing element. Before assembling MWCNT-based ETDR sensors, different designs of CNT thin film models were simulated. Special attention was paid to understand how the orientations of CNTs in the polymer matrix affected their piezoresistive response. The results of numerical simulations were used to guide the design of the distributed stain sensor. The hypothesis was that a resistive part of the

proposed distributed sensor and their piezoresistivity governed its strain sensing behavior. Based on numerical simulation results, four unique sample sets of MWCNT-based distributed sensors were assembled. The ETDR sensing properties of the sample sets were characterized and compared systematically. Simultaneously, strain sensing along different points in a transmission line was also validated.

This chapter begins with reviewing current sensing technologies for SHM including metal-foil strain gage, radiography, ultrasonics, and fiber-optic sensing following a brief background of ETDR. Then, CNT-based thin film models with different CNT orientations were derived, and their electrical and piezoresistive behavior were simulated. This is followed by describing how the MWCNT-based sensing elements were fabricated, as well as the different strain sensing test protocols employed in this study. Next, the ETDR strain sensing results of the different sample sets, as well as sensing strain at multiple points in a single transmission line, were discussed. The chapter concludes with a brief summary of the main findings and contributions of this research.

5.2 Sensing Technologies for SHM

The performance of aerospace, civil, marine, and mechanical structural systems can degrade due to damage and deterioration, particularly because of fatigue, impact, excessive loading, and harsh environmental conditions. If damage remains undetected, it can accumulate and propagate to cause component or even system failure. Therefore, SHM aims to monitor target structures over time (either periodically or continuously), detect anomalies, and extract damage-sensitive features from measurements [165]. To date, the most widely used means of monitoring damage is by visual inspection, but it is time-consuming, expensive, and challenging, especially when structures are large, have complex geometries, and damage can occur at different locations.

To address the limitations of visual inspection while enhancing the capability to monitor the integrity of structure, SHM systems have been sought to take novel sensing technologies to extract damage-sensitive features, and analyze the features for damage detection and structural prognostics [166]. Since SHM system monitors the structural condition and informs the operator if the damage is detected, maintenance approach can be condition-based instead of time-based significantly reducing the economic burden [166]. Current state-of-the-art sensing technologies of metal-foil strain gage, radiography, ultrasonics, and fiber-optic sensing will be briefly reviewed.

5.2.1 Metal-foil Strain Gage

Among the various parameters of interest (*i.e.*, displacement, crack opening, temperature, and humidity), knowledge of stress and strain is critical, since the failure criterion is often defined according to the material's yield point or ultimate strength. Without a practical method to directly measure stress, stress can be estimated from strain along with *a priori* information about material properties and behavior. Conventional means of measuring strain is by using metal-foil strain gages. It consists of a metal foil pattern located on an insulating film. When an object with a strain gage attached is subjected to deformation, the resistance of the metal foil changes under deformations, showing piezoresistivity. Although they are low-cost and fairly accurate, their main limitation is that they are discrete transducers that can only acquire strain at their instrumented location. For practical applications, a dense array of strain gages is required, but a number of cables that connect gages to the data acquisition system can make implementation challenging and expensive [167-169].

5.2.2 Radiography

Radiography uses high energy electromagnetic radiations (*i.e.*, X-rays, gamma-rays, or neutron rays) with wavelength less than 20 nm. The material is located between the radiation

source and a piece of film that is sensitive to given radiation. When the radiation is emitted, a portion of radiation will penetrate through the material, and the remaining portion will be absorbed by the material. The amount of absorption would vary depending on the thickness or the density of the material, resulting in variations of the darkness of the film [170]. The variations of the shadowgraph darkness provide useful information about the thickness and the composition of the material, and the presence of flaws. Radiography has been employed to detect flaws in welds [171], aircraft [172], concrete [170], and pipeline [173]. For examples, Kolkoori *et al.* [172] implemented an X-ray backscatter technique to inspect stringers that are critical components in the aircraft wing to transfer the bending loads on the aircraft skin onto the ribs and spars. Liao *et al.* [174] developed an automated radiographic system with four major processes of the preprocessing, curve fitting, profile-anomaly detection, and postprocessing to identify flaws in welds. Although a radiography technique can detect both external and internal defects with very few material limitations, it is usually hazardous to the operators and capability to locate defects highly depends on its orientation to the beam [170], and it is often limited to laboratory-scale evaluations due to their bulky instruments.

5.2.3 Ultrasonics

An ultrasonic method or pulse-echo technique involves transmission and reflection of mechanical stress waves through a material at frequency ranges of 20 kHz–200 MHz. Piezoelectric transducers are usually employed to transmit ultrasonic wave into the objective. Ultrasonic sensing can estimate the thickness of a specimen, the existence, size, and location of defects, and material properties such as density and elastic constants (*i.e.*, Young's modulus, Poisson's ratio, etc.) by investigating an amplitude, time-of-flight, and phase of the reflected wave [175]. It has broad applications in the aircraft [176], bridge [177], wind turbine [178, 179], pipeline [180], and so on.

Despite the advantages, ultrasonic sensing might not be applicable to the materials with high attenuation characteristics, which makes flaw detection challenging. Since a good coupling between the transducer and the surface of the material is needed to prevent wave scattering, coupling agents such as petroleum jelly and grease are usually used. However, if the surface geometry is not even, the coupling between the surface and transducer can be challenging [177].

5.2.4 Fiber-Optic Sensing

Fiber Bragg grating (FBG) optical sensors are widely used fiber-optic sensors which offer the unique capability of measuring strains. For example, Chan *et al.* [181] installed FBG sensors on a hanger cable, rocker bearings, and a truss girder of the Tsing Ma Bridge, Hong Kong for strain measurements, and the results were compared with the conventional strain gages. Besides locating FBG sensors on structural surfaces, there have been efforts to embed FBG sensors within composite structures [182, 183]. While they are immune to electromagnetic (EM) interference and are highly sensitive to strains [184], their complex and expensive data acquisition system, as well as their high manufacturing and installation costs, can limit their use cases. More importantly, FBG sensors do not provide truly distributed sensing, since they can only monitor structural strains at a finite number of locations.

In order to overcome the discrete sensing limitation of traditional FBGs, the fiber optic sensing community has developed sensors based on Rayleigh or Brillouin scattering principles. These sensors provide distributed sensing of strain, with spatial resolutions on the order of a few centimeters, by monitoring changes in the light scattering properties caused by strain [185, 186]. More specifically, Rayleigh scattering is caused by non-propagating elastic density fluctuations, whereas Brillouin scattering is based on the inelastic interaction of sound waves traveling in opposite directions. Distributed sensing in Rayleigh and Brillouin scattering fiber optic sensors are

achieved by various versions of Optical Time Domain Reflectometry (OTDR) [187, 188]. This implementation of OTDR requires a very large frequency bandwidth of the probing light in order to achieve small spatial resolution on the order of millimeters. The need for a tunable laser light source complicates the system and poses additional limits to the achievable scan rate, which, in turn, limits the range of dynamic strain measurements.

5.3 Distributed Sensing using ETDR

5.3.1 ETDR Background

ETDR is an electrical measurement technique that propagates an EM wave in a transmission line and examines the reflected wave in the line. A transmission line is an electrical conductor designed to carry alternating current, and its length is longer than 10% of an EM wavelength [189]. ETDR is widely used in the power and communication industries to locate faults at any point along a transmission line. ETDR entails propagating an EM pulse in the transmission line and then observing characteristics of the reflected pulse. The duration, shape, and magnitude of the reflected waveform contain rich information about impedance variations in the transmission system.

If there is any discontinuity in the characteristic impedance along the transmission line due to damage, that portion induces a reflected wave due to impedance mismatch. The reflection is generally quantified by a reflection coefficient (Γ) defined by the amplitude of the reflected voltage wave (V^-) normalized by the amplitude of the incident voltage wave (V^+) [189]:

$$\Gamma = \frac{V^-}{V^+} = \frac{Z_1 - Z_0}{Z_0 + Z_1} \tag{5.1}$$

where Z_0 and Z_1 are the characteristic impedances before and after the discontinuity, respectively (Figure 5.1). When the transmission line is intact, where $Z = Z_0 = Z_1$, there is no reflected wave,

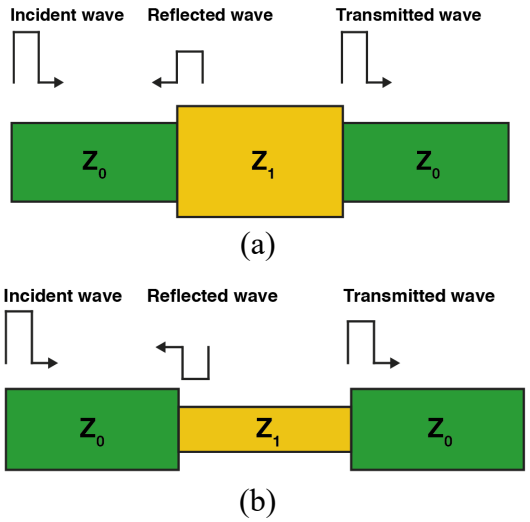

Figure 5.1. An impedance mismatch in a transmission line creates a reflected wave (a) if $Z_1 > Z_0$ or (b) $Z_1 < Z_0$.

and the EM wave will continue to propagate in the line. On the other hand, when an impedance discontinuity ($Z_0 \neq Z_1$) exists, a wave that carries the information about the discontinuity will be reflected (Figure 5.1).

Here, two different scenarios are illustrated. First, when $Z_1 > Z_0$, it creates a positive reflection ($\Gamma > 0$) (Figure 5.1a). Second, when $Z_1 < Z_0$, negative reflection is induced ($\Gamma < 0$) (Figure 5.1b). With the known propagation velocity of the incident wave (v) and the measured time difference between the incident and reflected waves (Δt), the location of impedance discontinuity (l) can be determined:

$$l = \frac{v\Delta t}{2} \tag{5.2}$$

5.3.2 ETDR Sensors

Early studies in geotechnical engineering introduced ETDR for rock deformation detection [190] and soil water content measurements [191]. For SHM applications, Liu *et al.* [192] suggested a twin-conductor transmission line that consisted of a bridge cable and a sensor wire for detecting

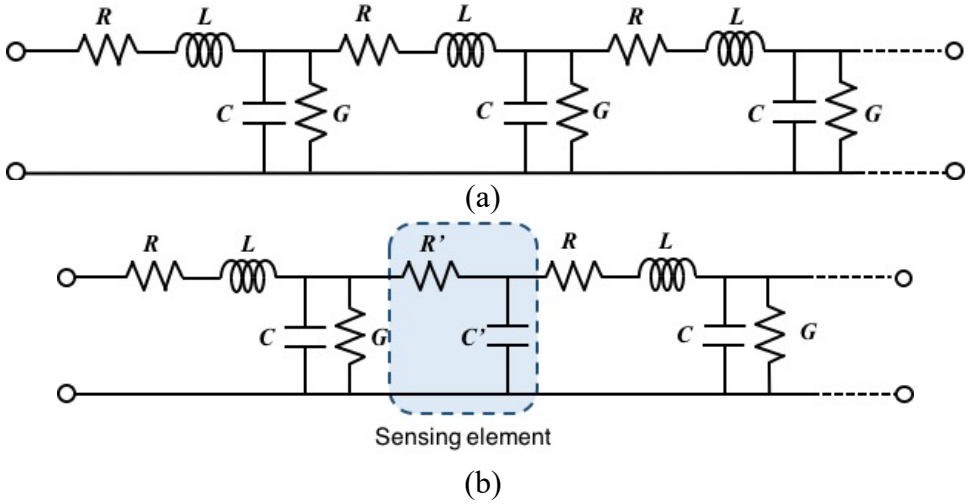

Figure 5.2. (a) An equivalent circuit of a transmission line can be described by *R*, *L*, *C*, and *G*, and (b) a modified transmission line with an MWCNT-based sensing element can be modeled using *R'* and *C'*.

steel cable corrosion. Corrosion was simulated by cutting several strands of the 0.95-m-long steel cable, and simulated damage locations were successfully determined from ETDR measurements. Lin *et al.* [193] replaced the dielectric part of a coaxial cable with rubber and compared its strain sensing response with that of an RG-174 cable that uses either polyethylene or Teflon for its dielectric. ETDR results showed that the proposed coaxial cable sensor was more sensitive to strains, which was enabled by the greater compliance of rubber. Unlike fiber optic sensors, its simple system architecture without the need of a laser light source, as well as low manufacturing and installation costs, would make ETDR implementation easier.

The distributed electrical characteristics of a transmission line are described by its series resistance (*R*), series inductance (*L*), shunt conductance (*G*), and shunt capacitance (*C*) [189]. An equivalent electrical circuit of a typical transmission line is shown in Figure 5.2a. Three approaches have been used to design an ETDR sensor for SHM, namely by: i) employing a conventional transmission line; ii) adjusting the geometry of the transmission line; and iii) incorporating the target structure as part of the transmission line.

First, Lin *et al.* [194] used a commercial coaxial cable transmission line to detect cracks in a reinforced concrete beam. However, conventional transmission lines are intended to transmit EM signals such that their geometry and dielectric materials are designed to prevent reflections during varying environmental conditions [195]. Therefore, if a typical transmission line is used for measuring structural response, impedance changes are barely induced, and its sensitivity might not be enough for practical monitoring applications. Second, to improve sensitivity, Chen *et al.* [196] modified the geometry of the outer part of a coaxial cable with spiral wrapping so that the gap between adjacent spirals separate easily when subjected to mechanical loading. Finally, another approach is to use the monitored structure as part of the ETDR system [197, 198]. Todoroki [197] used carbon fiber-reinforced polymer (CFRP) as the conducting part of a transmission line to monitor bearing failure. The transmission line had a sandwiched structure of copper tape (*i.e.*, signal conducting layer), glass fiber-reinforced polymer (GFRP) (*i.e.*, dielectric layer), and CFRP composite (*i.e.*, electrical ground layer). A 6 mm-diameter fastener hole was created in a 200×1,850 mm^2 specimen, and several impact loadings (10–30 J) were applied to the fastener by dropping weights. Impact damage was captured by ETDR when the energy of impact load was larger than 20 J. Pandey *et al.* [198] used a conductive layer with GFRP-based composites as the dielectric part and two copper plates as conductors. The copper plates were connected to a coaxial cable for EM signal propagation. The specimen was subjected to cyclic loading-unloading, and the results showed that the ETDR response followed the applied strains.

This chapter proposes a unique approach to design distributed ETDR strain sensors by integrating piezoresistive MWCNT-based sensing elements at different locations along the transmission line. In this case, the transmission line was a parallel wire (*i.e.*, speaker wire), which can be modeled by Figure 5.2a with four electrical components (R, L, C, and G). The MWCNT-based sensing element was a parallel-plate capacitor with two conductive layers (*i.e.*, MWCNT

thin films or copper tapes) separated by a dielectric layer of MWCNT-epoxy or pristine epoxy, which can be modeled as an *RC* element [199, 200] (Figure 5.2b). The rationale for using the MWCNT-based elements was because of their intrinsic piezoresistivity, which can be tuned and controlled during nanocomposite fabrication for improving strain sensitivity. In addition, a parallel-plate-type transmission line sensing element was used, since uniform penetration of EM fields can enhance sensitivity [198].

5.4 Numerical Simulations

5.4.1 Numerical Modeling Procedures

The nanostructure of piezoresistive MWCNT-based sensing elements was designed by simulating CNT thin film models. Chapter 3 and Chapter 4 demonstrated how geometrical features of dispersed CNTs and length distributions affect the electrical and electromechanical behavior of CNT-based thin film strain sensors. This study explored how CNT orientations influence bulk-film piezoresistive or strain sensing properties. Unlike Chapter 3 and Chapter 4, the geometry of CNT was assumed to be straight to solely consider their alignment effects on the strain sensing properties. The degree of CNT-network alignment was described by limiting the maximum angle (θ_{max}) between longitudinal axis (y) and CNT axis. The orientation of each CNT was then defined by the angle θ between the CNT axis and the horizontal axis (x) (Equation 5.3). By doing so, a CNT can be randomly located within the maximum angle of θ_{max}.

$$\theta = 90 + \theta_{\max} \times 2 \times (rand - 0.5) \tag{5.3}$$

For example, $\theta_{max} = 90°$ describes the perfect random dispersion of the CNT-network. As θ_{max} decreased, CNTs were more aligned with the y-axis or the direction of the electrical measurement.

Upon defining the CNT orientations, the location of each CNT was determined by two end-points (x_1, y_1) and (x_2, y_2) in a Cartesian coordinate system, which was similar to Chapter 2. One end of CNT was randomly located within the dimension of the CNT thin film model (4×24 μm^2). The other end was calculated using a CNT length (L_{CNT}) and a CNT orientation (θ):

$$x_2 = x_1 + L_{CNT}\cos\theta \tag{5.4}$$

$$y_2 = y_1 + L_{CNT}\sin\theta \tag{5.5}$$

The procedure was iterated until the predefined number of CNTs (N) was generated. A Gaussian distribution of CNT lengths (mean: 1.904 μm and standard deviation: 0.506 μm) was applied to the model. A set of representative models with different alignment conditions (θ_{max} = 10°, 30°, and 90°) was shown in Figure 5.3. With the CNT-based thin film model generated, electrical property and strain sensing simulations were conducted by following the procedures described in Chapter 2. R_{jct} was 240 kΩ, and intrinsic strain sensitivity (S_{CNT}) of CNTs was set as 150.

5.4.2 Numerical Simulation Results

In this study, five different CNT orientation conditions of θ_{max} = 10°, 20°, 30°, 60°, and 90° were employed. First, the percolation thresholds were simulated. The percolation thresholds were N = 220, 230, 300, 400, and 700 for θ_{max} = 90, 60, 30, 20, and 10°, respectively. The results of electrical resistance are shown in Figure 5.4. CNT-based thin film models were more conductive with more CNT inclusions. On the other hand, the electrical property varied depending on the CNT alignment conditions, although the number of CNTs was the same. The CNT thin film models with

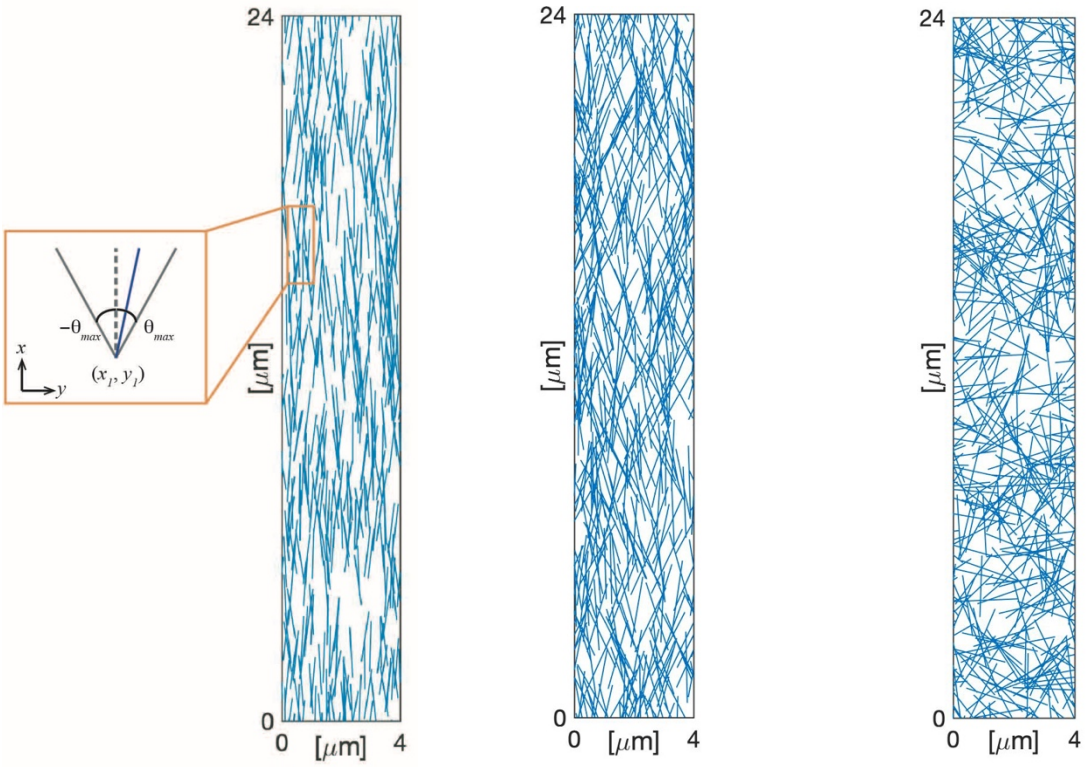

Figure 5.3. CNT thin film models with different CNT orientation conditions are shown: (a) θ_{max}=10°, (b) θ_{max}=30°, and (c) θ_{max}=90°.

θ_{max} = 60° were always more conductive than CNT-network with random CNT orientations (θ_{max} = 90°) regardless of CNT density. However, except θ_{max} = 60°, there was no clear relationship between the model's electrical resistance and CNT orientations. For example, random CNT-networks (θ_{max} = 30°) had a higher resistance than CNT networks with θ_{max} = 30° at lower CNT density ($N \sim 300$), while CNT-networks with θ_{max} = 30° was more conductive at higher CNT density ($N \geq 400$). A possible explanation of the results is that there is a fundamental competition between a decrease in the number of junctions indicating losing the conducting pathways and a decrease in the length of conducting paths favorable to the current flow. These results were consistent with other numerical and experimental studies [117, 201]. Figure 5.5 showed the strain

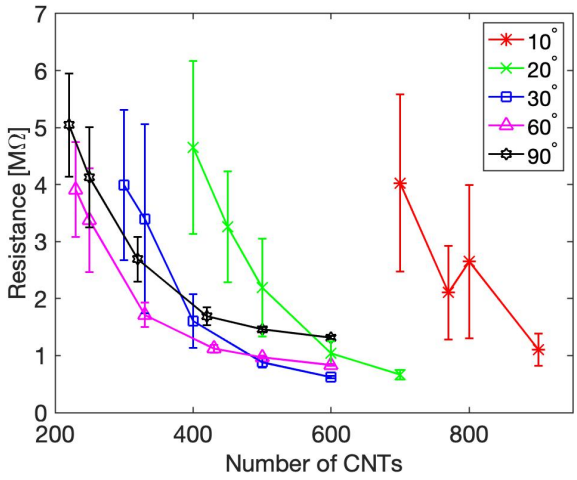

Figure 5.4. Unstrained resistance was simulated according to different CNT alignment degrees and number of CNTs.

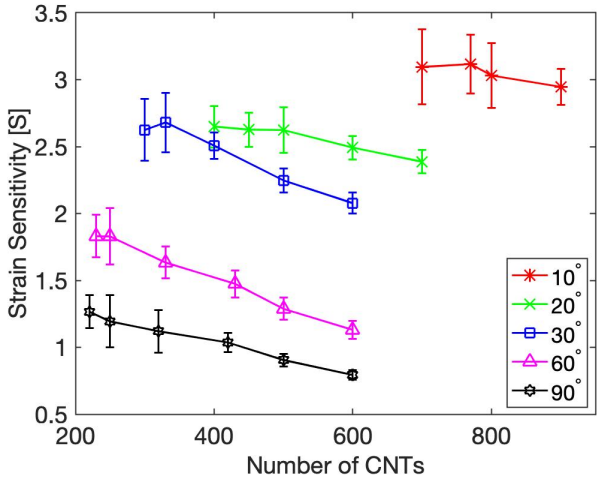

Figure 5.5. Model strain sensitivity was estimated with varied CNT orientations and number of CNTs.

sensitivity results of the CNT-based thin film model. Unlike the results of the electrical resistance simulation, a clear trend was found that the model sensitivity increased as θ_{max} decreased. According to the numerical simulation results, one can expect that CNT-based thin films with aligned CNTs would be more sensitive to strain. Inspired by numerical simulation results, two different MWCNT-Pluronic thin films (one with random MWCNT dispersion and the other with aligned MWCNT dispersion) were incorporated in an ETDR sensor.

5.5 Experimental Details

5.5.1 Materials

MWCNTs were purchased from NanoIntegris, and UV-curable epoxy (OG198-54) was acquired from EPO-TEK®. Pluronic F-127 (Pluronic) (M_W = 12,600) was from Sigma-Aldrich. Dragon Skin® FX-Pro (Dragon Skin) was acquired from Smooth-On. Hydrophilic PTFE membrane filters (diameter: 47 mm and pore size: 0.2 μm) were purchased from EMD Millipore.

5.5.2 Nanocomposite Sensing Element Fabrication

The ETDR parallel-plate nanocomposite sensing element fabrication started with the preparation of its conducting part, which was the MWCNT-Pluronic thin film. Here, 1 mg/mL MWCNTs were dispersed in 0.5 wt% Pluronic solution. Dispersion was achieved by subjecting the mixture to 60 min of high-energy tip sonication. Second, two types of MWCNT-Pluronic thin films were assembled. MWCNT thin film #1 was fabricated by vacuum filtering the MWCNT-Pluronic dispersion using a PTFE membrane. Fabrication of MWCNT thin film #2 followed the same procedure, except that a 30 kHz AC voltage of 2.8 kV_{p-p} was applied to the solution for 10 min, immediately prior to it being vacuum filtered; the resulting electric field, E, was 87.5 V_{p-p}/mm. It should be noted that E was applied to the solution using two parallel-plate electrodes mounted on opposite sides of the 3D-printed chamber directly above the filtering membrane and setup. Upon filtration, the thin films were air-dried for 12 h. The film was cut to form rectangular specimens (3×22 mm^2 or 3×11mm^2). Specifically, MWCNT thin film #2 was cut such that the electric field direction is parallel to the longer side of the thin films. SEM images of MWCNT thin films show that MWCNT thin film #1 that had a randomly dispersed network (Figure 5.6a) which can be described by the CNT-thin film model with random dispersion (Figure 5.3c). Similar to the

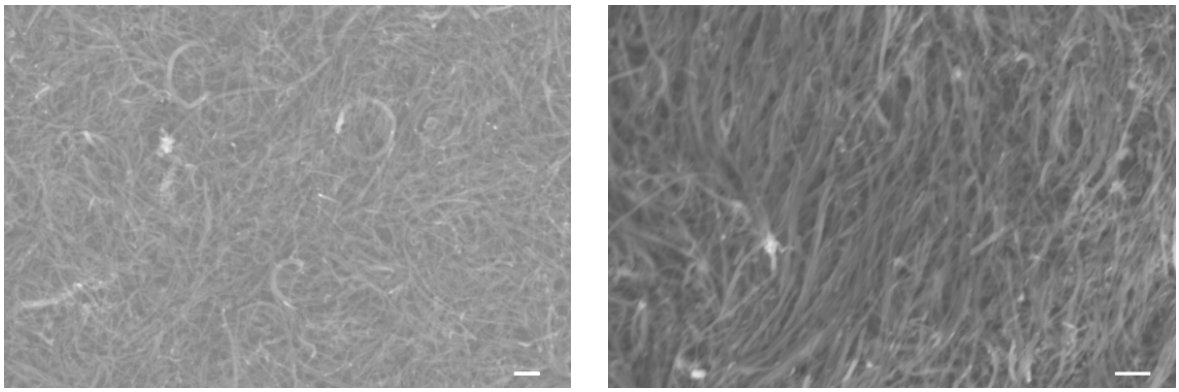

(a) (b)

Figure 5.6. SEM images of (a) the randomly dispersed MWCNT-Pluronic thin film (MWCNT thin film #1) and (b) the aligned MWCNT-Pluronic thin film (MWCNT thin film #2) are shown. The scale bar represents 200 nm.

aligned CNT thin film model (Figure 5.3a and 5.3b), MWCNT thin film #2 shows nanotube alignment in the direction of the applied electric field due to dielectrophoresis [202] (Figure 5.6b).

The dielectric portion of the ETDR sensors was based on two different thick films (*i.e.*, epoxy and 0.1 wt% MWCNT-epoxy) to study how their dielectric properties affected strain sensing. Preparation of the dielectric begun by dispersing MWCNTs in epoxy via high-speed shear-mixing for 2 min at 3,500 rpm and then high-energy tip sonication for 2 min. This was repeated five times for achieving uniform dispersion. The viscous mix was then cast in dog-bone shaped Dragon Skin molds. Curing was performed using an ultraviolet (UV) lamp (Uvitron Porta-ray 400R) for 10 min, followed by curing in a Yamato ADP-300C oven for 12 h at 70 °C. Preparation of the pristine epoxy followed the same curing process. The thickness of the final dog-bone shaped epoxy thick films was ~1.15 mm (Figure 5.7a).

The parallel-plate sensing element was then formed by attaching the conductive portion (*e.g.*, MWCNT-Pluronic thin film) to both the top and bottom of the dielectric (*e.g.*, MWCNT-epoxy). Electrodes were created at opposite ends of the thin films using copper tape (3×10 mm^2) and then drying colloidal silver paste (Ted Pella) at their interface to minimize contact impedance.

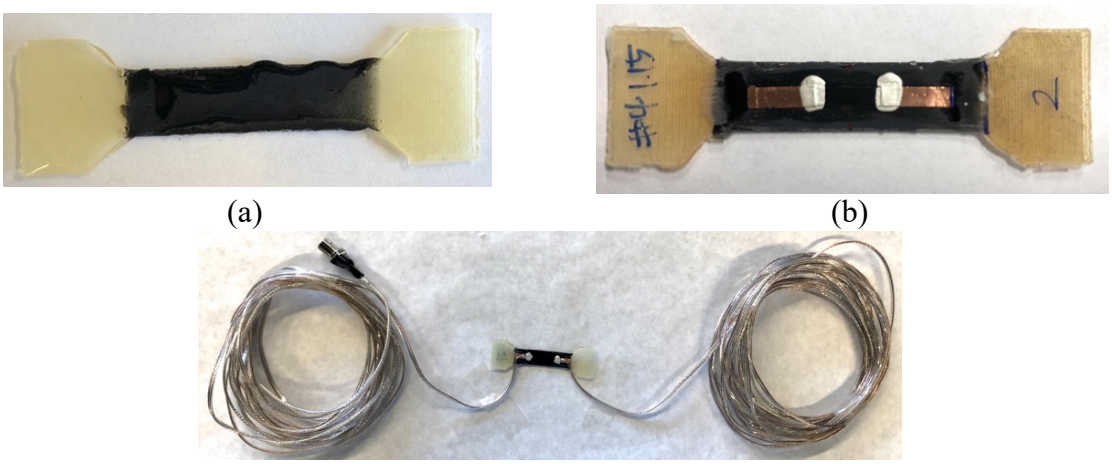

Figure 5.7. An MWCNT-based ETDR sensor was assembled by (a) preparing MWCNT-epoxy, (b) attaching MWCNT thin films on it, and (c) connecting the sensing element to the speaker wires.

These electrodes were then connected to speaker wires by soldering (Figure 5.7b). Finally, a BNC connector was soldered to one end of the wire (Figure 5.7c) for ETDR interrogation and measurement purposes.

5.5.3 ETDR Sensor Sample Sets

In this study, five unique ETDR sample sets were prepared. Four of them (*i.e.*, Sensors #1 to #4) were composed of two uniform lengths of parallel wires (l = 7.62 m) connected to opposite ends of the sensing element (Figure 5.8a). These sensors were used to study how their R and C properties affected strain sensing capability (Figure 5.2b). Sensor #1 (Figure 5.9a) was the control sample set and consisted of two parallel copper tape strips (3×38 mm^2) attached to a dog-bone-shaped epoxy dielectric. Sensor #2 (Figure 5.9b) employed MWCNT thin film #1 for the conductor, separated by pristine epoxy. Sensor #3 (Figure 5.9c) also used MWCNT thin film #1 for the conductor but was separated by the MWCNT-epoxy thick film as the dielectric. Sensor #4

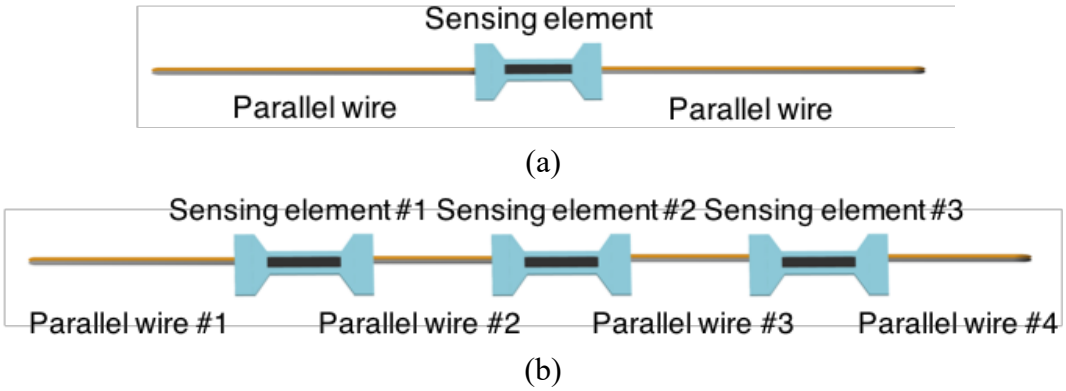

Figure 5.8. Two different types of MWCNT-based ETDR sensors were used: (a) one sensing element connected to two parallel wires and (b) three sensing elements connected to four parallel wires.

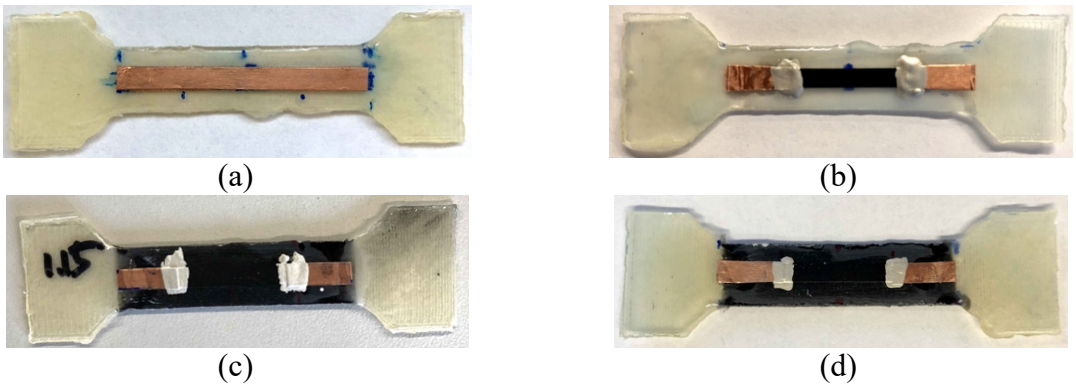

Figure 5.9. Four types of sensing elements that were fabricated are shown: (a) copper tapes on epoxy; (b) MWCNT thin films on epoxy; (c) MWCNT thin films on MWCNT-epoxy composite; and (d) AC-voltage-treated MWCNT thin films on MWCNT-epoxy composite.

(Figure 5.9d) was identical to Sensor #3, except that MWCNT thin film #2 was used.

For the final case, Sensor #5 incorporated three sensing elements for validating distributed strain sensing (Figure 5.8b), each separated by 4.57 m of parallel wire. It should be noted that the length of the first parallel wire (*i.e.*, between the first sensing element and the BNC connector) was 7.62 m. The sensing elements were identical to those used in Sensor #3, except that the MWCNT-Pluronic films were smaller (3×11 mm^2).

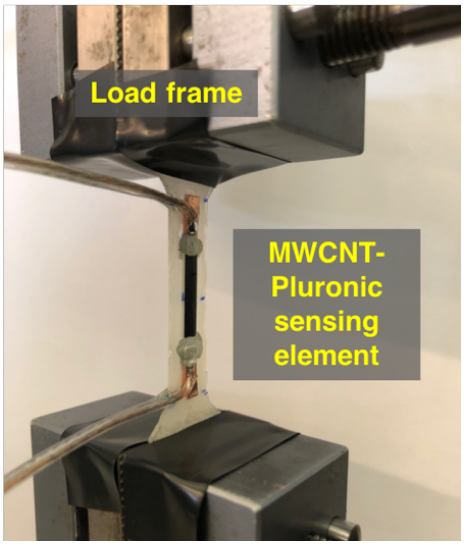

Figure 5.10. An MWCNT-based sensing element was mounted in the load frame for strain sensing tests.

5.5.4 ETDR Strain Sensing Characterization

All five types of ETDR sensors were subjected to loading-unloading tests. Here, only the MWCNT-based sensing element was mounted in the Test Resources 150R load frame (Figure 5.10). A preload of 0.5 N was first applied to ensure that the sensing element was taut. A baseline set of measurements was obtained by using a Keysight 33600A waveform generator to inject a 10 $V_{p\text{-}p}$, 60 MHz, one-cycle, sine wave. A Keysight DSOX3024T digital oscilloscope was also connected to record the reflected waveform response (Figure 5.11). Then, a one-cycle uniaxial tensile load pattern to 0.5% was applied to strain the sensing element. The load frame was paused at every 0.1% strain increment to acquire a set of ETDR measurements.

5.6 Results and Discussion

5.6.1 Unstrained ETDR Sensor Response

As discussed in Section 5.5.4, the ETDR sensors were first mounted in the load frame before they were strained, and baseline ETDR waveforms were obtained. Figure 5.12 summarizes

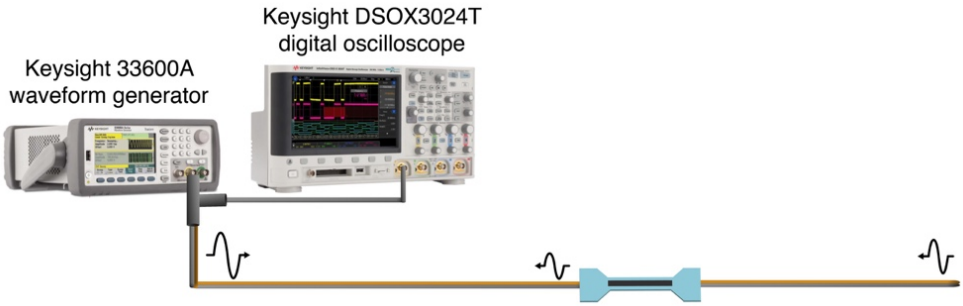

Figure 5.11. An ETDR system is composed of a waveform generator, a digital oscilloscope, and the ETDR sensor.

the unstrained ETDR measurement results. It can be seen that Sensors #1 to #4 all showed two reflected waves. When an incident wave was transmitted through an ETDR sensor, a portion of the wave reflected (Reflected wave #1) due to impedance mismatch between the sensing element and the parallel wire. The remaining portion of the wave was then transmitted, and total reflection occurred (Reflected wave #2) at the end of the ETDR setup due to open-circuit condition ($Z = \infty$). By using Equation 5.2, the velocity of the transmitted wave was estimated as $v = 2.05\times10^8$ m/s, which is ~69% the speed of light ($c = 2.99\times10^8$ m/s). The time difference (Δt) between the incident wave and Reflected wave #1 was similar among the four sensors ($\Delta t \sim 74$ ns), since the location of each sensing element was identical ($l = 7.62$ m).

On the other hand, the amplitudes of the reflected waves' voltages were different due to impedance differences among the four sensing elements, which are summarized in Table 5.1. The voltage amplitude of Reflected wave #1 of Sensor #1 was lower than the other three. This was expected since the resistance of the copper tape ($R = 0.02\ \Omega$) was much lower than that of the MWCNT-Pluronic thin films in the other sensing elements. Thus, more energy was transmitted through Sensor #1, and total reflection occurred at the end of the sensor so that the amplitude of Reflected wave #2 of Sensor #1 was the highest (Figure 5.12a).

For both Sensors #2 and #3, MWCNT thin film #1 was used. The difference was that

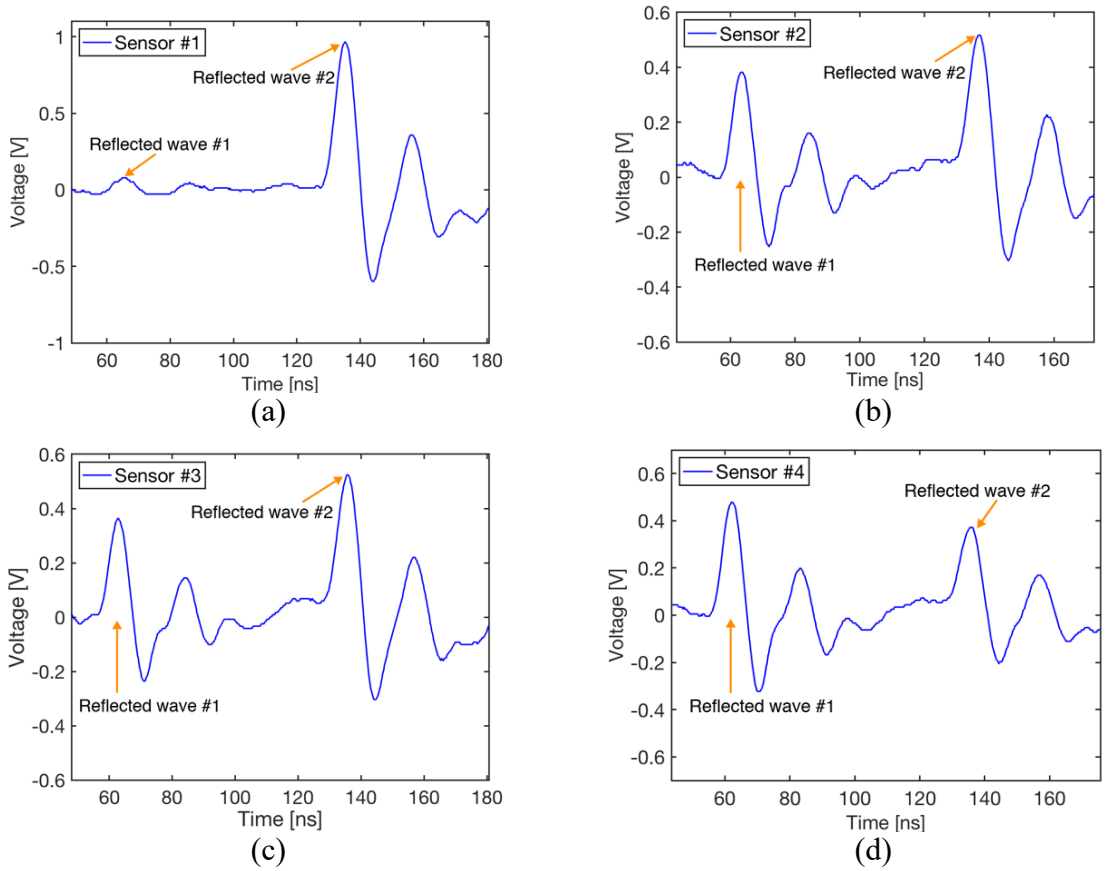

Figure 5.12. The waveform response of each unstrained ETDR sensor is shown: (a) Sensor #1; (b) Sensor #2; (c) Sensor #3; and (d) Sensor #4.

MWCNT-epoxy was used for Sensor #3. This resulted in a smaller reflected voltage amplitude for Sensor #3 (Figure 5.12c), which can be explained by the sensing element's *C* component. It was shown that the dielectric constant of polymer composites was enhanced with the inclusion of CNTs [203, 204], thereby increasing the capacitance and decreasing the impedance.

Although MWCNT-epoxy was used for both Sensors #3 and #4, the voltage amplitude of Reflected wave #1 was higher for Sensor #4 (478 mV) due to its *R* component. *R* of Sensor #3 was ~42 Ω while that of Sensor #4 was ~65 Ω. A similar explanation as the electrical property simulations of the CNT-based thin film model can be applied such that the governing effect of the aligned MWCNT-Pluronic thin film was decrease in conducting pathways over the decrease in the length of conducting paths. To be specific, aligned MWCNTs were less likely to overlap and form

Table 5.1. Voltage amplitudes of reflected waves.

Sensor ID	Reflected wave #1 voltage [mV]	Reflected wave #2 voltage [mV]
Sensor #1	63	967
Sensor #2	384	517
Sensor #3	363	524
Sensor #4	478	372

connective conducting pathways due to their high length-to-diameter ratio (*i.e.*, aspect ratio). Therefore, given the larger impedance of the conductor in the transmission line, this resulted in a larger reflected wave voltage amplitude for Sensor #4.

5.6.2 ETDR Strain Sensing Results

After the baseline ETDR measurements, one cycle of uniaxial tensile strains was applied to each sensing element. Figure 5.13 summarizes the response of Sensor #2. Figure 5.13a overlays the voltage peaks of Reflected wave #1 with respect to different applied strain states. The voltage peak increased as the sensing element was strained in tension. The results can be explained by the strain sensing results of MWCNT-based thin films (Chapter 4), where the electrical resistance of MWCNT-based thin films increased when strained in tension. To better quantify strain sensing behavior, the change in voltages (ΔV) with respect to the unstrained peak voltage was calculated:

$$\Delta V = V_i - V_0 \tag{5.3}$$

where V_i is the peak voltage of the reflected wave at the i^{th} strain state, and V_0 is the peak voltage of the initial unstrained reflected wave. Figure 5.13b shows that ΔV changed in tandem with applied stains, thus validating strain sensing using ETDR.

Similar to Sensor #2, ΔV of Sensors #3 (Figure 5.14) and #4 (Figure 5.15) followed the applied strain pattern as well. To compare the strain sensing behavior among all four sample sets,

their ΔV responses were overlaid and shown in Figure 5.16. First, Sensor #1 exhibited the worst

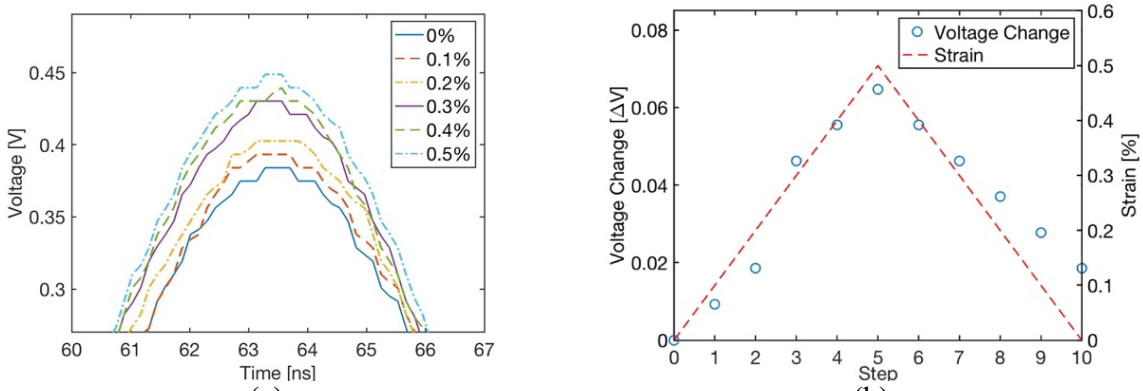

(a) (b)

Figure 5.13. Sensor #2 was subjected to uniaxial tensile loading and unloading. (a) The peaks of the reflected waves at different strain states are overlaid, and (b) the changes in peak voltage are overlaid with the applied strains.

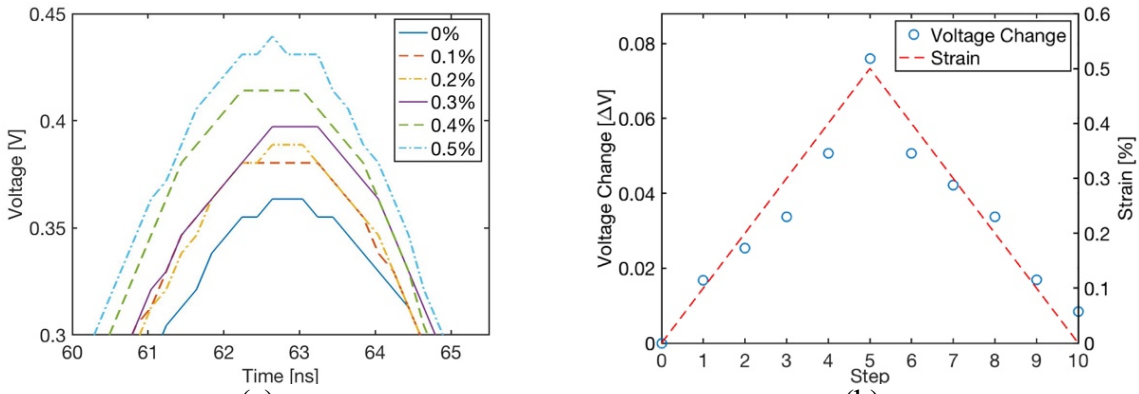

(a) (b)

Figure 5.14. Sensor #3 was subjected to uniaxial tensile loading and unloading. (a) The peaks of the reflected waves at strain states are overlaid, and (b) the changes in peak voltage are overlaid with the applied strains.

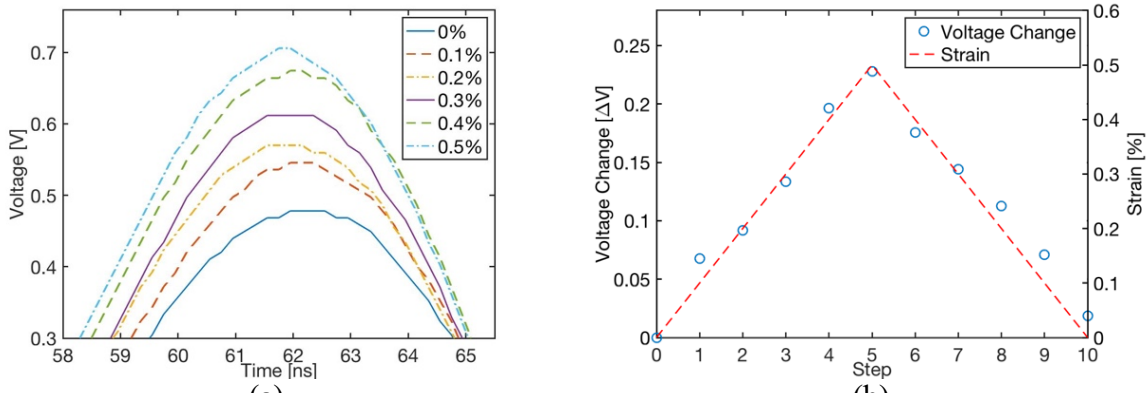

(a) (b)

Figure 5.15. Sensor #4 was subjected to uniaxial tensile loading and unloading. (a) The peaks of the reflected waves corresponding different strain states are overlaid, and (b) the changes in peak voltage and the applied strains are plotted as a function of steps.

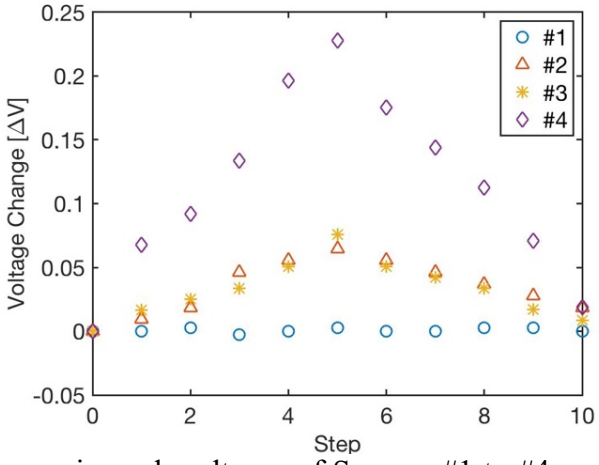

Figure 5.16. The changes in peak voltages of Sensors #1 to #4 are plotted as a function of steps.

performance. Sensor #1 used copper tape as conductors, and its electrical impedance did not respond to strain. Second, ΔV of Sensors #2 and #3 were comparable, but Sensor #3 showed slightly higher ΔV at 0.5 % strain (ΔV = 76.0 mV) versus Sensor #2 (ΔV = 64.7 mV). Last, Sensor #4 demonstrated the highest sensitivity to applied strains.

To investigate the underlying mechanism of the results obtained in Figure 5.16, the sensitivity of R (for the conductor) and C (for the dielectric) to applied strains were individually analyzed. First, C was investigated by measuring capacitance of epoxy and MWCNT-epoxy as they were strained. When specimens are subjected to deformation, C would be varied, because the thickness, area, and dielectric constant of the specimen changes [205]. Rectangular epoxy films ($10\times60\times1$ mm^3) were prepared, and copper films (10×38 mm^2) were affixed to its top and bottom surfaces. Similar to the aforementioned ETDR strain sensing tests, the specimen was loaded by applying one cycle of tensile strains and pausing every 0.125% for capacitance measurements using a Keysight E49080A LCR meter. The procedure was repeated until a maximum strain of 0.75% was reached, which was followed by unloading to 0%. The LCR meter applied a 1 $V_{p\text{-}p}$, 2 MHz, sinusoidal excitation signal.

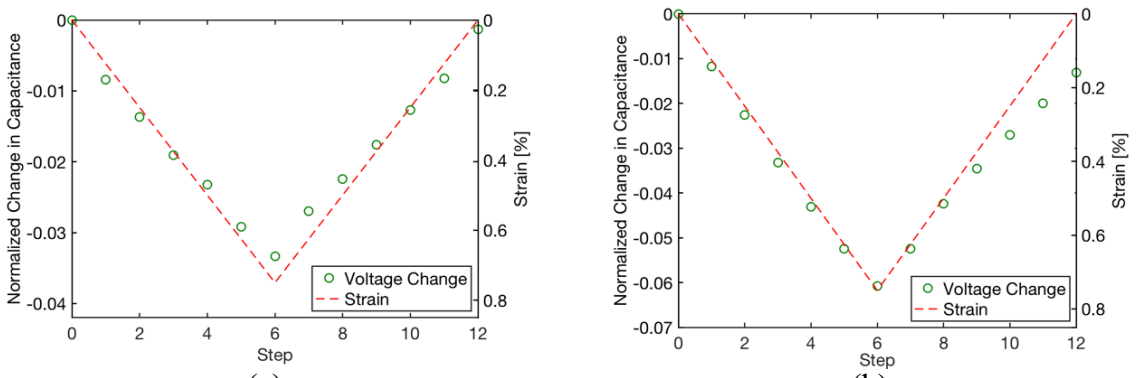

Figure 5.17. Normalized changes in capacitances overlaid with applied strain patterns are shown: (a) epoxy and (b) MWCNT-epoxy composite.

To compare the capacitance results, normalized change in capacitance (C_{norm}) was calculated:

$$C_{norm} = \frac{\Delta C_i}{C_0} \tag{5.4}$$

where C_0 is the initial unstrained capacitance of the specimen, and C_i is the change in capacitance at the i^{th} strain state. Representative results of the pristine and MWCNT-epoxy are shown in Figure 5.17. It can be seen that C_{norm} of both specimens followed the applied strain pattern, but C_{norm} for the MWCNT-epoxy was more sensitive to applied strains, which is consistent with other studies [199]. Although capacitance was measured at a lower frequency (f = 2 MHz) as compared to the ETDR excitation signal, it was found that the dielectric constant (or capacitance) plateaus at frequencies above 10 kHz [206].

Second, the R component of the ETDR sensing element was also tested. Here, MWCNT thin films #1 and #2 were prepared. Each thin film was attached to the dog-bone shaped epoxy. The dimensions of the film and gage length between electrodes were consistent with previous ETDR tests. The specimens were mounted in the load frame and subjected to two cycles of tensile loading-unloading at a strain rate of 0.04%/min and to a maximum strain of 0.5%. Figure 5.18 summarizes the results. The unstrained resistance of MWCNT thin film #1 (R = 44.2 Ω) was lower

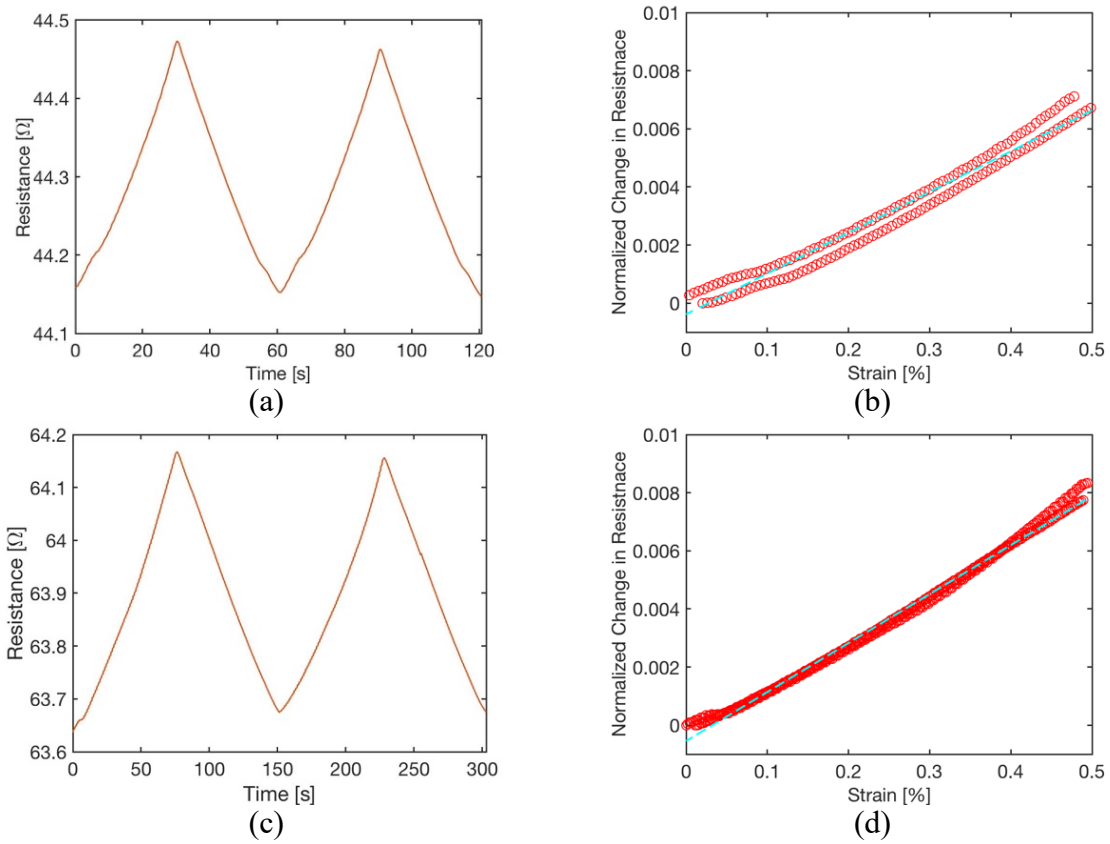

Figure 5.18. (a) The electrical resistance response of MWCNT thin film #1 is shown. (b) The normalized change in resistance of MWCNT thin film #1 is plotted as a function of applied strains. (c) The electrical resistance time history of MWCNT thin film #2 is plotted. (d) The normalized change in resistance of MWCNT thin film #2 versus applied strains is shown.

than that of #2 (R = 63.6 Ω). It can be observed from Figures 5.18a and 5.18c that both thin films showed linear strain sensing response. Strain sensitivity for each specimen was estimated by fitting a linear least-squares regression line to the plot of R_{norm} versus strain (Figures 5.18b and 5.18d). It was found that strain sensitivity for MWCNT thin film #2 (S = 1.62) was higher than that of #1 (S = 1.41). This was expected from the numerical simulations (Section 5.4), in which CNT thin film models with aligned CNTs along the loading direction produced higher bulk strain sensitivity. The increase in strain sensitivity of the thin film directly translated to the higher ETDR strain sensitivity. These results suggest that the R component and its piezoresistivity are dominating factors that influence ETDR strain sensing performance. In addition, by manipulating the sensing element's

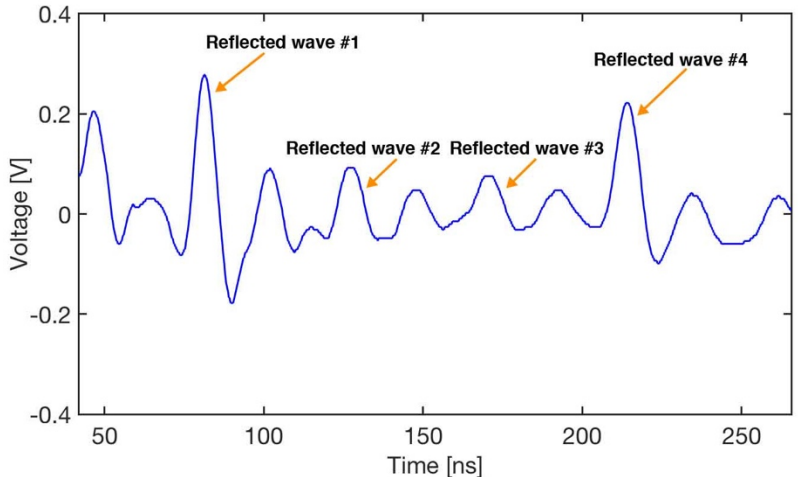

Figure 5.19. The waveform response of Sensor #5 is plotted as a function of time.

nanostructure, ETDR strain sensing response can be designed or tuned.

5.6.3 Distributed Strain Sensing Validation

Finally, distributed strain sensing was validated using Sensor #5 that included three sensing elements in the transmission line. The electrical resistance of all MWCNT thin films was ~20 Ω. As before, a set of baseline ETDR measurements was obtained prior to straining the sensing elements. Figure 5.19 shows that the measured response is somewhat complicated. However, the location of the incident wave (t = 7.72 ns), which is not shown in Figure 5.19, and that of the final reflected wave (Reflected wave #4) are apparent (t = 214.60 ns). Thus, the velocity of the EM wave can be calculated using Equation 5.2 to give $v = 2.06 \times 10^8$ m/s. With the known location of the three sensing elements, the locations of other reflected waves could be estimated and are marked in Figure 5.19.

Strain sensing tests were then performed by straining one of the three sensing elements while keeping the others unstrained. This was repeated until all of the sensing elements were strained and tested. The results are presented in Figure 5.20. Similar to Sensors #1 to #4 with one sensing element, all the Sensing elements #1 to #3 clearly showed strain sensing behavior, where

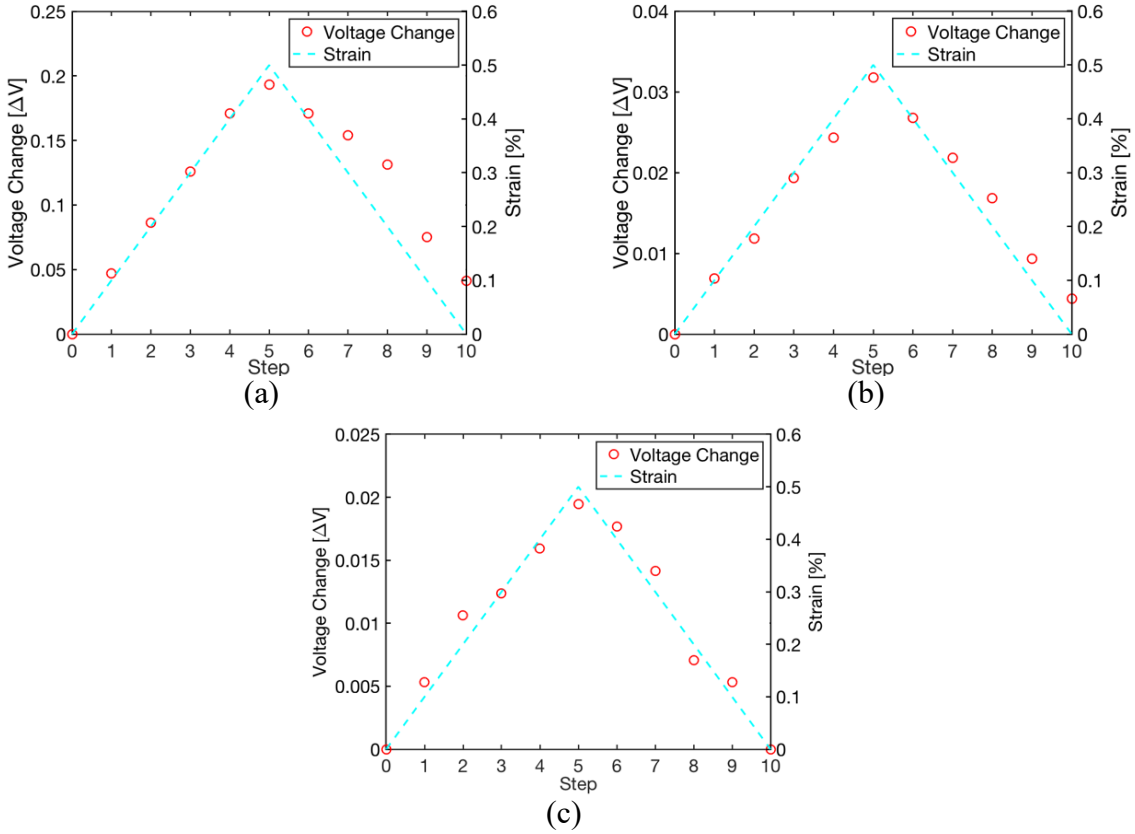

Figure 5.20. Each sensing element of Sensor #5 was subjected to strain sensing tests. (a) The changes in peak voltage of Sensing element #1, (b) Sensing element #2, and (c) Sensing element #3 are overlaid with the (same) applied strain pattern.

their voltage change matched the applied strain pattern, thereby successfully validating distributed sensing. However, the voltage change degraded as the location of sensing element was farther from the probe. To be specific, the first sensing element exhibited greater voltage changes than the other two. A possible explanation can be due to signal attenuation that worsened as the EM wave traveled down the transmission line and with a portion of the energy of the wave lost due to reflections as it interacted with each additional sensing element.

5.7 Summary

In this study, the numerical model of CNT-based thin film was used to guide the design of an MWCNT-based strain sensor. In addition, a new approach for truly distributed strain sensing

was demonstrated by integrating ETDR with MWCNT-based sensing elements. This work investigated different types of sensing elements, where the conductor was formed using MWCNT-Pluronic thin films, and the dielectric was either pristine or MWCNT-epoxy thick films. Especially, two different MWCNT-Pluronic thin films were incorporated in the strain sensor (one with random MWCNT orientations and the other with aligned MWCNTs). This was inspired by the numerical simulation results in which the aligned CNT thin film model was more sensitive to strains than the model with random CNT orientations. Upon integration of these sensing elements in a transmission line, the results showed that all the ETDR responses showed voltage changes that varied linearly with respect to applied strains. Furthermore, it was found that the strain sensitivity or gage factor of the MWCNT-Pluronic thin film conductor element directly influenced the bulk strain sensitivity of the ETDR sensor. The results suggested that the desired strain sensing performance of ETDR sensors could be achieved by controlling thin film nanostructure. Last, to validate distributed strain sensing, three sensing elements were integrated in a single transmission line. Each sensing element was subjected to applied strains, while their voltage responses were recorded using ETDR. Strain sensitivity was confirmed for all the sensing elements, and ETDR could successfully interrogate and acquire their response simply by analyzing the recorded reflected voltage waveforms.

Chapter 5, in part, is a reprint of the material as it appears in may appear in IEEE Sensors, Bo Mi Lee; Kenneth J. Loh; Francesco Lanza di Scalea, 2018. The dissertation author was the primary researcher and author of this paper.

Chapter 5, in part, is a currently being prepared for submission for publication of the material. Bo Mi Lee; Zachary Huang; Kenneth J. Loh. The dissertation author was the primary researcher and author of this material.

Chapter 6. Conclusions

6.1 Summary of Results

The main objective of this dissertation was to provide a 2D CNT-based thin film model that can describe the electrical and electromechanical performance of CNT-based thin films. A 2D CNT-based thin film model was derived and simulated to investigate the key parameters that influence the electrical and electromechanical behavior of CNT-based thin films. Experimental measurements of CNT-based thin films were integrated in the model, and strain sensing behavior of the CNT-based thin film model was experimentally validated. The model was further used to improve the design of a distributed strain sensor for SHM.

In Chapter 2, detailed procedures of deriving the 2D CNT-based thin film were presented. A 2D CNT-based thin film model was generated by randomly dispersing 1D straight CNT elements in a representative model area. First, the nominal electrical properties of the CNT-based thin film models were simulated. The percolation threshold was increased using shorter CNTs. The model was more conductive with longer CNTs at higher CNT densities. Then, electromechanical performance simulations were conducted by subjecting the model to uniaxial tensile-compressive strain patterns. The CNT-based thin film model showed linear electromechanical strain sensing response. The strain sensitivity decreased as the concentration or density of CNTs in the polymer matrix increased. In addition, the thin film models were more

sensitive to applied strains containing CNTs with higher intrinsic strain sensitivity, which was expected.

Chapter 3 integrated experimentally measured CNTs properties (*i.e.*, dispersed shapes and length distribution) into the 2D percolation-based thin film model. AFM topographical images of 1 μg/mL MWCNT-PSS thin films showed various geometrical shapes of as-deposited MWCNTs. The perimeter method was used to measure the lengths of 20 MWCNTs, and the results showed an average length of 1.904 μm and a standard deviation of 0.506 μm. Based on the image analysis results, five different CNT-based thin film models with varied CNT-network morphologies were investigated. The numerical simulation results showed that the dispersed shape of the CNT network significantly influenced the bulk-scale electrical and electromechanical behavior. First, the electrical properties of the thin film model were affected by the effective CNT lengths. In addition, the thin film model with straight CNTs showed the highest strain sensitivity among the five different models, while the model comprising CNTs characterized by three linear segments had the lowest strain sensitivity.

A CNT-based thin film model was experimentally validated in Chapter 4. Seven different concentrations of MWCNT-Pluronic thin films were prepared using vacuum filtration. According to the SEM images of MWCNT-Pluronic thin films, kinked-shaped CNTs were applied to the CNT-based thin film model. The degree of CNT kink was described by the height ratio. The model with higher height ratios was less sensitive to strains. The MWCNT-Pluronic thin films were represented by the CNT thin film model with 20% height ratio. The model was able to accurately describe the strain sensing performance of MWCNT-Pluronic thin films. In addition to the trend of decreasing strain sensitivity as a function of CNT density, values of strain sensitivities were similar to those for the MWCNT-Pluronic thin films. The numerical model was additionally validated by computing the area ratio of MWCNT-Pluronic thin films using SEM images. Area

ratio results of MWCNT-Pluronic thin films were comparable to those of numerical models, thereby successfully verifying the CNT-based thin film models.

Following this successful experimental validation, Chapter 5 leveraged the thin film models for guiding the design of a CNT-based distributed strain sensor for SHM. A distributed strain sensor was assembled by modifying sections of a transmission line with MWCNT-based sensing elements. Four different sets of samples were prepared by using different conducting thin films (*i.e.*, copper tapes, randomly oriented MWCNT-Pluronic thin films, and aligned MWCNT-Pluronic thin films) and different dielectric thick films (*i.e.*, pristine epoxy and MWCNT-epoxy). The aligned MWCNT-Pluronic thin films were chosen based on the numerical simulation results in which the aligned CNT-based thin film model showed higher strain sensitivities as compared to the CNT thin film model with random CNT orientations. The ETDR strain sensing results showed that the piezoresistivity of the MWCNT-Pluronic thin film directly affected the strain sensing behavior of the ETDR sensor. Distributed strain sensing was evaluated by integrating three sensing elements in a single ETDR sensor. The voltage of each sensing element changed in tandem with applied strains, thereby successfully validating their distributed sensing capabilities.

6.2 Contributions

As emphasized in Chapter 1, despite the diverse experimental and numerical studies on CNT-based strain sensors, the lack of understanding of strain-dependent electrical response of CNT-based nanocomposites prevented further innovations. Therefore, the main contribution of this doctoral thesis was to advance the understanding of the fundamental mechanisms behind the electrical and electromechanical properties of bulk CNT-based nanocomposites. To do that, a systematic investigation was conducted through numerical model derivation, model testing and evaluation, and experimental validation. First, the relationship between the electrical and

electromechanical characteristics of CNT-based thin films and parameters (such as CNT length, density, and intrinsic piezoresistivity) was numerically simulated. The CNT-based thin film model was able to explain the strain sensing performance of CNT-based thin films, which is in agreement with other results published in the literature. However, unlike other numerical simulations that could only explain the bulk electromechanical behavior of the nanocomposite, this dissertation significantly improved the accuracy of the CNT-based thin film model by incorporating actual physical properties of CNTs (*i.e.*, dispersed shapes and lengths of CNTs) with uncertainty quantification (*i.e.*, CNT length distribution). By doing so, the CNT-based thin film model was able to successfully reproduce the electromechanical behavior of experimentally tested MWCNT-Pluronic thin films. This accomplishment bridged the current research gap between experimental investigations and numerical simulations of CNT-based thin films.

The second contribution of this dissertation was the demonstration of using a model-enabled design approach for assembling CNT-based thin film sensors for structural health monitoring applications. To date, numerical simulations of nanocomposites have been focused on characterizing and validating the bulk electrical and electromechanical properties of CNT-based nanocomposites. This dissertation used a CNT-based thin film model to guide the design of an MWCNT-based distributed ETDR strain sensor. Before experimentally assembling the ETDR sensor, different designs of CNT-based thin film models were simulated, and their strain sensing responses were estimated. As expected from the strain sensing simulation results, the ETDR strain sensor integrating aligned MWCNT-based thin films was more sensitive to applied strains than randomly oriented MWCNT-based thin films.

In this dissertation, a novel approach for distributed strain sensing addressed the limitations of current sensing approaches for SHM. First, the proposed MWCNT-based ETDR sensor was a truly distributed sensor in that the ETDR sensor was capable of measuring strains at multiple points

along its length; furthermore, distributed sensing could be achieved by only obtaining measurements at one end of the ETDR sensor. This ability addresses the limitations of current discrete sensors (*e.g.*, metal-foil strain gages and accelerometers), which requires separate sensing channels and measurements at their instrumented locations. In addition, the proposed sensor implementation is simpler than other types of distributed sensors (*i.e.*, fiber optic sensors) due to its low manufacturing and installation costs and straightforward system architecture. Since strain sensing of the ETDR sensor was dominated by the piezoresistivity of MWCNT-based thin films, ETDR sensing behavior was controlled by manipulating nanostructures of the MWCNT-based thin films.

Another contribution of this dissertation was to provide guidelines for designing nanomaterial-based or nanocomposite systems. Despite the promise of nanomaterial and nanotechnology as mentioned in Section 1.1, the fundamental limitation that needs to be addressed is the lack of design tools of nanomaterial-based systems. This dissertation significantly improved the accuracy of a CNT-based thin film model so that the model can be employed to guide the design of CNT-based distributed ETDR sensors. Similarly, systematic investigations to uncover driving material mechanisms and a model-enabled design approach on CNT-based nanocomposites can be applied to design other nanomaterial-based systems with optimized material properties.

6.3 Future Work

For future research, the CNT-based thin film model will be further improved by considering the interfacial behavior between CNTs and different polymer matrices. This dissertation focused on CNT parameters during numerical modeling, and the CNT-based thin film models assumed that strain was uniformly distributed throughout the entire film while neglecting

the CNT-matrix interfaces. Future research will use molecular dynamics simulations to advance the understanding of interfacial behavior between CNTs and the polymer matrices. Molecular dynamics simulation results will be used as inputs for the CNT-based thin film model during the coordinate update procedure at a different strain state, thereby achieving an even more comprehensive and sophisticated multi-scale model. This research is expected to explain experimental results that showed different electromechanical behaviors depending on different polymer matrices.

In addition, optimization of a CNT-based strain sensor will be explored. Chapter 4 demonstrated that, although the 0.25 mg/mL MWCNT-Pluronic thin film (lowest MWCNT concentration) was the most sensitive to deformations among the seven MWCNT concentrations studied (0.25, 0.5, 1, 2, 3, 4, and 5 mg/mL), its strain sensing resolution was not ideal. Future research will thoroughly investigate the sensing properties (*i.e.*, strain sensitivity, strain sensing resolution, and accuracy) assembled based on different nanostructures (*i.e.*, random and aligned CNT orientations). Their relationships will then be described by a set of empirical equations. Decision variables, which are inputs to the optimization problem, can be physical properties of CNTs (*e.g.*, CNT length, aspect ratio), CNT density, and the polymer matrix, among others. The objective function will be defined by the optimum property (*i.e.*, strain sensitivity, strain sensing resolution, mechanical strength, or a combination of these). Finally, sensing performance will be optimized by maximizing or minimizing the objective function.

Besides CNTs, other conductive nanomaterials (*e.g.*, graphene, Ag NWs, and Au NWs) are also used for strain sensors. The CNT-based thin film model can be extended to describe the strain sensing response of such electrically conductive nanocomposites. Since conductive nanomaterials can also be regarded as resistor or conductor elements, the CNT equation (Equation 2.3), which described the electrical property of a CNT element, can be modified accordingly. The

same framework presented in this thesis can be followed, where high resolution microscope images of nanocomposites can be used as inputs during modeling. The interface between conductive nanomaterials and the polymer matrices can also be considered. In doing so, the electromechanical performance of other conductive nanofiller-based nanocomposites can be investigated.

References

[1] Kroto H. W., Heath J. R., O'Brien S. C., Curl R. F., and Smalley R. E. C60: Buckminsterfullerene. *Nature*, 318, 162-163, 1985.

[2] Tiwari J. N., Tiwari R. N., and Kim K. S. Zero-dimensional, one-dimensional, two-dimensional and three-dimensional nanostructured materials for advanced electrochemical energy devices. *Progress in Materials Science*, 57 (4), 724-803, 2012.

[3] Jeevanandam J., Barhoum A., Chan Y. S., Dufresne A., and Danquah M. K. Review on nanoparticles and nanostructured materials: history, sources, toxicity and regulations. *Beilstein Journal of Nanotechnology*, 9, 1050-1074, 2018.

[4] Baughman R. H., Zakhidov A. A., and de Heer W. A. Carbon nanotubes-the route toward applications. *Science*, 297 (5582), 787-792, 2002.

[5] Mayorov A. S., Gorbachev R. V., Morozov S. V., Britnell L., Jalil R., Ponomarenko L. A., Blake P., Novoselov K. S., Watanabe K., Taniguchi T., and Geim A. K. Micrometer-scale ballistic transport in encapsulated graphene at room temperature. *Nano Letters*, 11 (6), 2396-2399, 2011.

[6] Ghosh S., Calizo I., Teweldebrhan D., Pokatilov E. P., Nika D. L., Balandin A. A., Bao W., Miao F., and Lau C. N. Extremely high thermal conductivity of graphene: prospects for thermal management applications in nanoelectronic circuits. *Applied Physics Letters*, 92 (15), 1-4, 2008.

[7] Nair R. R., Blake P., Grigorenko A. N., Novoselov K. S., Booth T. J., Stauber T., Peres N. M. R., and Geim A. K. Fine structure constant defines visual transparency of graphene. *Science*, 320 (5881), 1308-1308, 2008.

[8] Zhang X., Li Q., Holesinger T. G., Arendt P. N., Huang J., Kirven P. D., Clapp T. G., DePaula R. F., Liao X., Zhao Y., Zheng L., Peterson D. E., and Zhu Y. Ultrastrong, stiff, and lightweight carbon-nanotube fibers. *Advanced Materials*, 19 (23), 4198-4201, 2007.

[9] Hong S. and Myung S. A flexible approach to mobility. *Nature Nanotechnology*, 2, 207-208, 2007.

[10] Zhou X., Park J.-Y., Huang S., Liu J., and McEuen P. L. Band structure, phonon scattering, and the performance limit of single-walled carbon nanotube transistors. *Physical Review Letters*, 95 (14), 146805, 2005.

[11] Han M., Gao X., Su J. Z., and Nie S. Quantum-dot-tagged microbeads for multiplexed optical coding of biomolecules. *Nature Biotechnology*, 19, 631-635, 2001.

[12] Vincenzo A., Roberto P., Marco F., Onofrio M. M., and Maria Antonia I. Surface plasmon resonance in gold nanoparticles: a review. *Journal of Physics: Condensed Matter*, 29 (20), 203002, 2017.

[13] Zhang X.-D., Wu D., Shen X., Liu P.-X., Yang N., Zhao B., Zhang H., Sun Y.-M., Zhang L.-A., and Fan F.-Y. Size-dependent in vivo toxicity of PEG-coated gold nanoparticles. *International Journal of Nanomedicine*, 6, 2071-2081, 2011.

[14] Junno T., Deppert K., Montelius L., and Samuelson L. Controlled manipulation of nanoparticles with an atomic force microscope. *Applied Physics Letters*, 66 (26), 3627-3629, 1995.

[15] Polyakov B., Vlassov S., Dorogin L. M., Butikova J., Antsov M., Oras S., Lõhmus R., and Kink I. Manipulation of nanoparticles of different shapes inside a scanning electron microscope. *Beilstein Journal of Nanotechnology*, 5, 133-140, 2014.

[16] Devreese J. T. Importance of nanosensors: Feynman's vision and the birth of nanotechnology. *MRS Bulletin*, 32 (9), 718-725, 2007.

[17] Piner R. D., Zhu J., Xu F., Hong S., and Mirkin C. A. "Dip-Pen" nanolithography. *Science*, 283 (5402), 661-663, 1999.

[18] Chou S. Y., Krauss P. R., and Renstrom P. J. Nanoimprint lithography. *Journal of Vacuum Science & Technology B: Microelectronics and Nanometer Structures Processing, Measurement, and Phenomena*, 14 (6), 4129-4133, 1996.

[19] Salata O. V. Applications of nanoparticles in biology and medicine. *Journal of Nanobiotechnology*, 2 (1), 1-6, 2004.

[20] Rioux R. M., Song H., Hoefelmeyer J. D., Yang P., and Somorjai G. A. High-surface-area catalyst design: synthesis, characterization, and reaction studies of platinum nanoparticles in mesoporous SBA-15 silica. *The Journal of Physical Chemistry B*, 109 (6), 2192-2202, 2005.

[21] Chan W. C. W., Maxwell D. J., Gao X., Bailey R. E., Han M., and Nie S. Luminescent quantum dots for multiplexed biological detection and imaging. *Current Opinion in Biotechnology*, 13 (1), 40-46, 2002.

[22] Stratakis E. and Kymakis E. Nanoparticle-based plasmonic organic photovoltaic devices. *Materials Today*, 16 (4), 133-146, 2013.

[23] Cha C., Shin S. R., Annabi N., Dokmeci M. R., and Khademhosseini A. Carbon-based nanomaterials: multifunctional materials for biomedical engineering. *ACS Nano*, 7 (4), 2891-2897, 2013.

[24] Liong M., Lu J., Kovochich M., Xia T., Ruehm S. G., Nel A. E., Tamanoi F., and Zink J. I. Multifunctional inorganic nanoparticles for imaging, targeting, and drug delivery. *ACS Nano*, 2 (5), 889-896, 2008.

[25] Whitman L. J., Makinen A., Friedersdorf L. E., Holdridge G. M., Thomas T. A., and Howard J. *The national nanotechnology initiative*, National Science and Technology Council, USA, 2017.

[26] Roco M. C., Mirkin C. A., and Hersam M. C. Nanotechnology research directions for societal needs in 2020: summary of international study. *Journal of Nanoparticle Research*, 13 (3), 897-919, 2011.

[27] Rizzo L. Y., Theek B., Storm G., Kiessling F., and Lammers T. Recent progress in nanomedicine: therapeutic, diagnostic and theranostic applications. *Current Opinion in Biotechnology*, 24 (6), 1159-1166, 2013.

[28] Roco M. C. Nanotechnology: convergence with modern biology and medicine. *Current Opinion in Biotechnology*, 14 (3), 337-346, 2003.

[29] Weiss J., Takhistov P., and McClements D. J. Functional materials in food nanotechnology. *Journal of Food Science*, 71 (9), R107-R116, 2006.

[30] Yang H., Wang Y., Lai S., An H., Li Y., and Chen F. Application of atomic force microscopy as a nanotechnology tool in food science. *Journal of Food Science*, 72 (4), R65-R75, 2007.

[31] Seung W., Gupta M. K., Lee K. Y., Shin K.-S., Lee J.-H., Kim T. Y., Kim S., Lin J., Kim J. H., and Kim S.-W. Nanopatterned textile-based wearable triboelectric nanogenerator. *ACS Nano*, 9 (4), 3501-3509, 2015.

[32] Shyamkumar P., Rai P., Oh S., Ramasamy M., Harbaugh R., and Varadan V. Wearable wireless cardiovascular monitoring using textile-based nanosensor and nanomaterial systems. *Electronics*, 3 (3), 504-520, 2014.

[33] Serrano E., Rus G., and García-Martínez J. Nanotechnology for sustainable energy. *Renewable and Sustainable Energy Reviews*, 13 (9), 2373-2384, 2009.

[34] Dai L., Chang D. W., Baek J.-B., and Lu W. Carbon nanomaterials for advanced energy conversion and storage. *Small*, 8 (8), 1130-1166, 2012.

[35] Contreras J. E., Rodriguez E. A., and Taha-Tijerina J. Nanotechnology applications for electrical transformers—A review. *Electric Power Systems Research*, 143, 573-584, 2017.

[36] Cui Y., Zhong Z., Wang D., Wang W. U., and Lieber C. M. High performance silicon nanowire field effect transistors. *Nano Letters*, 3 (2), 149-152, 2003.

[37] Hu J., Odom T. W., and Lieber C. M. Chemistry and physics in one dimension: synthesis and properties of nanowires and nanotubes. *Accounts of Chemical Research*, 32 (5), 435-445, 1999.

[38] Tejada J., Chudnovsky E. M., Barco E. d., Hernandez J. M., and Spiller T. P. Magnetic qubits as hardware for quantum computers. *Nanotechnology*, 12 (2), 181-186, 2001.

[39] Heath J. R., Kuekes P. J., Snider G. S., and Williams R. S. A defect-tolerant computer architecture: opportunities for nanotechnology. *Science*, 280 (5370), 1716-1721, 1998.

[40] Gopalakrishnan K., Birgisson B., Taylor P., and Attoh-Okine N. O. *Nanotechnology in civil infrastructure*, Springer, New York, 2011.

[41] Bang S. S., Lippert J. J., Yerra U., Mulukutla S., and Ramakrishnan V. Microbial calcite, a bio-based smart nanomaterial in concrete remediation. *International Journal of Smart and Nano Materials*, 1 (1), 28-39, 2010.

[42] Park S., Vosguerichian M., and Bao Z. A review of fabrication and applications of carbon nanotube film-based flexible electronics. *Nanoscale*, 5, 1727-1752, 2013.

[43] Sun D.-m., Timmermans M. Y., Tian Y., Nasibulin A. G., Kauppinen E. I., Kishimoto S., Mizutani T., and Ohno Y. Flexible high-performance carbon nanotube integrated circuits. *Nature Nanotechnology*, 6, 156-161, 2011.

[44] Sun D.-M., Liu C., Ren W.-C., and Cheng H.-M. A review of carbon nanotube- and graphene-based flexible thin-film transistors. *Small*, 9 (8), 1188-1205, 2013.

[45] Eda G., Fanchini G., and Chhowalla M. Large-area ultrathin films of reduced graphene oxide as a transparent and flexible electronic material. *Nature Nanotechnology*, 3, 270-274, 2008.

[46] Choi J.-H., Fafarman A. T., Oh S. J., Ko D.-K., Kim D. K., Diroll B. T., Muramoto S., Gillen J. G., Murray C. B., and Kagan C. R. Bandlike transport in strongly coupled and doped quantum dot solids: a route to high-performance thin-film electronics. *Nano Letters*, 12 (5), 2631-2638, 2012.

[47] Radisavljevic B., Radenovic A., Brivio J., Giacometti V., and Kis A. Single-layer MoS2 transistors. *Nature Nanotechnology*, 6, 147-150, 2011.

[48] Geiselmann M., Marty R., García de Abajo F. J., and Quidant R. Fast optical modulation of the fluorescence from a single nitrogen–vacancy centre. *Nature Physics*, 9, 785-789, 2013.

[49] Lee J., Kwon H., Seo J., Shin S., Koo J. H., Pang C., Son S., Kim J. H., Jang Y. H., Kim D. E., and Lee T. Conductive fiber-based ultrasensitive textile pressure sensor for wearable electronics. *Advanced Materials*, 27 (15), 2433-2439, 2015.

[50] Yuen C. W. M., Ku S. K. A., Li Y., Cheng Y. F., Kan C. W., and Choi P. S. R. Improvement of wrinkle-resistant treatment by nanotechnology. *The Journal of The Textile Institute*, 100 (2), 173-180, 2009.

[51] Zhao J., Deng B., Lv M., Li J., Zhang Y., Jiang H., Peng C., Li J., Shi J., Huang Q., and Fan C. Graphene oxide-based antibacterial cotton fabrics. *Advanced Healthcare Materials*, 2 (9), 1259-1266, 2013.

[52] Stoppa M. and Chiolerio A. Wearable electronics and smart textiles: a critical review. *Sensors*, 14 (7), 11957–11992, 2014.

[53] Coyle S., Wu Y., Lau K.-T., De Rossi D., Wallace G., and Diamond D. Smart nanotextiles: a review of materials and applications. *MRS Bulletin*, 32 (5), 434-442, 2007.

[54] Perret G., Ginet P., Tarhan M. C., Baccouche A., Lacornerie T., Kumemura M., Jalabert L., Cleri F., Lartigau E. F., Kim B. J., Karsten S. L., Fujita H., Rondelez Y., Fujii T., and Collard D. Nano systems and devices for applications in biology and nanotechnology. *Solid-State Electronics*, 115, 66-73, 2016.

[55] Hahm J.-I. Biomedical detection via macro- and nano-sensors fabricated with metallic and semiconducting oxides. *Journal of biomedical nanotechnology*, 9 (1), 1-25, 2013.

[56] Libutti S. K., Paciotti G. F., Byrnes A. A., Alexander H. R., Jr., Gannon W. E., Walker M., Seidel G. D., Yuldasheva N., and Tamarkin L. Phase I and pharmacokinetic studies of CYT-6091, a novel PEGylated colloidal gold-rhTNF nanomedicine. *Clinical cancer research : an official journal of the American Association for Cancer Research*, 16 (24), 6139-6149, 2010.

[57] Wang L., Hess A., Chang T. Z., Wang Y.-C., Champion J. A., Compans R. W., and Wang B.-Z. Nanoclusters self-assembled from conformation-stabilized influenza M2e as broadly cross-protective influenza vaccines. *Nanomedicine*, 10 (2), 473-482, 2014.

[58] Ranganathan R., Madanmohan S., Kesavan A., Baskar G., Krishnamoorthy Y. R., Santosham R., Ponraju D., Rayala S. K., and Venkatraman G. Nanomedicine: towards development of patient-friendly drug-delivery systems for oncological applications. *International Journal of Nanomedicine*, 7, 1043-1060, 2012.

[59] Backer M. V., Gaynutdinov T. I., Patel V., Bandyopadhyaya A. K., Thirumamagal B. T. S., Tjarks W., Barth R. F., Claffey K., and Backer J. M. Vascular endothelial growth factor selectively targets boronated dendrimers to tumor vasculature. *Molecular Cancer Therapeutics*, 4 (9), 1423-1429, 2005.

[60] Duan J., Zhang Y., Han S., Chen Y., Li B., Liao M., Chen W., Deng X., Zhao J., and Huang B. Synthesis and in vitro/in vivo anti-cancer evaluation of curcumin-loaded

chitosan/poly(butyl cyanoacrylate) nanoparticles. *International Journal of Pharmaceutics*, 400 (1), 211-220, 2010.

[61] Kurzrock R. and Li L. Liposome-encapsulated curcumin: in vitro and in vivo effects on proliferation, apoptosis, signaling, and angiogenesis. *Journal of Clinical Oncology*, 23 (16), 4091-4091, 2005.

[62] Brigger I., Morizet J., Aubert G., Chacun H., Terrier-Lacombe M.-J., Couvreur P., and Vassal G. Poly(ethylene glycol)-coated hexadecylcyanoacrylate nanospheres display a combined effect for brain tumor targeting. *Journal of Pharmacology and Experimental Therapeutics*, 303 (3), 928-936, 2002.

[63] Tang J., Huo Z., Brittman S., Gao H., and Yang P. Solution-processed core–shell nanowires for efficient photovoltaic cells. *Nature Nanotechnology*, 6, 568-572, 2011.

[64] Zhang H., Yu X., and Braun P. V. Three-dimensional bicontinuous ultrafast-charge and -discharge bulk battery electrodes. *Nature Nanotechnology*, 6, 277-281, 2011.

[65] Nazari A. and Riahi S. ZrO2 nanoparticles' effects on split tensile strength of self compacting concrete. *Materials Research*, 13 (4), 485–495 2010.

[66] Sato T. and Diallo F. Seeding effect of Nano-CaCO3 on the hydration of tricalcium silicate. *Transportation Research Record*, 2141 (1), 61-67, 2010.

[67] Nazari A. and Riahi S. Optimization mechanical properties of Cr2O3 nanoparticle binary blended cementitious composite. *Journal of Composite Materials*, 45 (8), 943-948, 2011.

[68] Daniyal M., Azam A., and Akhtar S. Application of nanomaterials in civil engineering. *Nanomaterials and their applications*, Khan Z. H., Ed. Springer, Singapore, 169-189, 2018.

[69] Williams G., Trask R., and Bond I. A self-healing carbon fibre reinforced polymer for aerospace applications. *Composites Part A: Applied Science and Manufacturing*, 38 (6), 1525-1532, 2007.

[70] Li Z., Chen Y., Li X., Kamins T. I., Nauka K., and Williams R. S. Sequence-specific label-free DNA sensors based on silicon nanowires. *Nano Letters*, 4 (2), 245-247, 2004.

[71] Holzinger M., Le Goff A., and Cosnier S. Nanomaterials for biosensing applications: a review. *Frontiers in Chemistry*, 2 (63), 1-10, 2014.

[72] Xie J., Jiang X., Zhong Y., Lu Y., Wang S., Wei X., Su Y., and He Y. Stem-loop DNA-assisted silicon nanowires-based biochemical sensors with ultra-high sensitivity, specificity, and multiplexing capability. *Nanoscale*, 6 (15), 9215-9222, 2014.

[73] Zhang D., Liu Z., Li C., Tang T., Liu X., Han S., Lei B., and Zhou C. Detection of NO2 down to ppb levels using individual and multiple In2O3 nanowire devices. *Nano Letters*, 4 (10), 1919-1924, 2004.

[74] Lyson-Sypien B., Czapla A., Lubecka M., Kusior E., Zakrzewska K., Radecka M., Kusior A., Balogh A. G., Lauterbach S., and Kleebe H. J. Gas sensing properties of TiO2–SnO2 nanomaterials. *Sensors and Actuators B: Chemical*, 187, 445-454, 2013.

[75] Llobet E. Gas sensors using carbon nanomaterials: A review. *Sensors and Actuators B: Chemical*, 179, 32-45, 2013.

[76] Lonergan M. C., Severin E. J., Doleman B. J., Beaber S. A., Grubbs R. H., and Lewis N. S. Array-based vapor sensing using chemically sensitive, carbon black−polymer resistors. *Chemistry of Materials*, 8 (9), 2298-2312, 1996.

[77] Zhang B., Fu R., Zhang M., Dong X., Wang L., and Pittman C. U. Gas sensitive vapor grown carbon nanofiber/polystyrene sensors. *Materials Research Bulletin*, 41 (3), 553-562, 2006.

[78] Kole A. and Radhakrishnan K. Quantum mechanical investigation into the electronic transport properties of a memantine-functionalized gold nanopore biosensor for natural and mutated DNA nucleobase detection. *RSC Advances*, 7 (14), 8474-8483, 2017.

[79] Wang J. Nanomaterial-based electrochemical biosensors. *Analyst*, 130 (4), 421-426, 2005.

[80] Eckert M. A., Vu P. Q., Zhang K., Kang D., Ali M. M., Xu C., and Zhao W. Novel molecular and nanosensors for in vivo sensing. *Theranostics*, 3 (8), 583-594, 2013.

[81] Thompson A. B., Calhoun A. K., Smagghe B. J., Stevens M. D., Wotkowicz M. T., Hatziioannou V. M., and Bamdad C. A gold nanoparticle platform for protein–protein interactions and drug discovery. *ACS Applied Materials & Interfaces*, 3 (8), 2979-2987, 2011.

[82] Howes P. D., Rana S., and Stevens M. M. Plasmonic nanomaterials for biodiagnostics. *Chemical Society Reviews*, 43 (11), 3835-3853, 2014.

[83] Lu Z., Chen X., and Hu W. A fluorescence aptasensor based on semiconductor quantum dots and MoS2 nanosheets for ochratoxin A detection. *Sensors and Actuators B: Chemical*, 246, 61-67, 2017.

[84] Gullapalli H., Vemuru V. S. M., Kumar A., Botello-Mendez A., Vajtai R., Terrones M., Nagarajaiah S., and Ajayan P. M. Flexible piezoelectric ZnO–paper nanocomposite strain sensor. *Small*, 6 (15), 1641-1646, 2010.

[85] Gong S., Schwalb W., Wang Y., Chen Y., Tang Y., Si J., Shirinzadeh B., and Cheng W. A wearable and highly sensitive pressure sensor with ultrathin gold nanowires. *Nature Communications*, 5 (3132), 1-8, 2014.

[86] Vetrone F., Naccache R., Zamarrón A., Juarranz de la Fuente A., Sanz-Rodríguez F., Martinez Maestro L., Martín Rodriguez E., Jaque D., García Solé J., and Capobianco J. A. Temperature sensing using fluorescent nanothermometers. *ACS Nano*, 4 (6), 3254-3258, 2010.

[87] Lin L., Xie Y., Wang S., Wu W., Niu S., Wen X., and Wang Z. L. Triboelectric active sensor array for self-powered static and dynamic pressure detection and tactile imaging. *ACS Nano*, 7 (9), 8266-8274, 2013.

[88] Stampfer C., Jungen A., Linderman R., Obergfell D., Roth S., and Hierold C. Nano-electromechanical displacement sensing based on single-walled carbon nanotubes. *Nano Letters*, 6 (7), 1449-1453, 2006.

[89] Tombler T. W., Zhou C., Alexseyev L., Kong J., Dai H., Liu L., Jayanthi C. S., Tang M., and Wu S.-Y. Reversible electromechanical characteristics of carbon nanotubes underlocal-probe manipulation. *Nature*, 405, 769–772, 2000.

[90] Cronin S. B., Swan A. K., Ünlü M. S., Goldberg B. B., Dresselhaus M. S., and Tinkham M. Resonant Raman spectroscopy of individual metallic and semiconducting single-wall carbon nanotubes under uniaxial strain. *Physical Review B*, 72 (3), 1-8, 2005.

[91] Dharap P., Li Z., Nagarajaiah S., and Barrera E. V. Nanotube film based on single-wall carbon nanotubes for strain sensing. *Nanotechnology*, 15 (3), 379-382, 2004.

[92] Loyola B. R., Zhao Y., Loh K. J., and Saponara V. L. The electrical response of carbon nanotube-based thin film sensors subjected to mechanical and environmental effects. *Smart Materials and Structures*, 22 (2), 025010, 2013.

[93] Mortensen L. P., Ryu D. H., Zhao Y. J., and Loh K. J. Rapid assembly of multifunctional thin film sensors for wind turbine blade monitoring. *Key Engineering Materials*, 569, 515-522, 2013.

[94] Kang J. H., Park C., Scholl J. A., Brazin A. H., Holloway N. M., High J. W., Lowther S. E., and Harrison J. S. Piezoresistive characteristics of single wall carbon nanotube/polyimide nanocomposites. *Journal of Polymer Science Part B: Polymer Physics*, 47 (10), 994-1003, 2009.

[95] Frogley M. D., Zhao Q., and Wagner H. D. Polarized resonance Raman spectroscopy of single-wall carbon nanotubes within a polymer under strain. *Physical Review B*, 65 (11), 113413, 2002.

[96] Loh K. J., Kim J., Lynch J. P., Kam N. W. S., and Kotov N. A. Multifunctional layer-by-layer carbon nanotube–polyelectrolyte thin films for strain and corrosion sensing. *Smart Materials and Structures*, 16 (2), 429-438, 2007.

[97] Park M., Kim H., and Youngblood J. P. Strain-dependent electrical resistance of multi-walled carbon nanotube/polymer composite films. *Nanotechnology*, 19 (5), 055705, 2008.

[98] Pham G. T., Park Y.-B., Liang Z., Zhang C., and Wang B. Processing and modeling of conductive thermoplastic/carbon nanotube films for strain sensing. *Composites Part B: Engineering*, 39 (1), 209-216, 2008.

[99] Christ J. F., Aliheidari N., Ameli A., and Pötschke P. 3D printed highly elastic strain sensors of multiwalled carbon nanotube/thermoplastic polyurethane nanocomposites. *Materials & Design*, 131, 394-401, 2017.

[100] Farahani R. D., Dalir H., Borgne V. L., Gautier L. A., Khakani M. A. E., Lévesque M., and Therriault D. Direct-write fabrication of freestanding nanocomposite strain sensors. *Nanotechnology*, 23 (8), 085502, 2012.

[101] Park J.-M., Kim D.-S., Lee J.-R., and Kim T.-W. Nondestructive damage sensitivity and reinforcing effect of carbon nanotube/epoxy composites using electro-micromechanical technique. *Materials Science and Engineering: C*, 23 (6), 971-975, 2003.

[102] Alexopoulos N. D., Jaillet C., Zakri C., Poulin P., and Kourkoulis S. K. Improved strain sensing performance of glass fiber polymer composites with embedded pre-stretched polyvinyl alcohol–carbon nanotube fibers. *Carbon*, 59, 65-75, 2013.

[103] Sam-Daliri O., Faller L.-M., Farahani M., Roshanghias A., Oberlercher H., Mitterer T., Araee A., and Zangl H. MWCNT–epoxy nanocomposite sensors for structural health monitoring. *Electronics*, 7 (8), 1-14, 2018.

[104] Martin C. A., Sandler J. K. W., Shaffer M. S. P., Schwarz M. K., Bauhofer W., Schulte K., and Windle A. H. Formation of percolating networks in multi-wall carbon-nanotube–epoxy composites. *Composites Science and Technology*, 64 (15), 2309-2316, 2004.

[105] Qiu W., Li Q., Lei Z.-K., Qin Q.-H., Deng W.-L., and Kang Y.-L. The use of a carbon nanotube sensor for measuring strain by micro-Raman spectroscopy. *Carbon*, 53, 161-168, 2013.

[106] Lipomi D. J., Vosgueritchian M., Tee B. C. K., Hellstrom S. L., Lee J. A., Fox C. H., and Bao Z. Skin-like pressure and strain sensors based on transparent elastic films of carbon nanotubes. *Nature Nanotechnology*, 6, 788-792, 2011.

[107] Dharap P., Li Z., Nagarajaiah S., and Barrera E. V. Flexural strain sensing using carbon nanotube film. *Sensor Review*, 24 (3), 271-273, 2004.

[108] Thostenson E. T. and Chou T.-W. Real-time in situ sensing of damage evolution in advanced fiber composites using carbon nanotube networks. *Nanotechnology*, 19 (21), 1-6, 2008.

[109] Loh K. J. and Gonzalez J. Cementitious composites engineered with embedded carbon nanotube thin films for enhanced sensing performance. *Journal of Physics: Conference Series*, 628 (1), 1-8, 2015.

[110] Gupta S., Gonzalez J. G., and Loh K. J. Self-sensing concrete enabled by nano-engineered cement–aggregate interfaces. *Structural Health Monitoring*, 16 (3), 1-15, 2016.

[111] Loh K. J., Lynch J. P., Shim B., and Kotov N. Tailoring piezoresistive sensitivity of multilayer carbon nanotube composite strain sensors. *Journal of Intelligent Material Systems and Structures*, 19 (7), 747-764, 2008.

[112] Kanoun O., Müller C., Benchirouf A., Sanli A., Dinh T., Al-Hamry A., Bu L., Gerlach C., and Bouhamed A. Flexible carbon nanotube films for high performance strain sensors. *Sensors*, 14 (6), 10042-10072, 2014.

[113] Alamusi, Hu N., Fukunaga H., Atobe S., Liu Y., and Li J. Piezoresistive strain sensors made from carbon nanotubes based polymer nanocomposites. *Sensors*, 11 (11), 10691-10723, 2011.

[114] Hu N., Karube Y., Arai M., Watanabe T., Yan C., Li Y., Liu Y., and Fukunaga H. Investigation on sensitivity of a polymer/carbon nanotube composite strain sensor. *Carbon*, 48 (3), 680-687, 2010.

[115] Zeng X., Xu X., Shenai P. M., Kovalev E., Baudot C., Mathews N., and Zhao Y. Characteristics of the electrical percolation in carbon nanotubes/polymer nanocomposites. *The Journal of Physical Chemistry C*, 115 (44), 21685-21690, 2011.

[116] Kumar S., Murthy J. Y., and Alam M. A. Percolating conduction in finite nanotube networks. *Physical Review Letters*, 95 (6), 1-4, 2005.

[117] Behnam A. and Ural A. Computational study of geometry-dependent resistivity scaling in single-walled carbon nanotube films. *Physical Review B*, 75 (12), 125432, 2007.

[118] Bao W. S., Meguid S. A., Zhu Z. H., and Meguid M. J. Modeling electrical conductivities of nanocomposites with aligned carbon nanotubes. *Nanotechnology*, 22 (48), 1-8, 2011.

[119] Li C., Thostenson E. T., and Chou T.-W. Effect of nanotube waviness on the electrical conductivity of carbon nanotube-based composites. *Composites Science and Technology*, 68 (6), 1445-1452, 2008.

[120] Du F., Fischer J. E., and Winey K. I. Effect of nanotube alignment on percolation conductivity in carbon nanotube/polymer composites. *Physical Review B*, 72 (12), 121404, 2005.

[121] Hu N., Karube Y., Yan C., Masuda Z., and Fukunaga H. Tunneling effect in a polymer/carbon nanotube nanocomposite strain sensor. *Acta Materialia*, 56 (13), 2929-2936, 2008.

[122] Rahman R. and Servati P. Effects of inter-tube distance and alignment on tunnelling resistance and strain sensitivity of nanotube/polymer composite films. *Nanotechnology*, 23 (5), 1-9, 2012.

[123] Wang Z. and Ye X. A numerical investigation on piezoresistive behaviour of carbon nanotube/polymer composites: mechanism and optimizing principle. *Nanotechnology*, 24 (26), 1-10, 2013.

[124] Amini A. and Bahreyni B. Behavioral model for electrical response and strain sensitivity of nanotube-based nanocomposite materials. *Journal of Vacuum Science & Technology B*, 30 (2), 022001, 2012.

[125] Yin G., Hu N., Karube Y., Liu Y., Li Y., and Fukunaga H. A carbon nanotube/polymer strain sensor with linear and anti-symmetric piezoresistivity. *Journal of Composite Materials*, 45 (12), 1315-1323, 2011.

[126] Jang H.-S., Lee Y.-H., Na H.-J., and Nahm S. H. Variation in electrical resistance versus strain of an individual multiwalled carbon nanotube. *Journal of Applied Physics*, 104 (11), 114304, 2008.

[127] Broadbent S. R. and Hammersley J. M. Percolation processes. *Mathematical Proceedings of the Cambridge Philosophical Society*, 53 (3), 629-641, 1957.

[128] Hammersley J. M. Percolation Processes: Lower Bounds for the Critical Probability. *The Annals of Mathematical Statistics*, 28 (3), 790-795, 1957.

[129] Kirkpatrick S. Percolation and Conduction. *Reviews of Modern Physics*, 45 (4), 574-588, 1973.

[130] Lee B. M., Loh K. J., Burton A., and Loyola B. R. Modeling the electromechanical and strain response of carbon nanotube-based nanocomposites. *SPIE*, 906117, 2014.

[131] Odegard G. M. Multiscale modeling of nanocomposite materials. *Virtual Testing and Predictive Modeling*, Farahmand B., Ed. Springer, 221-245, 2009.

[132] Harper L. T., Qian C., Turner T. A., Li S., and Warrior N. A. Representative volume elements for discontinuous carbon fibre composites – Part 1: Boundary conditions. *Composites Science and Technology*, 72 (2), 225-234, 2012.

[133] Kanit T., Forest S., Galliet I., Mounoury V., and Jeulin D. Determination of the size of the representative volume element for random composites: statistical and numerical approach. *International Journal of Solids and Structures*, 40 (13–14), 3647-3679, 2003.

[134] Hill R. Elastic properties of reinforced solids: Some theoretical principles. *Journal of the Mechanics and Physics of Solids*, 11 (5), 357-372, 1963.

[135] Berhan L. and Sastry A. M. Modeling percolation in high-aspect-ratio fiber systems. I. Soft-core versus hard-core models. *Physical Review E*, 75 (4), 041120, 2007.

[136] McEuen P. L. and Park J.-Y. Electron transport in single-walled carbon nanotubes. *MRS Bulletin*, 29 (4), 272-275, 2004.

[137] Bandaru P. R. Electrical properties and applications of carbon nanotube structures. *Journal of Nanoscience and Nanotechnology*, 7 (3), 1-29, 2007.

[138] Fuhrer M. S., Nygård J., Shih L., Forero M., Yoon Y.-G., Mazzoni M. S. C., Choi H. J., Ihm J., Louie S. G., Zettl A., and McEuen P. L. Crossed nanotube junctions. *Science*, 288 (5465), 494-497, 2000.

[139] Nirmalraj P. N., Lyons P. E., De S., Coleman J. N., and Boland J. J. Electrical connectivity in single-walled carbon nanotube networks. *Nano Letters*, 9 (11), 3890-3895, 2009.

[140] Wang L., Loh K. J., Brely L., Bosia F., and Pugno N. M. An experimental and numerical study on the mechanical properties of carbon nanotube-latex thin films. *Journal of the European Ceramic Society*, 36 (9), 2255-2262, 2016.

[141] Cao J., Wang Q., and Dai H. Electromechanical properties of metallic, quasimetallic, and semiconducting carbon nanotubes under stretching. *Physical Review Letters*, 90 (15), 157601, 2003.

[142] Bauhofer W. and Kovacs J. Z. A review and analysis of electrical percolation in carbon nanotube polymer composites. *Composites Science and Technology*, 69 (10), 1486-1498, 2009.

[143] Lee D., Hong H. P., Lee C. J., Park C. W., and Min N. K. Microfabrication and characterization of spray-coated single-wall carbon nanotube film strain gauges. *Nanotechnology*, 22 (45), 455301, 2011.

[144] Li X., Levy C., and Elaadil L. Multiwalled carbon nanotube film for strain sensing. *Nanotechnology*, 19 (4), 045501, 2008.

[145] Jang J., Cha S., Choi Y., Amaratunga G. A., Kang D., Hasko D., Jung J., and Kim J. Nanoelectromechanical switches with vertically aligned carbon nanotubes. *Applied Physics Letters*, 87 (16), 163114, 2005.

[146] Gommes C., Blacher S., Masenelli-Varlot K., Bossuot C., McRae E., Fonseca A., Nagy J. B., and Pirard J. P. Image analysis characterization of multi-walled carbon nanotubes. *Carbon*, 41 (13), 2561-2572, 2003.

[147] Tenent R. C., Barnes T. M., Bergeson J. D., Ferguson A. J., To B., Gedvilas L. M., Heben M. J., and Blackburn J. L. Ultrasmooth, large-area, high-uniformity, conductive transparent single-walled-carbon-nanotube films for photovoltaics produced by ultrasonic spraying. *Advanced Materials*, 21 (31), 3210-3216, 2009.

[148] Timmermans M. Y., Estrada D., Nasibulin A. G., Wood J. D., Behnam A., Sun D.-m., Ohno Y., Lyding J. W., Hassanien A., Pop E., and Kauppinen E. I. Effect of carbon nanotube network morphology on thin film transistor performance. *Nano Research*, 5 (5), 307-319, 2012.

[149] Lee B. M. and Loh K. J. A 2D percolation-based model for characterizing the piezoresistivity of carbon nanotube-based films. *Journal of Materials Science*, 50 (7), 2973-2983, 2015.

[150] Li C. and Chou T.-W. Continuum percolation of nanocomposites with fillers of arbitrary shapes. *Applied Physics Letters*, 90 (17), 174108, 2007.

[151] Yi Y. B., Berhan L., and Sastry A. M. Statistical geometry of random fibrous networks, revisited: Waviness, dimensionality, and percolation. *Journal of Applied Physics*, 96 (3), 1318-1327, 2004.

[152] Dalmas F., Dendievel R., Chazeau L., Cavaillé J.-Y., and Gauthier C. Carbon nanotube-filled polymer composites. Numerical simulation of electrical conductivity in three-dimensional entangled fibrous networks. *Acta Materialia*, 54 (11), 2923-2931, 2006.

[153] Berhan L. and Sastry A. M. Modeling percolation in high-aspect-ratio fiber systems. II. The effect of waviness on the percolation onset. *Physical Review E*, 75 (4), 041121, 2007.

[154] Zhang Z., Wei H., Liu Y., and Leng J. Self-sensing properties of smart composite based on embedded buckypaper layer. *Structural Health Monitoring*, 14 (2), 127-136, 2015.

[155] Vaisman L., Wagner H. D., and Marom G. The role of surfactants in dispersion of carbon nanotubes. *Advances in Colloid and Interface Science*, 128–130, 37-46, 2006.

[156] Shvartzman-Cohen R., Florent M., Goldfarb D., Szleifer I., and Yerushalmi-Rozen R. Aggregation and self-assembly of amphiphilic block copolymers in aqueous dispersions of carbon nanotubes. *Langmuir*, 24 (9), 4625-4632, 2008.

[157] Zhao Y., Viechtbauer C., Loh K. J., and Schagerl M. Enhancing the strain sensitivity of carbon nanotube-polymer thin films for damage detection and structural monitoring. *11th International Workshop on Advanced Smart Materials and Smart Structures Technology* 1-8, 2015.

[158] Pop E., Mann D., Wang Q., Goodson K., and Dai H. Thermal conductance of an individual single-wall carbon nanotube above room temperature. *Nano Letters*, 6 (1), 96-100, 2006.

[159] Chen R. J., Franklin N. R., Kong J., Cao J., Tombler T. W., Zhang Y., and Dai H. Molecular photodesorption from single-walled carbon nanotubes. *Applied Physics Letters*, 79 (14), 2258-2260, 2001.

[160] Yu H., Cao T., Zhou L., Gu E., Yu D., and Jiang D. Layer-by-Layer assembly and humidity sensitive behavior of poly(ethyleneimine)/multiwall carbon nanotube composite films. *Sensors and Actuators B: Chemical*, 119 (2), 512-515, 2006.

[161] Fuhrer M. S., Lim A. K. L., Shih L., Varadarajan U., Zettl A., and McEuen P. L. Transport through crossed nanotubes. *Physica E: Low-dimensional Systems and Nanostructures*, 6 (1–4), 868-871, 2000.

[162] Cullinan M. A. and Culpepper M. L. Carbon nanotubes as piezoresistive microelectromechanical sensors: Theory and experiment. *Physical Review B*, 82 (11), 115428, 2010.

[163] Li W., Buschhorn S. T., Schulte K., and Bauhofer W. The imaging mechanism, imaging depth, and parameters influencing the visibility of carbon nanotubes in a polymer matrix using an SEM. *Carbon*, 49 (6), 1955-1964, 2011.

[164] Zhao M., Ming B., Kim J.-W., Gibbons L. J., Gu X., Nguyen T., Park C., Lillehei P. T., Villarrubia J. S., Vladár A. E., and Liddle J. A. New insights into subsurface imaging of carbon nanotubes in polymer composites via scanning electron microscopy. *Nanotechnology*, 26 (16), 085703, 2015.

[165] Farrar C. R. and Worden K. *An introduction to structural health monitoring*, The Royal Society, London, UK, 2007.

[166] Farrar C. R. and Worden K. *Structural health monitoring: a machine learning perspective*, Wiley, United Kingdom, 1-667, 2012.

[167] Chan T. H. T., Li Z. X., and Ko J. M. Fatigue analysis and life prediction of bridges with structural health monitoring data — Part II: application. *International Journal of Fatigue*, 23 (1), 55-64, 2001.

[168] Gomez J., Zubia J., Aranguren G., Arrue J., Poisel H., and Saez I. Comparing polymer optical fiber, fiber Bragg grating, and traditional strain gauge for aircraft structural health monitoring. *Applied Optics*, 48 (8), 1436-1443, 2009.

[169] Swartz R. A., Lynch J. P., Sweetman B., Rolfes R., and Zerbst S. Structural monitoring of wind turbines using wireless sensor networks. *Smart Structures and Systems*, 6 (3), 183-196, 2010.

[170] McCann D. M. and Forde M. C. Review of NDT methods in the assessment of concrete and masonry structures. *NDT & E International*, 34 (2), 71-84, 2001.

[171] Ewert U., Redmer B., and Müller J. Mechanized weld inspection for detection of planar defects and depth measurements by tomosynthesis and planartomography. *AIP Conference Proceedings*, 509 (1), 2093-2098, 2000.

[172] Kolkoori S., Wrobel N., Zscherpel U., and Ewert U. A new X-ray backscatter imaging technique for non-destructive testing of aerospace materials. *NDT & E International*, 70, 41-52, 2015.

[173] Shafeek H. I., Gadelmawla E. S., Abdel-Shafy A. A., and Elewa I. M. Automatic inspection of gas pipeline welding defects using an expert vision system. *NDT & E International*, 37 (4), 301-307, 2004.

[174] Liao T. W. and Li Y. An automated radiographic NDT system for weld inspection: Part II—Flaw detection. *NDT & E International*, 31 (3), 183-192, 1998.

[175] Shull P. J. *Nondestructive evaluation: theory, techniques, and applications*, Marcel Dekker, New York, 2002.

[176] Liu Y., Chen W.-L., Bond L. J., and Hu H. Development of an ultrasonic pulse-echo (UPE) technique for aircraft icing studies. *AIP Conference Proceedings*, 1581 (1), 1757-1764, 2014.

[177] Kashif Ur Rehman S., Ibrahim Z., Memon S. A., and Jameel M. Nondestructive test methods for concrete bridges: A review. *Construction and Building Materials*, 107, 58-86, 2016.

[178] Schubel P. J., Crossley R. J., Boateng E. K. G., and Hutchinson J. R. Review of structural health and cure monitoring techniques for large wind turbine blades. *Renewable Energy*, 51, 113-123, 2013.

[179] Li S., Shi K., Yang K., and Xu J. Research on the defect types judgment in wind turbine blades using ultrasonic NDT. *IOP Conference Series: Materials Science and Engineering*, 87 (1), 012056, 2015.

[180] Pan E., Rogers J., Datta S. K., and Shah A. H. Mode selection of guided waves for ultrasonic inspection of gas pipelines with thick coating. *Mechanics of Materials*, 31 (3), 165-174, 1999.

[181] Chan T. H. T., Yu L., Tam H. Y., Ni Y. Q., Liu S. Y., Chung W. H., and Cheng L. K. Fiber Bragg grating sensors for structural health monitoring of Tsing Ma bridge: Background and experimental observation. *Engineering Structures*, 28 (5), 648-659, 2006.

[182] Minakuchi S., Okabe Y., and Takeda N. Real-time detection of debonding between honeycomb core and facesheet using a small-diameter FBG sensor embedded in adhesive layer. *Journal of Sandwich Structures & Materials*, 9 (1), 9-33, 2007.

[183] Takeda S., Yamamoto T., Okabe Y., and Takeda N. Debonding monitoring of composite repair patches using embedded small-diameter FBG sensors. *Smart Materials and Structures*, 16 (3), 763-770, 2007.

[184] Mihailov S. J. Fiber Bragg grating sensors for harsh environments. *Sensors*, 12 (2), 1898-1918, 2012.

[185] Bao X. and Chen L. Recent progress in distributed fiber optic sensors. *Sensors*, 12 (7), 8601-8639, 2012.

[186] Di Sante R. Fibre optic sensors for structural health monitoring of aircraft composite structures: recent advances and applications. *Sensors*, 15 (8), 18666-18713, 2015.

[187] Barnoski M. K., Rourke M. D., Jensen S. M., and Melville R. T. Optical time domain reflectometer. *Applied Optics*, 16 (9), 2375-2379, 1977.

[188] Juarez J. C. and Taylor H. F. Polarization discrimination in a phase-sensitive optical time-domain reflectometer intrusion-sensor system. *Optics Letters*, 30 (24), 3284-3286, 2005.

[189] Pozar D. M. *Microwave engineering*, Wiley, NJ, 2012.

[190] Dowding C. H., Su M. B., and O'Connor K. Measurement of rock mass deformation with grouted coaxial antenna cables. *Rock Mechanics and Rock Engineering*, 22 (1), 1-23, 1989.

[191] Noborio K. Measurement of soil water content and electrical conductivity by time domain reflectometry: a review. *Computers and Electronics in Agriculture*, 31 (3), 213-237, 2001.

[192] Liu W., Hunsperger R. G., Chajes M. J., Folliard K. J., and Kunz E. Corrosion Detection of Steel Cables using Time Domain Reflectometry. *Journal of Materials in Civil Engineering*, 14 (3), 217-223, 2002.

[193] Lin M. W., Thaduri J., and Abatan A. O. Development of an electrical time domain reflectometry (ETDR) distributed strain sensor. *Measurement Science and Technology*, 16 (7), 1495–1505, 2005.

[194] Lin M. W., Abatan A. O., and Zhang W.-M. Crack damage detection of concrete structures using distributed electrical time domain reflectometry (ETDR) sensors. *1999 Symposium on Smart Structures and Materials*, 297-304, 1999.

[195] Panth D. Reasons for failure of transmission lines and their prevention strategies. *International Journal of Electrical, Electronics and Data Communication*, 2 (1), 1-4, 2014.

[196] Chen G. D., Sun S. S., Pommerenke D., Drewniak J. L., Greene G. G., McDaniel R. D., Belarbi A., and Mu H. M. Crack detection of a full-scale reinforced concrete girder with a distributed cable sensor. *Smart Materials and Structures*, 14 (3), S88–S97, 2005.

[197] Todoroki A., Ohara K., Mizutani Y., Suzuki Y., and Matsuzaki R. Self-sensing time-domain reflectometry for detection of the bearing failure of a CFRP laminate fastener hole: effect of peeling of the insulator. *Advanced Composite Materials*, 25 (5), 457-469, 2016.

[198] Pandey G., Wolters M., Thostenson E. T., and Heider D. Localized functionally modified glass fibers with carbon nanotube networks for crack sensing in composites using time domain reflectometry. *Carbon*, 50 (10), 3816-3825, 2012.

[199] Sanli A., Müller C., Kanoun O., Elibol C., and Wagner M. F. X. Piezoresistive characterization of multi-walled carbon nanotube-epoxy based flexible strain sensitive films by impedance spectroscopy. *Composites Science and Technology*, 122, 18-26, 2016.

[200] Esen G., Fuhrer M. S., Ishigami M., and Williams E. D. Transmission line impedance of carbon nanotube thin films for chemical sensing. *Applied Physics Letters*, 90 (12), 123510, 2007.

[201] Du F., Fischer J. E., and Winey K. I. Coagulation method for preparing single-walled carbon nanotube/poly(methyl methacrylate) composites and their modulus, electrical conductivity, and thermal stability. *Journal of Polymer Science Part B: Polymer Physics*, 41 (24), 3333-3338, 2003.

[202] Oliva-Avilés A. I., Avilés F., Sosa V., Oliva A. I., and Gamboa F. Dynamics of carbon nanotube alignment by electric fields. *Nanotechnology*, 23 (46), 465710, 2012.

[203] Yang C., Lin Y., and Nan C. W. Modified carbon nanotube composites with high dielectric constant, low dielectric loss and large energy density. *Carbon*, 47 (4), 1096-1101, 2009.

[204] Wang L. and Dang Z.-M. Carbon nanotube composites with high dielectric constant at low percolation threshold. *Applied Physics Letters*, 87 (4), 2005.

[205] Lee H. Y. and Shkel Y. M. Dielectric response of solids for contactless detection of stresses and strains. *Sensors and Actuators A: Physical*, 137 (2), 287-295, 2007.

[206] Guo X., Yu D., Gao Y., Li Q., Wan W., and Gao Z. Dielectric properties of filled carbon nanotubes/epoxy composites with high dielectric constant. *2006 1st IEEE International Conference on Nano/Micro Engineered and Molecular Systems*, 295-298, 2006.